UNIVERSITA DEGLI STUDI DI FERRARA

Dottorato in Scienze dell' Ingegneria

Study, Modeling and Design of Semiconductor Photonic Crystal Based Devices

Ph. D. Thesis

Advisor	**Ph. D. Student**
Prof. Stefano Trillo	Stefania Malaguti

Defended on March 25, 2011

Ciclo XXIII

Contents

Introduction

In the last years great attention has been addressed to the study of light control with the purpose to realize all-optical signal processing. A lot of research works have been focused on nonlinear effects in semiconductor materials and on their exploitation to manipulate optical signals. One of the main key to realize high performances optical devices by using nonlinearities, is essentially that to obtain the best compromise between speed of processes and required power consumption. Ultra-fast nonlinear dynamics with low employment of power can be reached in nano-photonic structures by engineering material and geometrical features. From this point of view, one of the most attractive framework to achieve strong light-matter interactions and consecutively enhance optical nonlinearities are, of course, small volume resonant cavities. In such systems a careful design can lead to maximize the efficiency and minimize the required power to trigger a given nonlinear process.

Within the general overview of optical signal-processing, all-optical switching is one of the most important target for photonics. Switching functionalities can been achieved by exploiting the nonlinear modulation of the refractive index induced by electromagnetic optical intensity. To this purpose, ultra-small and high-quality factor (high-Q) cavities must be realized as switching elements. In fact, by confining the light in a small volume and for a long time, the field intensity inside the cavity is enhanced by a factor of Q/V, where V is the modal volume. At the same time, the frequency shift required for switching is decreased by a factor of Q, and a high switching contrast becomes possible with very small frequency shift. As a result, high-Q, small volume cavities exhibit switching power that generally decreases as V/Q^2. Switching resonators based on semiconductor materials such as GaAs [1] or Silicon [2], [3] have been demonstrated to require very low power consumption. How-

ever, the tread-off between small volume V and high quality factor Q with conventional optical cavities did not lead to fulfill the envisaged achievements and nowadays the research of new solutions is still a fascinating challenge.

Among the different investigated optical nano-structures, photonic crystals (PhC) are, perhaps, one of the most interesting environment that allows for the design of highly-efficient optical switching devices. High-Q, small volume cavities created by defects and coupled to line-defect waveguides allow for implementing photonic functionalities with great flexibility [5]- [10]. Furthermore, air-hole semiconductor membranes are very promising structures where optical switching can be achieved by tuning the cavity through the nonlinear response of the material. In this respect, III-V semiconductors and in particular GaAs have been demonstrated to be viable candidates due to their fast carrier dynamics, weak nonlinear losses, and low power requirements [7]-[11].

The aim of this thesis is to deeply analyze the more important nonlinear effects exhibited by semiconductor materials in order to understand how to exploit their functionalities for the design of all-optical devices. Insight into the nonlinear semiconductor dynamics is obtained by both analytical approach and numerical modeling. To this end, Coupled Mode Theory (CMT) models [24] able to investigate the linear response of different topologies composed by optical resonators and waveguides are developed, and nonlinear CMT models that account for the whole relevant semiconductor nonlinearities such as the Kerr effect and two photon absorption (TPA) are used. Furthermore, a two dimensional finite difference time domain (FDTD) code is set up in order to numerically model the nonlinear behavior in semiconductor devices. In particular, a 2D-FDTD code that incorporates all of the nonlinear effects such as, precisely, Kerr and two photon absorption nonlinearities, as well as free carriers dispersion (FCD) and free carriers absorption (FCA) induced by TPA, is realized. Finally, in order to give an accurate description of the carriers dynamics that takes place in semiconductors, a rate equation that includes both bulk recombinations and diffusion effects is discretized in the FDTD code.

Then, after discussing the tools of analysis, this thesis is primarily concerned with the design of optical devices, in particular, in the framework of the pho-

tonic crystal technology. Indeed, as explained, they are one the most promising environment to enhance nonlinear processes. Different PhC topologies in various nonlinear optical regimes are analyzed and discussed by means of nonlinear CMT and FDTD models with the purpose of building up a set of tools aimed at designing these types of devices. Once such set of tools are fine tuned, they are employed to investigate new PhC switching configurations. In particular, at the end of this thesis, some optimized All-Optical-Gate topologies are designed. These designs are the basis for one of the main target pursued in the framework of the EU. *Copernicus* (Compact OTDM / WDM Optical Receivers based on Photonic Crystal Integrated Circuits) project. The aim is to supply a starting point for future developments of ultra-fast high-performances all-optical signal processing devices.

The thesis is organized as follows:

- In the first chapter a preliminary description of the most relevant nonlinear effects in standard semiconductor materials is outlined. The mathematical models of the nonlinear response including Kerr effect and two photon absorption are developed, and this formalism is then extended to the case of polarized light in a two dimensional domain.

- In the second chapter photonic crystals are described with particular care for two-dimensional periodic structures such as photonic crystal membranes that, due to their feasibility in recent fabrication processes, are becoming promising environments for phtonics.

- In the third chapter the Kerr effect is deeply analyzed. Bistable response induced by Kerr nonlinearity in optical resonators is investigated by means of CMT models and nonlinear 2D-FDTD codes. In the last sections of this chapter some possible configurations of PhC devices that can be realized by exploiting nonlinear Kerr bistability are presented. In particular, a simple all-optical serial-to-parallel converter is designed.

- In the fourth chapter the two photon absorption in semiconductor materials is investigated. Free carriers dispersion is analyzed by means of CMT equations, and bistable dynamics induced by FCD is demonstrated in optical resonators. Moreover, it is shown that the FCD associated with TPA can lead to the onset of spontaneous oscillations (self-pulsing) when the nonlinear losses are not too high. The 2D-FDTD code is completed with all of the

nonlinear governing equations. The correctness of the FDTD code is verified by comparison with experimental results. Finally, some optimized PhC switching designs are presented and discussed.

Chapter 1

Nonlinear effects in semiconductor materials

1.1 Introduction

The purpose of this chapter is to acquire the basic knowledge addressed to the set up of an useful tool for the design of high-performances optical devices. To this end, the most relevant nonlinear effects in semiconductor materials are studied. In particular, effects such as Kerr and two photon absorption are both physically analyzed and mathematically described. The analysis of nonlinearities in semiconductor materials is then extended to the case of polarized light with the aim of modeling the nonlinear light behavior in periodic structures by means of numerical methods.

1.2 Physic of Kerr and two photon absorption effects

Nonlinear optics is a wide field of study that involves a large number of phenomena. A first distinction concerning the atomic quantum-mechanical state can be made between parametric and nonparametric processes [14].
Parametric processes are those in which the initial and final energy states of the system are the same. In a parametric process the population of the
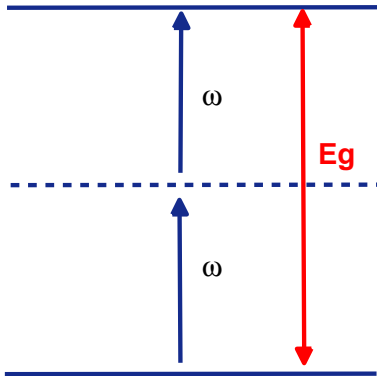
Figure 1.1: Two photon absorption scheme.

electrons can be removed from the ground state only for brief intervals of time and resides in a virtual level for a time interval of the order of $\hbar/\delta E_v$, where δE_v is the energy difference between the two energy levels. Moreover, in parametric processes the photon energy is always conserved so that they admit a purely real susceptibility.

In the nonparametric processes, on the contrary, the populations can be transferred from a real state to an another real state. The photon energy is not conserved because can be transferred to or from the material medium then, unlike the parametric processes, nonparametric processes must be described by a complex susceptibility.

Kerr effect is a third-order process which results in a change of the refractive index that linearly depend on the optical intensity. The Kerr effect is a parametric process and then does not require real electronic transitions. Also, it is considered as a instantaneous effect, because its speed is of the order of electronics vibrations.

In two photon absorption (TPA) processes, two photons are simultaneously absorbed by exciting an electron to transit from its ground state (valence band) to an excited state (conduction band). This can only happen if the total energy of the two photons exceeds the energy difference between the valence and conduction band, i.e. if $2\hbar\omega > E_g$, where E_g is the energy gap (see Fig. 1.1). The result of two photon absorption is the creation of

6

free carriers which in turn change the electrical and optical properties of the medium giving rise to additional nonlinear effects. In fact, a free carrier can absorb a photon and move to a higher energy state inside the band. This is the free carriers absorption (FCA) phenomenon, also known as the plasma effect induced by TPA. Free carriers absorption is then responsible for both losses and change of the refractive index (also known as free carrier dispersion (FCD)) in the medium. The modulation of the refractive index induced by free carrier generations exhibits a characteristic speed limited by the relaxation time of the carriers.

1.3 Mathematical formalism for Kerr and two photon absorption

Formally the Kerr effect can be considered as a perturbation of the refractive index that occurs in presence of an electromagnetic field. This perturbation linearly depends on the light intensity, i.e.:

$$n = n_0 + n_{2I}I \tag{1.1}$$

where n_0 is the linear refractive index of the material, n_{2I} is the Kerr coefficient, and I is the optical intensity. Since the optical intensity can be expressed in terms of the electric field as follows

$$I = \frac{1}{2}\epsilon_0 c_0 n_0 |E|^2 \tag{1.2}$$

the Eq. (1.1) can be written as

$$n = n_0 + n_2|E|^2 \tag{1.3}$$

with $\epsilon_0 = 8.854 \times 10^{-12} F/m$ the free space permittivity and $c_0 = 2.997 \times 10^8 m/s$ the speed of light in the vacuum. The Eq. (1.2) leads to the following relationships between the nonlinear coefficients

$$
\begin{aligned}
n_{2I} &= \frac{2}{\epsilon_0 c_0 n_0} n_2 \\
n_2 &= \frac{\epsilon_0 c_0 n_0}{2} n_{2I}
\end{aligned}
\tag{1.4}
$$

Equivalently, the absorption effect linearly depends on the intensity under the following relationship

$$\alpha = \alpha_0 + \alpha_{2I} I \tag{1.5}$$

that, by Eq. (1.2), can be written as

$$\alpha = \alpha_0 + \alpha_2 |E|^2 \tag{1.6}$$

where α_0 is the linear lossy coefficient and α_{2I} the two photon absorption coefficient.

The origin of such effects can be related to a linear perturbation of the material polarization due to the presence of light intensity. In particular, the polarization can be expanded in a power series as

$$\mathcal{P}(t) = \mathcal{P}^{(1)}(t) + \mathcal{P}^{(2)}(t) + \mathcal{P}^{(3)}(t)... \tag{1.7}$$

where $\mathcal{P}^{(n)} \propto \mathcal{E}^n$. This proportionality relationship can be expressed by means of the $n - th$ order susceptibility:

$$\mathcal{P}(t) = \epsilon_0 \left[\chi^{(1)} \mathcal{E}(t) + \chi^{(2)} \mathcal{E}^2(t) + \chi^{(3)} \mathcal{E}^3(t)... \right] \tag{1.8}$$

In the case of scalar susceptibility, taking into account a monochromatic wave on the form

$$\begin{aligned}
\mathcal{E}(t) &= \frac{1}{2} E(\omega) e^{i\omega t} + \frac{1}{2} E^*(\omega) e^{i\omega t} \\
\mathcal{P}(t) &= \frac{1}{2} P(\omega) e^{i\omega t} + \frac{1}{2} P^*(\omega) e^{i\omega t}
\end{aligned} \tag{1.9}$$

and considering only the first and third order terms of the Eq. (1.8), one obtains the following expression for the polarization

$$P(\omega) = \epsilon_0 \left[\chi^{(1)}(\omega;\omega) + \frac{3}{4} \epsilon_0 \chi^{(3)}(\omega;\omega,-\omega,\omega) |E(\omega)|^2 \right] E(\omega) \tag{1.10}$$

where $\chi^{(1)}(\omega;\omega)$ and $\chi^{(3)}(\omega;\omega,-\omega,\omega)$ are responsible for the one photon and three photon processes respectively. By this expression it is possible to calculate the complex refractive index $n_c = n - iK$, with n the refractive index and K the extinction coefficient defined by [19]

$$P(\omega) = \epsilon_0 \left[n_c^2(\omega) - 1 \right] E(\omega) \tag{1.11}$$

8

For semiconductor materials in which $n \gg K$, the approximation $(n-iK)^2 \approx n(n - i2K)$ holds. The refractive index is then given by

$$
\begin{aligned}
n &\approx \sqrt{1 + Re\chi^{(1)}(\omega;\omega) + \frac{3}{4}Re\chi^{(3)}(\omega;\omega,-\omega,\omega)|E(\omega)|^2} \\
&\approx \sqrt{1 + Re\chi^{(1)}(\omega;\omega)} + \frac{3Re\chi^{(3)}(\omega;\omega,-\omega,\omega)}{8\sqrt{1 + Re\chi^{(1)}(\omega;\omega)}|E(\omega)|^2} \\
&= n_0 + n_2|E(\omega)|^2
\end{aligned}
\tag{1.12}
$$

with

$$
\begin{aligned}
n_0 &= \sqrt{1 + Re\chi^{(1)}(\omega;\omega)} \\
n_2 &= \frac{3Re\chi^{(3)}(\omega;\omega,-\omega,\omega)}{8n_0}
\end{aligned}
\tag{1.13}
$$

that holds for small nonlinear effects $(n_0 \gg n_2|E(\omega)|^2)$. Equivalently, the extinction coefficient can be expressed as

$$
\begin{aligned}
K &\approx -\frac{Im\chi^{(1)}(\omega;\omega)}{2n_0} - \frac{3Im\chi^{(3)}(\omega;\omega,-\omega,\omega)}{8n_0}|E(\omega)|^2 \\
&= K_0 + K_2|E(\omega)|^2
\end{aligned}
\tag{1.14}
$$

where

$$
\begin{aligned}
K_0 &= -\frac{Im\chi^{(1)}(\omega;\omega)}{2n_0} \\
K_2 &= -\frac{3Im\chi^{(3)}(\omega;\omega,-\omega,\omega)}{8n_0}
\end{aligned}
\tag{1.15}
$$

Finally, the single and two photon absorption coefficients are defined by means of the extinction coefficient K_0 and K_2 as

$$
\alpha = 2\omega K_0/c
\tag{1.16}
$$

$$
\beta = 2\omega K_2/c
\tag{1.17}
$$

where β is in unit of m/W.

This analysis explains the physics of third-order polarization, and how Kerr and two photon absorption are related to the third-order susceptibility.

1.4　The plasma effect

As previously explained, a secondary effect of TPA is the plasma effect induced by carriers generation. The excess of charges modifies the optical properties of the material causing absorption as well as change in the refractive index. These affects can be suitably described by means of the following Drude model [20], [21]

$$\epsilon' = \epsilon - \frac{\omega_p^2}{\omega^2} + i\frac{\omega_p^2}{\omega^2 \tau_r} \tag{1.18}$$

with ω the frequency of the incident light, ϵ the linear dielectric constant, τ_r the carrier relaxation time, and ω_p the plasma frequency defined as

$$\omega_p = \sqrt{\frac{e^2 N}{\epsilon_0 m^*}} \tag{1.19}$$

where e is the elementary charge, N the carrier density, ϵ_0 the dielectric constant of the vacuum, and m^* the effective mass of the charges. The imaginary part of the Eq. (1.18) accounts for the losses with an absorption coefficient given by

$$\alpha_f = \frac{\omega_p^2}{\omega^2 \tau_r} \tag{1.20}$$

The real part of the Eq.(1.18) models the change index induced by free carrier dispersion. In fact, from Eq. (1.18) the index modulation can be obtained as follows

$$n' = \sqrt{\epsilon - \frac{\omega_p^2}{\omega^2}} \approx n_0 - \frac{\omega_p^2}{2n_0\omega^2} = n_0 + \Delta n_{plasma} \tag{1.21}$$

The Eq. (1.21) highlights that owing to the amount of generated charges, the refractive index decreases linearly with respect to the carriers density. The time scale of the effects inherent to the free carriers generation is related to the recombinations and diffusion processes that, in turn, depend on the material engineering and geometrical features of the structure.

1.5 Thermal effects

The absorption of incident power from matter is always related to a generation of thermal energy. The carriers generated by two photon absorption, when recombine, transfer energy to the material in the form of heat. Because of the increasing of the temperature, the optical properties of the material can be changed, manifesting as a modulation of the refractive index that can increase or decrease according to the material type. Thereby, thermal effects are responsible for strong nonlinearities that are often parasitic or unwanted. The time scale of the thermal nonlinearity is very long, of the order of $100\mu s$, i.e. much larger than the characteristic temporal scale of the pulses involved in optical signal processes.

The phenomenological dependence of the index from the temperature can be expressed as

$$n = n_0 + \frac{\partial n}{\partial T}T_1 \qquad (1.22)$$

where $\partial n/\partial T$ is the modulation of the index with respect to the temperature T, and $T_1 = T - T_0$ is the change of the temperature induced by a heat source. The differential equation that governs the temperature evolution in the time for a given source $I(r)$ (measured in unit of W/m^2) is the heat transport equation:

$$\rho_0 C \frac{\partial T_1}{\partial t} - k\nabla^2 T_1 = \alpha I(r) \qquad (1.23)$$

where $\rho_0 C$ is the heat capacity per unit of volume and is measured in units of $J/m^3 K$, ρ_0 the material density, and C the heat capacity per unit mass. k is the thermal conductivity measured in units of W/mK, and α the linear absorption coefficient. By means of the Eq. (1.23) the change in the refractive index can be evaluated in any point of the material. Importantly, due to the fact that thermal effects lead to a degradation of the performances, they must be avoided by lowering the power level of the used optical signals.

1.6 Analytical investigation of Kerr and TPA effects for TE polarized light

The majority of the devices that are analyzed and designed within this study exploit the strong potential of nonlinear effects in semiconductor materials. To enhance these effects, nanophotonic periodic structures are taken into account. These structures, in fact, for strong light confinement, can exhibit ultrafast all-optical signal processing with relatively low power consumption. To model the nonlinear dynamics that occurs in structures interested by TE polarized light such as, for example, photonic crystals in a membrane of high index material, it is useful to extend the previous formalism to the case in which the electric field has two components in the plane of the crystal. To this end, the starting point is the wave equation

$$\nabla^2 \underline{\mathcal{E}} - \frac{1}{c^2} \frac{\partial^2 \underline{\mathcal{E}}}{\partial t^2} = \mu_0 \frac{\partial^2 \underline{\mathcal{P}}^{(3)}}{\partial t^2} \tag{1.24}$$

with $c = c_0/n(\mathbf{r})$, c_0 the speed of light in the vacuum, and n the linear refractive index (note that semiconductors as Silicon or GaAs are linearly isotropic). In the (x, z) plane of the crystal the Eq. (1.24) is separated in the two following equations

$$\nabla^2 \mathcal{E}_x - \frac{1}{c^2} \frac{\partial^2 \mathcal{E}_x}{\partial t^2} = \mu_0 \frac{\partial^2 \mathcal{P}_x^{(3)}}{\partial t^2} \tag{1.25}$$

$$\nabla^2 \mathcal{E}_z - \frac{1}{c^2} \frac{\partial^2 \mathcal{E}_z}{\partial t^2} = \mu_0 \frac{\partial^2 \mathcal{P}_z^{(3)}}{\partial t^2} \tag{1.26}$$

In section 1.3, the nonlinear third-order effects have been described by an isotropic susceptibility $\chi^{(3)}$. However, semiconductor materials such as Silicon or GaAs, have cubic symmetry and then their nonlinear susceptibility is a tensor with three independent components [22]. Therefore, for a cubic crystal the nonlinear third-order polarizations are given by

$$
\begin{aligned}
\mathcal{P}_x^{(3)}(t) &= \frac{3}{8}\epsilon_0 \left(\chi_1^{(3)} |E_x|^2 E_x + \chi_2^{(3)} E_z^2 E_x^* + 2\chi_3^{(3)} |E_z|^2 E_x \right) e^{-i\omega t} + cc. \\
\mathcal{P}_z^{(3)}(t) &= \frac{3}{8}\epsilon_0 \left(\chi_1^{(3)} |E_z|^2 E_z + \chi_2^{(3)} E_x^2 E_z^* + 2\chi_3^{(3)} |E_x|^2 E_z \right) e^{-i\omega t} + cc.
\end{aligned}
\tag{1.27}
$$

with $\chi_1^{(3)} = \chi_{xxxx}^{(3)} = \chi_{zzzz}^{(3)}$, $\chi_2^{(3)} = \chi_{xzxz}^{(3)} = \chi_{zxzx}^{(3)}$, and $\chi_3^{(3)} = \chi_{xxzz}^{(3)} = \chi_{zzxx}^{(3)}$ the susceptibility values along the crystalline axes of the semiconductor. In Eq. (1.27) the terms multiplied for $\chi_2^{(3)}$ can be written in the following form:

$$E_z^2 E_x^* = |E_z|^2 e^{i2\phi_z}\frac{E_x}{E_x}E_x^* = |E_z|^2 E_x e^{-i2\phi}$$
$$E_x^2 E_z^* = |E_x|^2 e^{i2\phi_x}\frac{E_z}{E_z}E_z^* = |E_x|^2 E_z e^{i2\phi} \tag{1.28}$$

with $\phi(t) = \phi_x(t) - \phi_z(t)$ the phase difference. The Eqs. (1.28) yield

$$\mathcal{P}_x^{(3)}(t) = \frac{3}{8}\epsilon_0 E_x \left(\chi_1^{(3)}|E_x|^2 + \chi_2^{(3)}|E_z|^2 e^{-i2\phi} + 2\chi_3^{(3)}|E_z|^2\right) e^{-i\omega t} + cc.$$
$$\mathcal{P}_z^{(3)}(t) = \frac{3}{8}\epsilon_0 E_z \left(\chi_1^{(3)}|E_z|^2 + \chi_2^{(3)}|E_x|^2 e^{i2\phi} + 2\chi_3^{(3)}|E_x|^2\right) e^{-i\omega t} + cc. \tag{1.29}$$

By introducing the Eqs. (1.29) in the wave equations (1.25-1.26) and using the paraxial approximation:

$$\left|\frac{\partial^2 E_x}{\partial t^2}\right| \ll 2\omega\left|\frac{\partial E_x}{\partial t}\right|$$
$$\left|\frac{\partial^2 a_z}{\partial t^2}\right| \ll 2\omega\left|\frac{\partial E_z}{\partial t}\right| \tag{1.30}$$

one obtains

$$\frac{\partial E_x}{\partial t} = iE_x\left(\chi_1|E_x|^2 + \chi_2|E_z|^2 e^{-i2\phi} + \chi_3|E_z|^2\right)$$
$$\frac{\partial E_z}{\partial t} = iE_z\left(\chi_1|E_z|^2 + \chi_2|E_x|^2 e^{i2\phi} + \chi_3|E_x|^2\right) \tag{1.31}$$

where the coefficients χ_1, χ_2 and χ_3 have been defined as follows

$$\chi_1 = \frac{3\omega}{8nc_0}\chi_1^{(3)} \qquad \chi_2 = \frac{3\omega}{8nc_0}\chi_2^{(3)} \qquad \chi_3 = \frac{3\omega}{4nc_0}\chi_3^{(3)} \tag{1.32}$$

1.6.1 Analysis of the nonlinear system with Kerr effect

In the case of materials in which the Kerr effect is dominant, the third-order susceptibility takes real values. From Eqs. (1.31) and the corresponding conjugate equations one has

$$\frac{\partial|E_x|^2}{\partial t} = 2\chi_2|E_x|^2|E_z|^2\sin(2\phi)$$
$$\frac{\partial|E_z|^2}{\partial t} = -2\chi_2|E_x|^2|E_z|^2\sin(2\phi) \tag{1.33}$$

13

from which it follows that $I_e = |E_x|^2 + |E_z|^2$ is a conserved quantity, i.e. $\partial I_e / \partial t = 0$. With the ansatz

$$E_x = s_x \sqrt{\eta_x} e^{i\phi_x} \qquad E_z = s_z \sqrt{\eta_z} e^{i\phi_z} \qquad (1.34)$$

by the changes $\eta_x = \eta$, $\eta_z = I_e - \eta$ and $\phi = \phi_x - \phi_z$, from the first of the Eqs. (1.33) one obtains the equation of motion for η:

$$\dot{\eta} = 2\chi_2 \eta (I_e - \eta) \sin(2\phi) \qquad (1.35)$$

with $\dot{\eta} = \partial \eta / \partial t$. Furthermore, by replacing the relationships (1.34) into Eqs. (1.33) and equaling real and imaginary part one has

$$\begin{aligned} \dot{\phi}_x &= \chi_1 \eta_x + \chi_2 \, \eta_z \cos(2\phi) + \chi_3 \eta_z \\ \dot{\phi}_z &= \chi_1 \eta_z + \chi_2 \, \eta_x \cos(2\phi) + \chi_3 \eta_x \end{aligned} \qquad (1.36)$$

from which it follows the equation of motion for the phase:

$$\dot{\phi} = I_e(\chi_3 - \chi_1) + 2\eta(\chi_1 - \chi_3) + \chi_2(I_e - 2\eta)\cos(2\phi) \qquad (1.37)$$

The Hamiltonian H_r of the system (i.e. the conserved quantity so that $\partial H_r / \partial t = 0$) results to be

$$H_r = \frac{\chi_1}{2}(2\eta^2 - 2\eta I_e + I_e^2) + \chi_2 \eta(I_e - \eta)\cos(2\phi) + \chi_3 \eta(I_e - \eta) \qquad (1.38)$$

and the motion of the variables η and ϕ can be obtained as

$$\dot{\eta} = -\frac{\partial H_r}{\partial \phi} \qquad \dot{\phi} = \frac{\partial H_r}{\partial \eta} \qquad (1.39)$$

In Figs. (1.2) and (1.3) the phase plane for different ratio $\chi_1/\chi_j, j = 2, 3$ is shown. When the values of χ_2 and χ_3 are some order of magnitude smaller than χ_1, the dynamical system has points of equilibrium at multiples of $\pi/2$. The points at odd multiples of $\pi/2$ are centers, where the equilibrium is stable. Conversely, the points at even multiples of $\pi/2$ are saddle ones (see Fig. 1.2), and then they give rise to an instability of polarization. For χ_2 and χ_3 of the same order of magnitude than χ_1 there are still the points of equilibrium at multiples of $\pi/2$ but they are all points of stability (see Fig. 1.3).
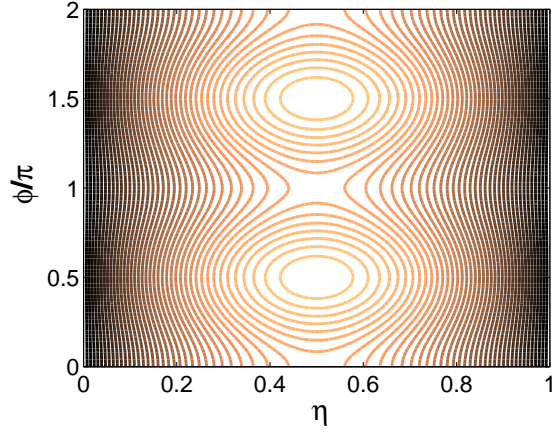
Figure 1.2: Phase plane corresponding to level curves of Eq. (1.39) when $\chi_2 = 0.1\chi_1$ and $\chi_3 = 0.01\chi_1$. The system shows equilibrium points at integer multiples of $\pi/2$ with $\eta = I_e/2$. The points at odd multiples of $\pi/2$ are centers, whereas those at even multiples are saddle points.
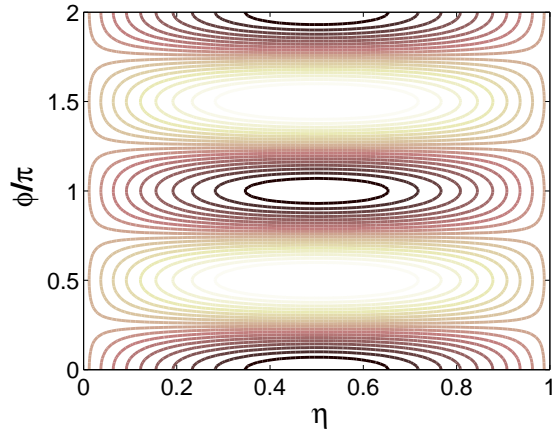
Figure 1.3: Phase plane corresponding to level curves of Eq. (1.39) when $\chi_2 = \chi_1$ and $\chi_3 = \chi_1$. The system still has equilibrium points at multiples of $\pi/2$ but they are all points of stable equilibrium.

In the framework of this thesis it is assumed to work within the polarization stability regime described in Fig. 1.3, that means to consider materials where the susceptibility values χ_1, χ_2 and χ_3, are almost of the same order. In fact, it is reasonable to assume that in photonic crystal cavities realized in semi-

15

conductors, the condition of polarization stability is satisfied and then that the electromagnetic field is locally linearly polarized (this assumption has been verified by means of numerical simulations of the electric field polarization inside some kinds of cavities). In this case, the third-order polarization induced by Kerr effect takes a trivial form, so that the Eqs. (1.29) are significantly simplified neglecting the phase mismatch between the electric field components and can be treated as equations with isotropic susceptibility.

1.6.2 Study in presence of dissipative third-order non-linearities

When the dissipative effects inherent to third-order polarization are taken into account, the values of the susceptibility are complex with an imaginary part that represents the losses induced by two photon absorption, i.e. $\chi_j = \chi_{jR} + i\chi_{jI}, j = 1, 2, 3$. As explained in the previous section, when locally linearly polarized light is treated, the third-order susceptibility takes a drastically simplified form and the Eqs. (1.29) become

$$
\begin{aligned}
\mathcal{P}_x^{(3)} &= \frac{3}{8}\epsilon_0 \left(\chi_R^{(3)} + i\chi_I^{(3)} \right) \left(|E_x|^2 + |E_z|^2 \right) E_x e^{-i\omega t} + cc. \\
\mathcal{P}_z^{(3)} &= \frac{3}{8}\epsilon_0 \left(\chi_R^{(3)} + i\chi_I^{(3)} \right) \left(|E_x|^2 + |E_z|^2 \right) E_z e^{-i\omega t} + cc.
\end{aligned}
\tag{1.40}
$$

Replacing these expressions in the Eqs. (1.25) and (1.26) gives

$$
\begin{aligned}
\frac{\partial E_x}{\partial t} &= i\frac{3\omega}{8n} \left(\chi_R^{(3)} + i\chi_I^{(3)} \right) I_e E_x \\
\frac{\partial E_z}{\partial t} &= i\frac{3\omega}{8n} \left(\chi_R^{(3)} + i\chi_I^{(3)} \right) I_e E_z
\end{aligned}
\tag{1.41}
$$

with $I_e = |E_x|^2 + |E_z|^2$. From the corresponding conjugate equations, it is easy to obtain a rate equation that describes the losses as a function of the time:

$$
\frac{\partial I_e}{\partial t} = -\frac{3\omega\chi_I^{(3)}}{4n^2}I_e^2
\tag{1.42}
$$

By properly defining $I = \epsilon_0 c_0 n/2 I_e$ with I the optical intensity, the Eq. (1.42) yields

$$
\frac{\partial I}{\partial t} = -\frac{3\omega\chi_I^{(3)}}{2\epsilon_0 c_0 n^3}I = -\beta_t I^2
\tag{1.43}
$$

where β_t describes the strength of the nonlinear process and can be related to the known two photon absorption coefficient β (accounting for the losses per unit length) by $\beta_t = \beta c_0 / n$. Free carriers absorption induced by TPA, in turn, can be described by the following rate equation

$$\frac{\partial N}{\partial t} = -\frac{1}{2\hbar\omega c_0}\frac{\partial I}{\partial t} - \frac{N}{\tau_r} \qquad (1.44)$$

where τ_r is the recovery time of the charges (typically of the order of few picoseconds), and $\hbar = 6.626 \times 10^{-34} Js$ is the Planck constant. Therefore, by using the Eq. (1.43) one obtains

$$\frac{\partial N}{\partial t} = \frac{\beta_t}{2\hbar c_0 \omega} I^2 - \frac{N}{\tau_r} \qquad (1.45)$$

From this analytical study for TE polarized light in nonlinear regime, it becomes quite feasible to obtain the governing equations that can be discretized by means of time domain numerical methods.

1.7 Summary

In this first chapter the main nonlinear effects in standard semiconductors have been introduced. The purpose of such a study has been to mathematically describe Kerr and TPA nonlinearities in a general way and then to extend the study to polarized light with the aim to implement numerical tools able to model the nonlinear effects in photonic crystal devices.

Chapter 2

Photonic crystals

2.1 Introduction

One purpose of this thesis is to extend the analysis of the third-order nonlinearities to periodic structures, where the interaction between light and matter can be strongly improved and the nonlinear effects enhanced. To this end, in this chapter a description of widespread periodic structures is developed. In particular, photonic crystal structures are introduced and their relevant properties era described. Furthermore, the most important components such as photonic crystal slabs, waveguides and cavities are analyzed. Finally, to highlight the operative contribution that such periodic structures can offer in the manipulation of the optical signals, an example of photonic crystal filtering process is demonstrate.

2.2 Properties of the periodic structures

Photonic crystals (PhC), studied for the first time by Yablonovitch [15] and John [16], are periodic arrangements of materials with different refractive index [17], [18]. This spatial distribution gives rise to a periodic dielectric function that, as for the periodic potential generated by regular arrays of atoms and molecules, produces an energy band structure in which band gaps may occur. The presence of photonic band gaps forbids the propagation for specific frequencies and in certain directions. This feature makes the
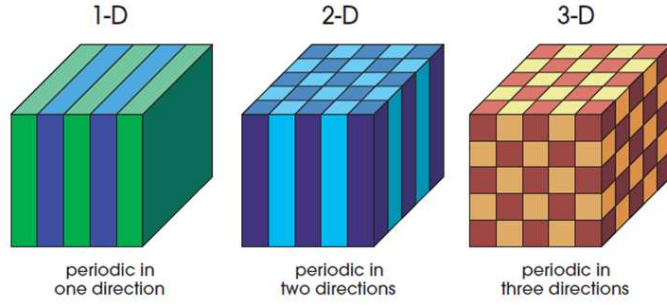
Figure 2.1: Examples of 1D, 2D, 3D PhCs [17].

photonic crystals an excellent framework to engineer the materials for the optical control and manipulation. Fig. 2.1 shows three different examples of how two materials can be stacked to obtain 1D, 2D and 3D periodicity. The spatial period is named *lattice constant* and it is chosen on the order of the wavelength of the incident light involved in the optical process. The discrete translational symmetry of a photonic crystal makes possible to classify the electromagnetic modes with respect to their wavevectors $\mathbf{k}$. The modes can be expanded in Bloch form consisting of a plane wave modulated by a periodical function that takes into account the periodicity of the crystal [17]. Therefore, for example, the magnetic field into a PhC can be written as

$$\mathbf{H}_k(\mathbf{r}) = e^{i\mathbf{k}\cdot\mathbf{r}}\mathbf{u}(\mathbf{r}) = e^{i\mathbf{k}\cdot\mathbf{r}}\mathbf{u}(\mathbf{r} + \mathbf{R}) \qquad (2.1)$$

where $\mathbf{R}$ is the spatial vector that accounts for the lattice periodicity and it is named *lattice vector*. Defining the *reciprocal lattice vector* $\mathbf{G}$ as the vector that satisfies the relationship $exp(i\mathbf{G}\cdot\mathbf{R}) = 1$, from Eq. (2.1) it follows that a mode with wavevector $\mathbf{k}$ and a mode with wavevector $\mathbf{k} + \mathbf{G}$ are the same mode. This means that it is convenient to restrict the attention to a finite zone in reciprocal space (space of $\mathbf{k}$) in which it is not possible to get from one part to another of the lattice by adding any $\mathbf{G}$; this zone is known as the *Brillouin zone*. Fig 2.2 shows an example of triangular lattice (left), of its reciprocal space (central), and of the corresponding Brillouin zone (right).

19
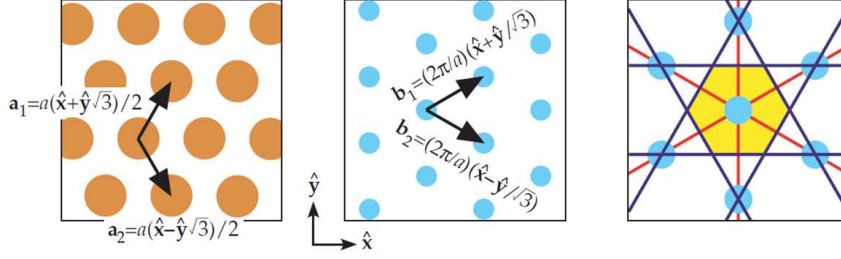
Figure 2.2: The Real space (Left), the corresponding reciprocal space (center), and the Brillouin zone (Right) of a triangular lattice [17].

2.3 Dielectric multilayers

In order to give an intuitive understanding of the photonic bands, band gaps, and Bloch modes, it can be useful to examine a 1D crystal [18]. Fig. 2.3 shows a dielectric multilayers where the single layer has size a. The electromagnetic wave is considered linearly polarized in the y direction and propagating along the x axis in the direction perpendicular to the surface of the dielectric layers. The wave equation is then given by

$$\frac{c^2}{\epsilon(x)} \frac{\partial^2 E}{\partial x^2} = \frac{\partial^2 E}{\partial t^2} \tag{2.2}$$

where c is the light speed in the vacuum, and $\epsilon(x)$ the relative dielectric constant accounting for the spatial periodicity. Because $\epsilon(x)$ is a periodic function of x, i.e.

$$\epsilon(x + a) = \epsilon(x) \tag{2.3}$$

$\epsilon^{-1}(x)$ is also periodic and then it can be expanded in Fourier series as follows

$$\epsilon^{-1}(x) = \sum_{m-\infty}^{\infty} k_m e^{i\frac{2\pi m}{a}x} \tag{2.4}$$

where m is an integer and k_m are the Fourier coefficients. Since it is assumed that $\epsilon(x)$ is real, $k_{-m} = k_m^*$. The well-known Bloch's theorem that holds for the electronic eigenstates in a ordinary crystal, also holds for the description of electromagnetic waves in periodic structures. Therefore, the eigenmodes
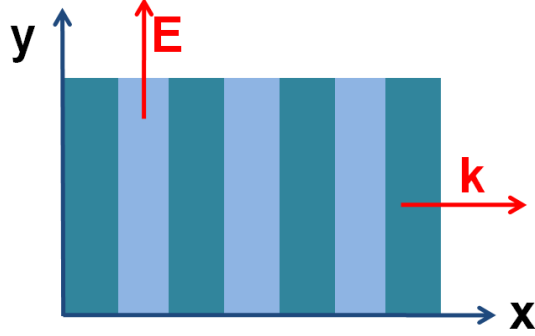
Figure 2.3: Multilayered structure (a). Dispersion relation for the 1D PhC (b) [18].

in the 1D photonic crystal can be characterized by a wavenumber k and expressed as

$$E(x,t) = u_k(x)e^{i(kx-\omega_k t)} \tag{2.5}$$

where ω_k denote the eigen-angular frequency, and $u_k(x)$ is a periodic function of x. The electric field can in turn be expanded as

$$E_k(x,t) = \sum_{m=-\infty}^{\infty} E_m e^{i\left(k+\frac{2\pi m}{a}\right)x - i\omega_k t} \tag{2.6}$$

with E_m the Fourier coefficients. For a simple analysis, it can be assumed that the components with $m = 0, \pm 1$ are dominant in Eq. (2.4), so that $\epsilon^{-1}(x)$ can be approximated as follows

$$\epsilon^{-1}(x) \approx k_0 + k_1 e^{i\frac{2\pi}{a}x} + k_{-1}e^{-i\frac{2\pi}{a}x} \tag{2.7}$$

By replacing Eqs. (2.4) and (2.6) in the wave Eq. (2.2), the following relation is obtained

$$k_1\left[k + \frac{2(m-1)\pi}{a}\right]^2 E_{m-1} + k_{-1}\left[k + \frac{2(m+1)\pi}{a}\right]^2 E_{m+1} \approx$$
$$\approx \left[\frac{\omega_k^2}{c^2} - k_0\left(k + \frac{2m\pi}{a}\right)^2\right]E_m \tag{2.8}$$

that evaluated for $m = 0$ gives

$$E_0 \approx \frac{c^2}{\omega_k^2 - k_0 c^2 k^2} \left[k_1 \left(k - \frac{2\pi}{a} \right)^2 E_{-1} + k_{-1} \left(k + \frac{2\pi}{a} \right)^2 E_1 \right] \qquad (2.9)$$

and fro $m = -1$

$$E_{-1} \approx \frac{c^2}{\omega_k^2 - k_0 c^2 (k - 2\pi/a)^2} \left[k_1 \left(k - \frac{4\pi}{a} \right)^2 E_{-2} + k_{-1} k^2 E_0 \right] \qquad (2.10)$$

If $k \approx |k - 2\pi/a|$ (i.e. $k \approx \pi/a$), and if $\omega_k^2 \approx k_0 c^2 k^2$, then E_0 and E_{-1} are dominant in Eq. (2.6). In this case, by neglecting the other terms, the following set of equations is obtained

$$\left(\omega_k^2 - k_0 c^2 k^2 \right) E_0 - k_1 c^2 \left(k - \frac{2\pi}{a} \right)^2 E_{-1} = 0$$

$$-k_{-1} c^2 E_0 + \left[\omega_k^2 - k_0 c^2 \left(k - \frac{2\pi}{a} \right)^2 \right] E_{-1} = 0 \qquad (2.11)$$

This linear system has non-trivial solutions when the determinant of the associated matrix vanishes. This request, by replacing $h = k - \pi/a$, yields

$$\omega_k \approx \frac{\pi c}{a} \sqrt{k_0 \pm |k_1|} \pm \frac{ac}{\pi |k_1| \sqrt{k_0}} \left(k_0^2 - \frac{|k_1|^2}{4} \right) h^2 \qquad (2.12)$$

as far as $|h| \ll \pi/a$. Therefore, Eq. (2.12) describes a dispersive relation (ω versus k) in which, due to spatial modulation (accounted for the term k_1), a band gap is open for frequencies in the interval

$$\frac{\pi c}{a} \sqrt{k_0 - |k_1|} < \omega < \frac{\pi c}{a} \sqrt{k_0 + |k_1|} \qquad (2.13)$$

2.4 Photonic crystal slabs

In recent years a class of photonic crystals known as photonic crystals slabs have been intensively investigated, in particular thanks to sophisticated technologies such as electron beam and lithography recently developed for their fabrication. Photonic crystal slabs are two-dimensionally periodic dielectric structures that have a band gap for propagation in a plane and that use index
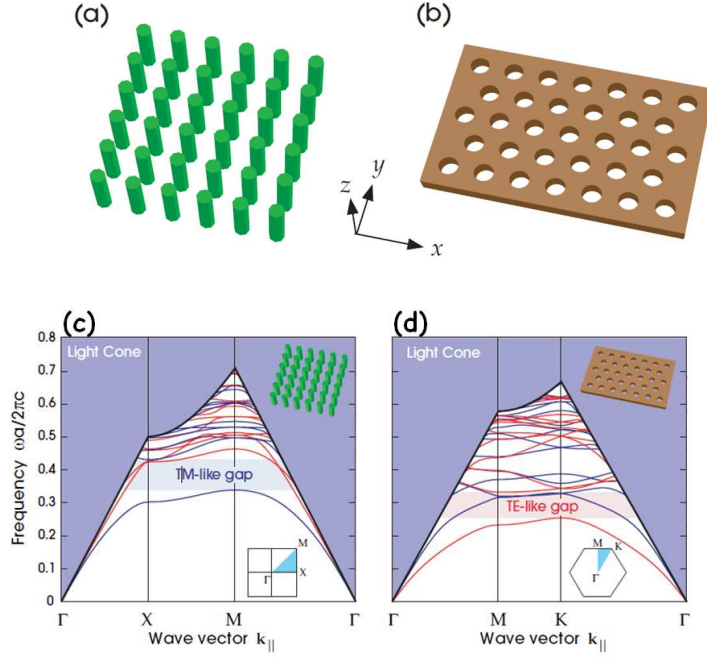
Figure 2.4: Examples of photonic crystal slabs. Square lattice of dielectric rods in air (a). Triangular lattice of air holes in bulk dielectric material (b). Rod slab (c) and hole slab (d) bands diagram. The blue shaded area is the light cone. Below the light cone are the guided bands localized to the slab: blue and red bands indicate the TM and TE modes respectively [17].

guiding to confine light in the third dimension. Examples of such structures are shown in Fig. 2.4. Because of translational symmetry in two directions, the in-plane wavevector $k_{||} = (k_x, k_y)$ is conserved, whereas the vertical k_z wavevector is not conserved. Fig. 2.4 (c)-(d) shows the band diagram (ω versus k) of a triangular lattice photonic cristal slab of air holes in dielectric (Fig. 2.4 (c)), and of a square lattice photonic crystal slab of rods in air (Fig. 2.4 (d)). The extended modes propagating in air form a light cone when $\omega \leq c|k_{||}|$. Below the light cone, due to higher index, the modes are tight confined inside the slab, and they decay exponentially in vertical direction. Because of the symmetry of the structure, the modes can be classified as TE-like (transverse electric) which have two electric components in the plane of the crystal and one magnetic component in the vertical direction,

and TM-like (transverse magnetic) which have two magnetic components in the plane of the crystal and one electric component in the vertical direction. As displayed in Fig. 2.4 (c)-(d), the rods slabs exhibit TM gaps (red lines), and the hole slabs favor TE gaps (blue lines). The presence of gaps makes possible to control the flow of light by means of defects. Defects can be introduced in PhC membranes by removing, for example, rods in a square lattice of dielectric rods, or holes in a triangular lattice of air holes. This breaks the periodicity of the crystal giving rise to localized states inside the band gap. Thereby, by means of defects, it become possible to trap or guide the light as the field is tight confined inside the band gap and can not escape toward the crystal.

2.5 Tuning the dispersion in photonic crystal waveguides

In this study some different topologies of PhC slabs based devices able to manipulate both TM and TE polarized light are developed. In each configuration, light enters the structures by traveling toward waveguides realized by line defect into the photonic crystal. In this respect, it is very important is to ensure suitable features of light that travels in the waveguide such as group velocity and vertical confinement. Furthermore, it is essential to provide a specific coupling between waveguide and resonators to transfer the required amount of energy into the cavities. These attainments can easily be pursued by engineering the characteristics of the waveguides, with the advantage that the high flexibility offered by photonic crystals allows to realize fine tuned geometries.

Unlike conventional linear dielectric waveguides that operate by index confinement, waveguides realized in PhC slabs [4], by trapping the light into the band gap and by using the index confinement in the vertical direction, prohibit radiation losses. The dispersive features of the PhC waveguide can be tuned by means of some perturbations of the slab. One possibility is to create a decreased index waveguide by lowering the amount of high-index material in a PhC air holes slab. Fig. 2.5 shows the projected bands of a

(a) (b)
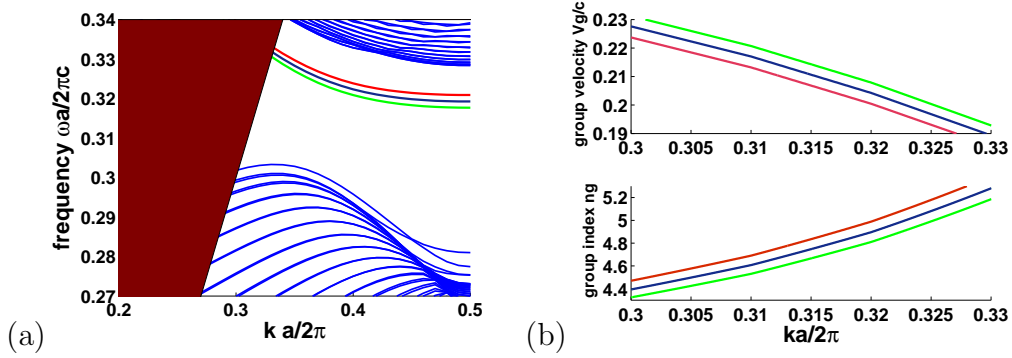
Figure 2.5: Projected band diagram of the TE modes for a line defect waveguide realized in a hole slab with thickness $200nm$ surrounded by air. The holes radius of the nearest rows are increased by $0.32a$ (green line), $0.33a$ (blue line), and $0.34a$ (red line) (a), resulting in a group velocity (group index) that decreases (increases) with the holes size (b).

waveguide realized in a triangular lattice PhC slab of air holes, where the hole radius of the two nearest rows in the waveguide is increased (plane wave simulations are performed by using the tool described in [23]). As it can be seen in Fig. 2.5 (a)-(b), an increase of the holes radius causes a shift of the cut-off frequency of the waveguide toward higher frequency and, simultaneously, induces a decrease of the group velocity v_g (or an equivalent increase of the group index defined as $n_g = c/v_g$) leading to the limit of slow light regime.

2.6 Localized light in photonic crystal cavities

In an optical cavity light can be stored for a long time and in a small volume, and the trapped field can reach very high levels of intensity. In particular, photonic crystal cavities, by exhibiting high Q factors and tight confinement of light in very small volumes, are an ideal environment to enhance light-matter interactions. The Q factor is defined as the ratio between the resonant frequency and the full width at half maximum (FWHM) of the cavity: $Q = \omega_0/\Delta\omega$. It represents the lifetime of the photons trapped inside the cavity

(a) (b)
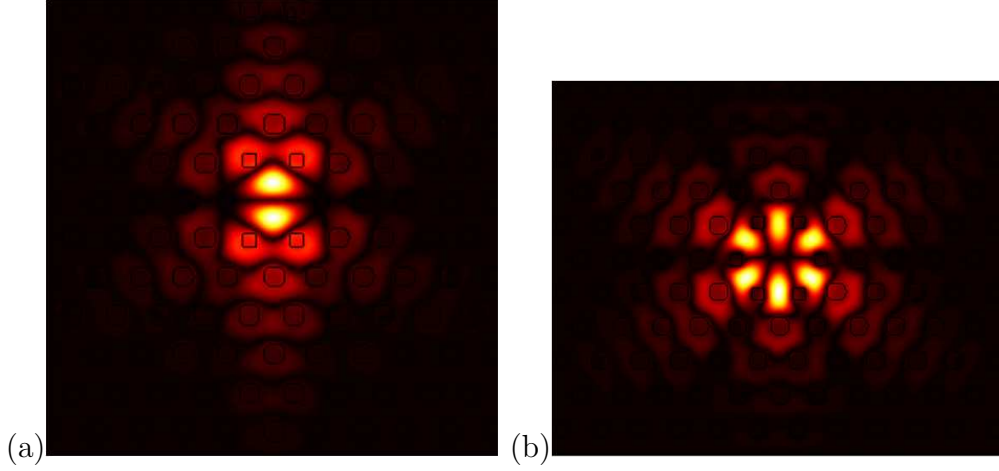
Figure 2.6: Profile of the modes in a monopole (a) and hexapole (b) cavity.

and then defines the time scale in which optical processes can work. The modal volume defined as $V = \int \epsilon(\mathbf{r})\mathbf{E}^2(\mathbf{r})d^3\mathbf{r} / \left[\epsilon(\mathbf{r})\mathbf{E}^2(\mathbf{r})\right]_{max}$, accounts for the spatial confinement of the energy stored inside the cavity. From this definitions it is straightforward to understand how the ratio Q/V determines the strength of the various cavity interactions. The cavity energy leaks out according to the following equation

$$\frac{\partial E(t)}{\partial t} = -\frac{\omega_0 E(t)}{Q_{tot}} \tag{2.14}$$

where E and ω_0 are the energy and the resonant frequency of the cavity, respectively. The total radiate power $(1/Q_{tot})$ can be decomposed into a vertical contribution $(1/Q_{vert})$ and an in-plane contribution $(1/Q_{hor})$ according to the following relation

$$\frac{1}{Q_{tot}} = \frac{1}{Q_{vert}} + \frac{1}{Q_{hor}} \tag{2.15}$$

The Q_{vert} accounts for inherent optical losses of the energy, as the in-plane losses can be reduced by increasing the number of PhC periods surrounding the cavity. When a cavity is coupled to a waveguide, the in-plane quality factor is mainly determined by the strength of the cavity to waveguide coupling. In fact, the bulk of light leaves the cavity via the waveguide, whereas the losses through the crystal remain very weak. In this case, the in-plain

quality factor Q_{hor} is referred as loaded quality factor Q_L. If the vertical quality factor is much higher than the loaded Q_L, from the Eq. (2.15) it results that the cavity lifetime is dominated by the losses through the waveguide. Thereby, the cavity lifetime is entirely accounted for the cavity to waveguide coupling coefficient Γ that, in this case, results to be related to the loaded quality factor through the relation $\Gamma = \sqrt{\omega_0/2Q_L}$. The strength of coupling, in turn, depends on the nearness between the resonator and the line defect as well as on dispersive features of the waveguide. In this respect, the design of high intrinsic quality factor Q_{vert} as well as the achievement of a suitable coupling Γ, become essential targets for the realization of optical structures. The optimization of the PhC cavities in terms of both intrinsic quality factor Q and modal volume V can be pursued by investigating different topologies. In this perspective, various kinds of defects can be realized by molding the geometrical features of the crystal [32], [33]. As examples of excellent flexibility offered by engineering the PhC geometry, two field profiles stored in isolated defects realized in a PhC triangular lattice slab of air holes are shown in Fig. 2.6. The defects are obtained by removing a single hole (monopole (a)) or by shifting the six nearest neighbor holes (hexapole (b)). By means of numerical calculations it has been demonstrate that the monopole cavity exhibits a Q factor of almost 10000, whereas the hexapole cavity reaches a Q factor of almost 150000 and exhibits an effective volume V of the order of cubic wavelength.

2.7   Design of photonic crystal structures

By composing PhC cavities and waveguides, and by tailoring the topologies of the crystal, it is possible to efficiently manipulate light. As an example, Fig. 2.7 shows a filter composed by a cavity and two waveguides in a 2D triangular lattice of air holes. As depicts in Fig. 2.7 (b) the cavity, realized by removing three adjacent holes, exhibits resonants modes inside the band gap of the crystal. When the wavelength of incoming light lies inside the linewidth of the resonator (determined by the loaded quality factor of the cavity), it is partially dropped toward the output ports and partially back reflected. The amount of energy that is guided through a given output port,

(a)

(b)

(c)
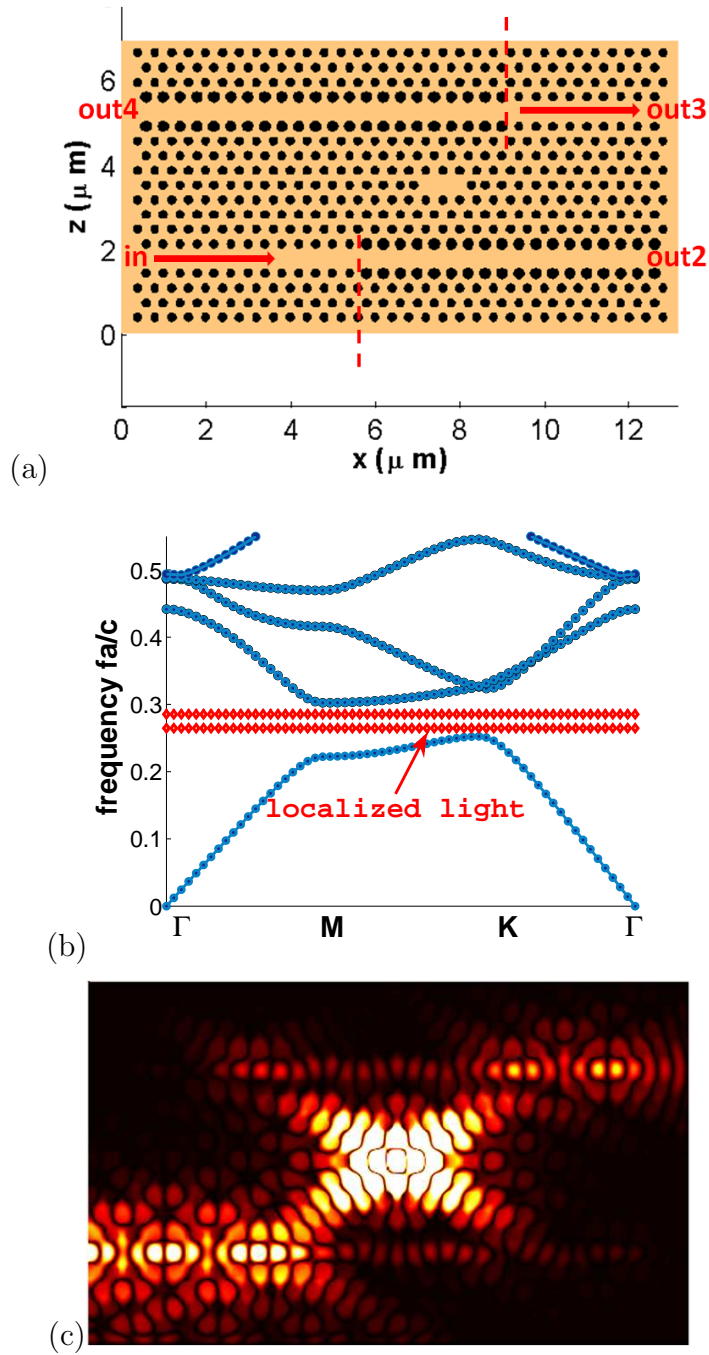
Figure 2.7: Filter topology (a). Localized modes of the cavity inside the PhC band gap (b). Snapshot of the H field obtained by means of FDTD simulations.

can be controlled by an artful design of the PhC topology. In this perspective, as suggested in [34] the filtering performances are successfully improved by modifying the radii of the edge holes in the waveguides. By exploiting the fact that light below the cut-off frequency can not entering the waveguides with largest holes, this design prevents light to travel toward ports 2 and 4, and ensure high drop efficiency toward port 3. In fact, with a careful design of the waveguides boundary barriers, the resonant tunneling filter has been demonstrated to achieve maximum drop efficiency of almost 100%.

2.8   Summary

In this chapter the relevant features of periodic structures have been analyzed with the purpose to describe an excellent framework where the flow of light can be controlled. An overview has been made about the description of different basic components such as photonic crystal slabs, cavities and waveguides. Especially, two dimensional PhC slabs have been taken into account because of the accessibility offered by current well-established standard fabrication processes. Tunability of the dispersion in PhC waveguides has been studied, and optical characteristics such as the mode profile, the Q factor and the modal volume of PhC cavities have been analyzed. Finally, the high flexibility that these periodic structures exhibit for the design of optical devices has been demonstrate.

Chapter 3

Photonic crystal devices working with Kerr nonlinearities

3.1 Introduction

In this chapter the Kerr effect is deeply studied. In particular, the bistable response typical of resonators based on Kerr materials is analyzed. Then it is shown how this characteristic behavior can be properly exploited to design optical devices. The main tool that is used to model and design these devices, is the nonlinear 2D finite difference time domain (FDTD) method. The well known linear FDTD scheme (described in appendix A) is developed to extract the linear characteristics of the structures. Then, the discretized equations are extended to simulate the Kerr nonlinearity. Finally, some photonic cystal topologies implementing optical devices such as switches and serial to parallel converters are modeled by means of the nonlinear code.

3.2 Optical bistability

Optical bistability is a behavior exhibited by resonant structures that have two different stable steady transmission states depending on the history of the input. Bistability occurs when the effects of nonlinear regime causes hys-

teresis in the transmission and reflection of the resonant system. A possible mechanism that gives rise to bistability is a strong dependence of the refractive index on the optical intensity, as it can occur in a high quality factor cavity realized in Kerr materials.

By considering the driven-damped model of a cavity discussed in [8] in the limit of dominant Kerr instantaneous response, the governing equation is then of the form

$$\frac{du}{dt} = i(\omega_0 - \omega_L)u - i\chi_{eff}|u|^2 u - \alpha u + \sqrt{\frac{\Gamma_c}{2}P_{in}} \tag{3.1}$$

where $|u|^2$ is the cavity energy, $\alpha \equiv \Gamma_{tot}/2$ is the loss coefficient, $\Gamma_{tot} = \omega_0/Q$ being the inverse cavity lifetime, $\Gamma_c = \omega_0(1/Q - Q_0)$ is the transmission or coupling coefficient, and ω_0, ω_L are the cold resonance and the laser frequency respectively. For theoretical analysis it is useful to rescale the model into dimensionless units with minimum number of parameters with unit lossy coefficient:

$$\frac{da}{d\tau} = i\delta a + i\chi|a|^2 a - a + S(\tau) \tag{3.2}$$

One can simply convert back to dimensional quantities using the following scaling

$$\tau = \alpha t, \quad a = \sqrt{\frac{|\chi_{eff}|}{\alpha}}u, \quad \delta = \frac{\omega_0 - \omega_L}{\alpha}, \quad S(\tau) = \sqrt{\frac{\Gamma_c}{2\alpha}P_{in}(\tau)} = \sqrt{\frac{2\Gamma_c}{\Gamma_{tot}^2}P_{in}(\tau)} \tag{3.3}$$

To be more general, the sign of nonlinearity can be $\chi = \pm 1$. The dynamics discussed below occurs for both signs of nonlinearity with suitable change of the detuning sign.

The steady state response $a = A =$ constant from constant excitation $P_i = S^2$ can be easily found in terms of normalized intracavity energy $P = |A|^2$ as

$$P_i = P\left[1 + (\delta + \chi P)^2\right] \tag{3.4}$$

The response is bistable for

$$|\delta| > \sqrt{3} \tag{3.5}$$
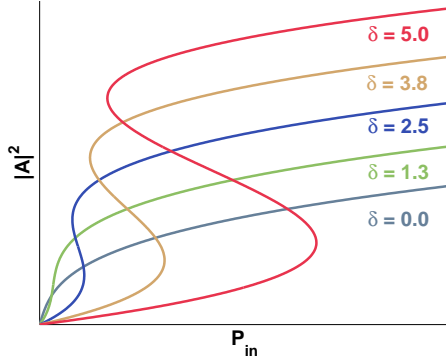
Figure 3.1: Bistable behavior.

and have knee values of the bistable response (such that $dP_i/dP = 0$) at intracavity levels $P = P^\pm$:

$$\chi = 1 \Rightarrow \delta < -\sqrt{3} \quad P^\pm = \frac{-2\delta \pm \sqrt{\delta^2 - 3}}{3}$$
$$\chi = -1 \Rightarrow \delta < -\sqrt{3} \quad P^\pm = \frac{2\delta \pm \sqrt{\delta^2 - 3}}{3}$$

(3.6)

If $\chi = 1$, a high optical intensity can lower the resonance frequency, so that when $\omega_L < \omega_0$ one has the tuning of the driving frequency. Two stationary intensity values then became possible. Since α is related to the response time of the cavity, the condition (3.5) implies that the frequency offset (i.e. the frequency detuning δ) must be sufficiently large compared with the resonator bandwidth. In Fig. 3.1 it is shown how the energy of the system evolves under increasing input power P_{in} for different detuning values. For $\delta < \sqrt{3}$ a bistable behavior is not allowed, therefore the cavity energy grows with the increasing of the input intensity. When $\delta > \sqrt{3}$, at low intensity there is only one possible value of the energy for a given input power, whereas for sufficiently high input power there exist two different energy values corresponding to the change of the resonator state. The lower and upper branch of the response coincide with two different states in which the resonator can reside depending on its previous state. For a low initial internal energy, as one moves to higher input intensities, the normalized energy in the cavity rises to a critical value and when the input power increases further, the energy jumps to a higher state and then continue to rise. On the other hand, if
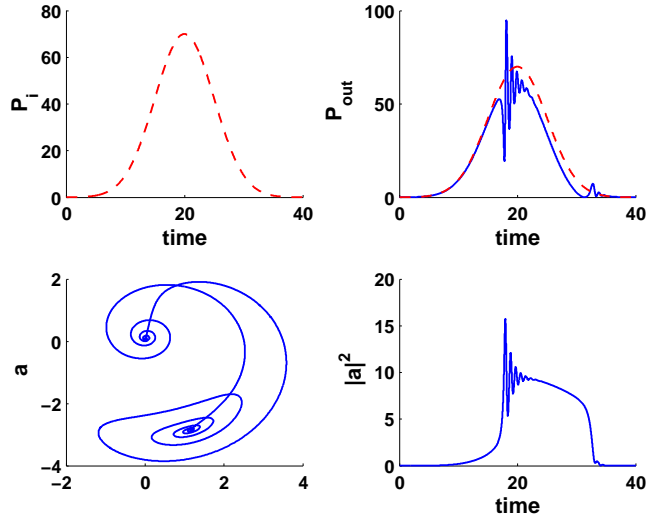
Figure 3.2: Bistable switching with relaxation oscillations on the leading edge of the pulse. Top left: driving Gaussian pulse. Top right: output transmitted pulse (blue curve) compared with input. Bottom right: internal cavity energy. Bottom left: phase-space $Re(a) - Im(a)$ reconstruction of the dynamics. Here $\delta \approx 7$.

the cavity is in an initial high level energy, with decreasing input power the internal energy decreases as well and then jumps to a lower value.

Linear stability analysis can be performed with the ansatz $a(t) = A + \delta a(t)$, which leads after linearization to the system for the unknown $\mathbf{a} = [\delta a\ \delta a^*]^T$:

$$\frac{d\mathbf{a}}{dt} = \begin{pmatrix} ib - 1 & i\chi P \\ -i\chi P & -(ib+1) \end{pmatrix} \mathbf{a} \qquad (3.7)$$

where has been set $b = \delta + 2\chi P$. The dynamics of the perturbation is ruled by the eigenvalues λ of the above matrix

$$\lambda = \lambda^\pm = -1 \pm \sqrt{P^2 - (\delta + 2\chi P)^2} \qquad (3.8)$$

The eigenvalues are either real on the negative slope branch of the bistable response and conjugate pairs on the positive slope branches. Clearly the eigenvalues rule the temporal evolution of the perturbation when a small deviation from the stationary state is imposed. In this case the cavity relaxes
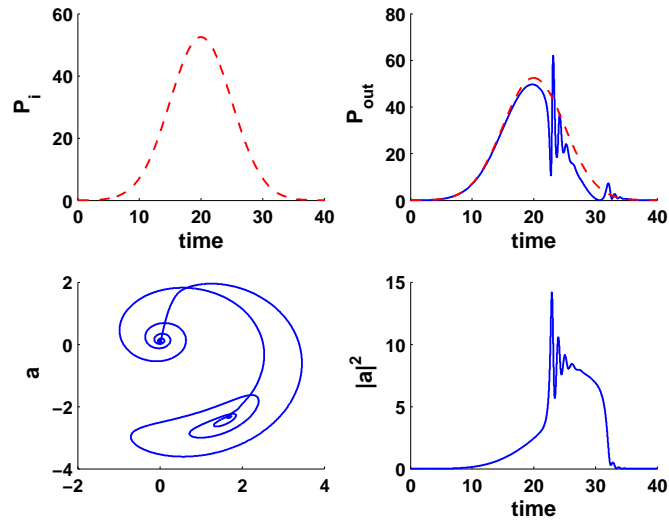
Figure 3.3: Same with relaxation oscillations on the trailing edge of the driving pulse.
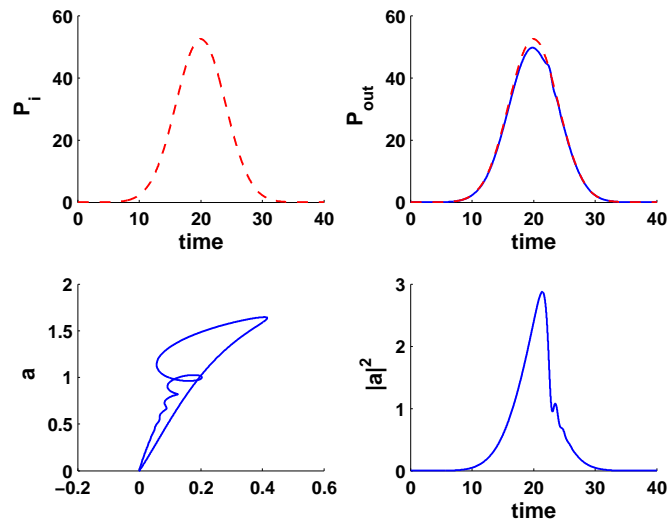
Figure 3.4: Same with relaxation oscillations on the trailing edge of the driving pulse.

to the stable branch of the stationary response with oscillations exhibiting a period $T_p = 2\pi |Im(\lambda)|$. Simple simulations based on numerical integration of

Eq. (3.2) with $P_i(t)$ being Gaussian pulse, shows that bistable jumps occurs with relaxation oscillations which can be manifested either on the leading or trailing edge of the pulse, depending on the peak value of the driving signal, as shown in Fig. 3.2 and 3.3. These figures show both the transmitted power $P_{out} = |\sqrt{P_i - a}|^2$ and the internal energy $|a|^2$, as well as a phase-space representation of the dynamics. In order for the relaxation oscillations to appear it seems rather crucial to have a driving pulse whose characteristic time (duration) is somehow longer than the cavity time constant (normalized to one in this scaling). As shown in Fig. 3.4 relaxation oscillations tend to disappear for shorter pulses. This kind of dynamics is visible also by means of finite difference time domain method (described in appendices A and B) as it is analyzed in the next section.

3.3   FDTD modeling of Kerr-type photonic crystal based devices

In order to model the bistable nonlinear behavior studied in the section 3.2, 2D finite difference time domain simulations involving nonlinear periodic structures are performed.

The domain analyzed is a photonic crystal composed of a square lattice of rods with index 3.4 in air [31]. The lattice constant is $600nm$ and the width of the rods is $150nm$. The crystal has a band gap for TM polarized modes for wavelength between $1300nm$ and $1800nm$ (see Fig. 3.5). Moreover, the material of the rods is considered to have a nonlinear behavior with a third order susceptibility $\chi^{(3)}$ arbitrarily chosen to be $0.08m^2/V^2$. For wavelengths inside the band gap, a waveguide can be created by removing a line of rods. Furthermore, as explained in chapter 2, when a defect is introduced into a periodic structure, high transmission state with a sharp and narrow resonance peak appears in the band gap of the crystal. Fig. 3.6 shows the structure composed of a waveguide and a cavity realized by removing three rods (a). In the same figure it is illustrated the corresponding resonant TM pattern of the cavity mode evaluated by means of the discrete fourier transform (DFT) at resonant frequency (b). In this topology the cavity is side-coupled to the
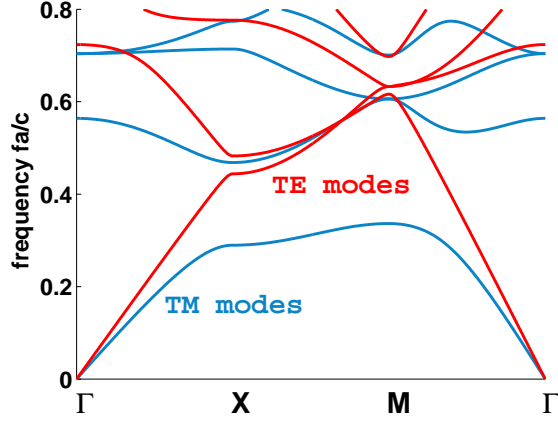
Figure 3.5: Photonic band structure for a square lattice of rods with index 3.4 in air. The crystal shows a complete band gap for TM polarized modes (blue curves), whereas the gap is closed for TE modes (red curves). The frequency is expressed as dimensionless ratio fa/c, where a is the lattice constant and c the speed of light. In the horizontal axis are reported the in-plane wavevector values at the edges of the irreducible Brillouin zone form Γ to X to M.

waveguide so, when the system is on resonance, the energy in the cavity increases abruptly and the transmission through the waveguide goes to zero. Specifically, the side-coupled cavity shows a resonance at $\lambda_0 = 1573nm$ with a loaded quality factor $Q = 297$ that corresponds to a decay constant $\tau = 2Q/\omega_0$ of almost $0.5ps$. The nonlinear dynamics can be suitably described by the following CMT model

$$\frac{da}{dt} = i\Delta\omega a - \frac{\omega_0}{2Q}a - i\omega_0\chi_{eff}|a|^2a + \sqrt{\frac{\omega_0}{2Q}}S \qquad (3.9)$$

In order to compare the FDTD results with the predicted CMT dynamics studied in the section 3.2, the effective value of the susceptibility in Eq. (3.9) has been defined as

$$\chi_{eff} = \frac{3\int \chi^{(3)}|A(r)|^4 dr}{8\left[\int \epsilon_r(r)|A(r)|^2 dr\right]^2} \qquad (3.10)$$
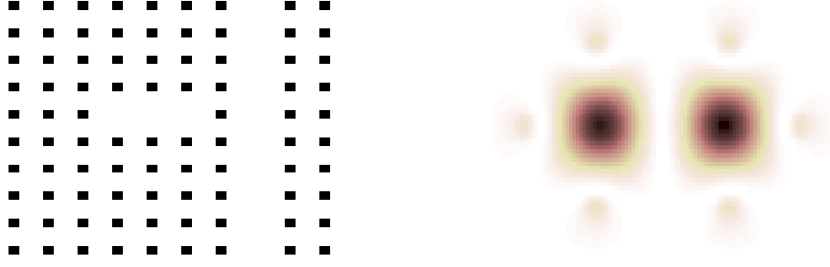
Figure 3.6: Left: photonic crystal topology of the domain simulated. Right: DFT calcuated pattern of the resonant TM mode at $\lambda_0 = 1573nm$.

The 2D-FDTD simulations are performed by discretizing, according to the method described in appendices A and B, the following TM equations

$$\mu_0 \frac{\partial H_z}{\partial t} = \frac{\partial E_y}{\partial x}$$
$$\mu_0 \frac{\partial H_x}{\partial t} = -\frac{\partial E_y}{\partial z}$$
$$\frac{\partial \left(\epsilon_0 \epsilon_r E_y + \epsilon_0 \chi^{(3)} |E_y|^2 E_y \right)}{\partial t} = \frac{\partial H_z}{\partial x} - \frac{\partial H_x}{\partial z}$$
(3.11)

 For a sufficient accuracy, a number of 19 cells for period have been chosen. The domain of simulation is surrounded by perfectly matched layer (PML) boundary conditions. The structure is excited by injecting a $10ps$ Gaussian pulse with optical carrier at $\lambda_p = 1583nm$ in the waveguide so that the normalized detuning results $2Q(\lambda_p - \lambda_0)/\lambda_0 = 3.75$. According to Eqs. (3.5) and (3.6) the frequency offset is sufficiently large to ensure a bistable effect for input power above the threshold of bistability ($P_i > P^+$). In high power regime the intense energy stored in the cavity causes a local change of the refractive index that decreases proportionally with the increasing of the optical intensity leading to a red shift of the cavity resonance. When the red shifted resonance becomes close to the driving frequency, the signal is switched in the cavity causing a strong enhancement of the internal energy. Further increasing of the intensity leads the resonance to exceed the signal frequency so that the energy in the cavity tends to decrease. The system is then self-balanced by this feedback mechanism. The bistability behav-
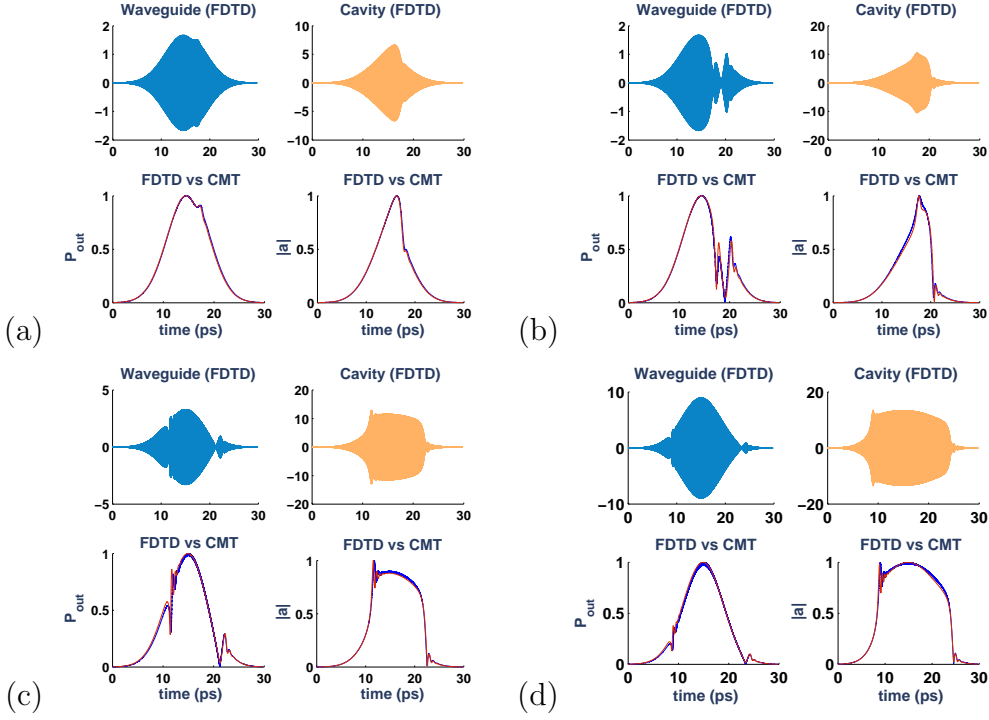
Figure 3.7: From (a) to (d), top left: FDTD power dynamics in the waveguide. Top right: FDTD energy dynamics in the cavity. Bottom left: FDTD power envelope in the waveguide (solid blue curve) compared to the CMT output power dynamics (dashed red curve). Bottom right: FDTD energy envelope in the cavity (solid blue curve) compared to the CMT energy dynamics (dashed red curve). The input powers calculated by means of the CMT simulations are $P_{in} = 0.335 mW/\mu m$ (a), $P_{in} = 0.337 mw/\mu m$ (b), $P_{in} = 1.36$ mW $/\mu m$ (c), $P_{in} = 6.83 mW/\mu m$ (d).

ior is evaluated for different excitation intensities and, as predicted by the CMT model, relaxation oscillations appear in the leading or trailing pulse edge depending on driving excitation intensity. Fig. 3.7 shows the results of FDTD simulations. The signal has been captured in a point of the waveguide and in the cavity; then the envelope has been calculated by means of a low-pass filtering. The nonlinear FDTD dynamics are then compared to the corresponding CMT model in which the parameters are in turn evaluated by linear FDTD simulations.

3.4 All-Optical switching in nonlinear photonic crystals

One of the simplest photonic crystal devices that can be realized by exploiting the nonlinear effects is a switch based on a cavity side-coupled to two waveguides. A waveguide (bus) is dedicated to transport signal data at frequency out of the cavity linewidth, whereas the other waveguide (drop) extracts the signal when the cavity is on resonance. To tune the cavity resonance close to the signal frequency it is necessary to locally change the refractive index of the medium inside the cavity by using the nonlinear properties of the material excited via optical intensity. All-optical switching can be realized in two different ways. In the first one, the switching is obtained by controlling the intensity of the input signal so that, by means of a sort of self-switching, the signal data triggers optical switching by itself. In the second one, the nonlinear effects can be exploited by launching a control beam (pump) to trigger optical switching for the signal (probe) which is maintained at relative low intensity. The switching contrast (SC) in the drop waveguide of the probe intensity evaluated as the ratio between the "'On'" and the "'Off'" states, i.e. $P_{probe}(pump = On)/P_{probe}(pump = Off)$, determines the efficiency of the process. It is easy to understand how, in pump-probe operations, because the optical switching is driven by the external pump light, the major properties of the process, which are the response speed and the switching contrast, can be suitably controlled by the intensity and duration of the pump light.

Two examples of such switching devices are shown in Fig. (3.8) (b) and (c), where the photonic crystal has the same properties (lattice constant, size of square rods, refractive index and third order nonlinear susceptibility) described in the previous section. Here the cavity is made by removing only one rod. The corresponding TM polarized resonant mode is shown in Fig. (3.8) (a) where the pattern of the mode has been calculated by means of numerical DFT. The feasibility of pump-probe operations to switch signal data by exploiting the potentiality of Kerr nonlinearity are investigated in both topologies by performing nonlinear 2D-FDTD simulations.
In the first structure, where the two waveguides has been realized by removing two parallel lines of rods, the probe is injected in the left waveguide
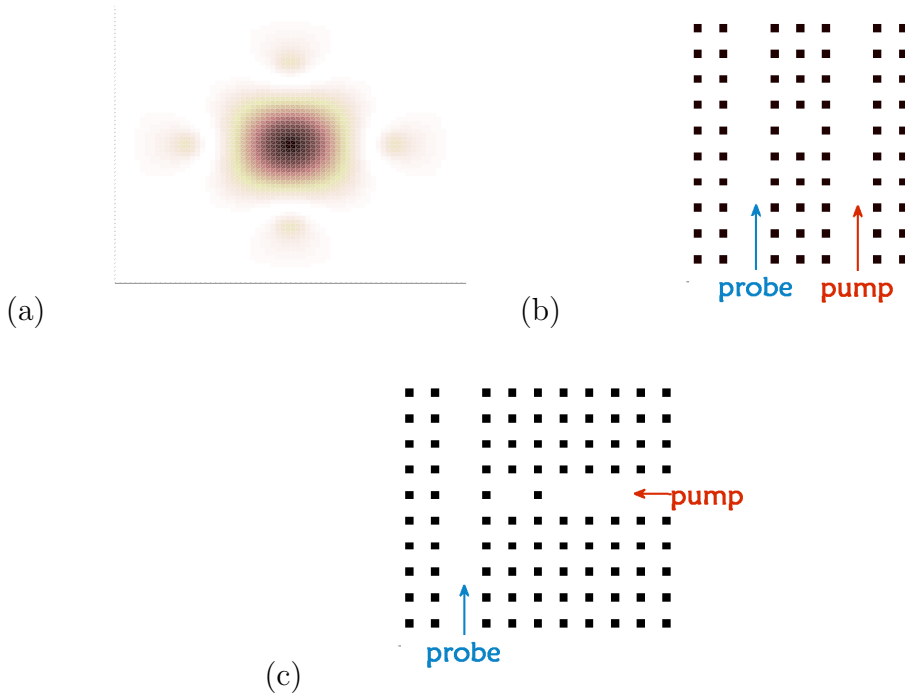
Figure 3.8: Resonant TM polarized mode of a cavity realized by removing one rod in a square photonic crystal of rods in air (a). Example of different switching topologies (b)-(c).

(bus), whereas the pump is launched in the right waveguide (drop). The loaded cavity presents a resonant frequency at $\lambda_0 = 1535nm$ and a quality factor $Q = 86$. The wavelength of the probe is $\lambda_s = 1565nm$, whereas the the pump is at $\lambda_p = 1595nm$, so that the normalized detuning are $\delta_s = 3.36$ and $\delta_p = 6.72$ respectively. Either, probe and pump, are $10ps$ Gaussian pulses. When the optical intensity of the control signal is sufficiently high to lower the cavity resonance close to probe frequency, the signal data is switched from bus to drop. In Fig. (3.9) the results of FDTD simulations are shown. The intensity of the signal is extracted in the bus, in the cavity, as well as in the drop waveguide. When the pump power is increased of the 65% above the bistability critical power, the probe signal is switched from the bus to the drop with a switching contrasr of about SC= 2.

In the second configuration the drop waveguide is terminated next to the cavity and is directed perpendicular with respect to the bus waveguide. The
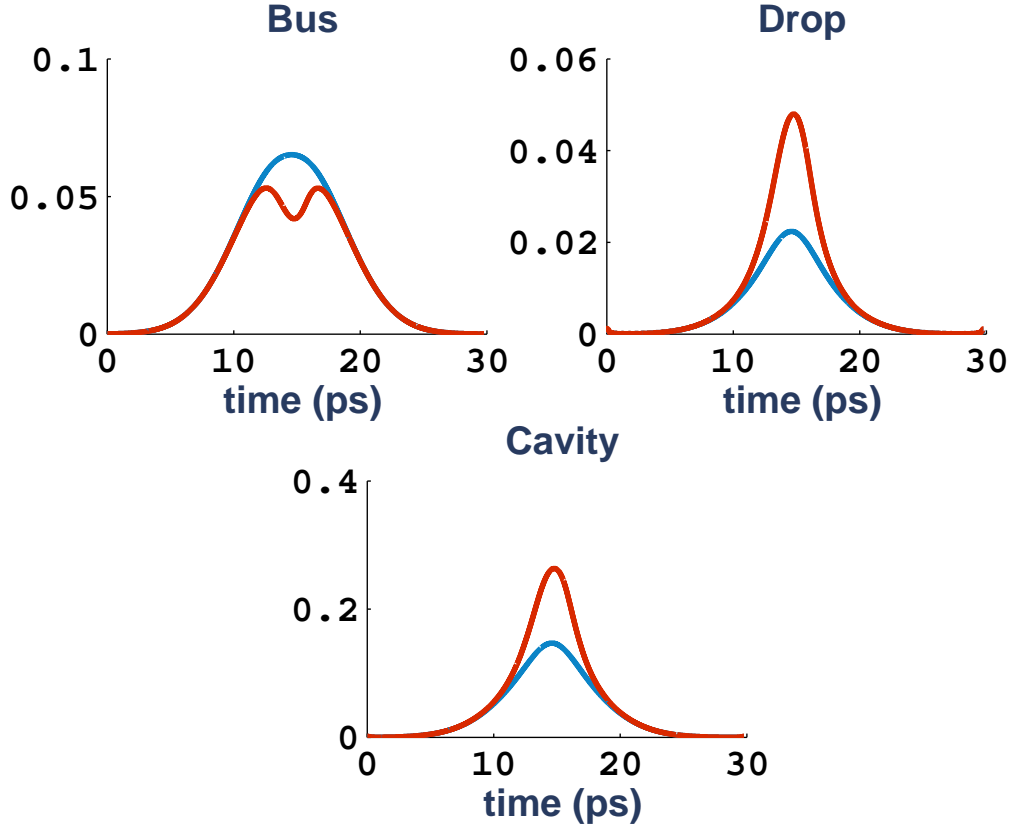
Figure 3.9: Top left: probe intensity in the bus waveguide. Top right: probe intensity in the drop waveguide. Bottom center: energy in the cavity. In each figures the state ʺʻOffʺʼ (blue curve) and the state ʺʻOnʺʼ (red curve) that correspond to low and high input power of the control signal respectively, are shown. The ratio between the ʺʻOnʺʼ and the ʺʻOffʺʼ state in the drop defines the switching contrast.

probe is launched in the bus waveguide, whereas the pump propagates in the drop. The loaded cavity resonates at $\lambda_0 = 1538nm$ with a quality factor $Q = 64$. Pump and probe are two 10 ps Gaussian modulate pulses with optical carrier $\lambda_p = 1619nm$ and $\lambda_s = 1578nm$ respectively, so that the normalized detuning result to be $\delta_p = 6.74$ and $\delta_s = 3.33$. The nonlinear dynamics obtained by 2D-FDTD simulations is shown in Fig. (3.10). For a pump power above the 56% of the critical switching power, the contrast of the probe intensity in the drop waveguide is $SC = 1.5$. It is interesting
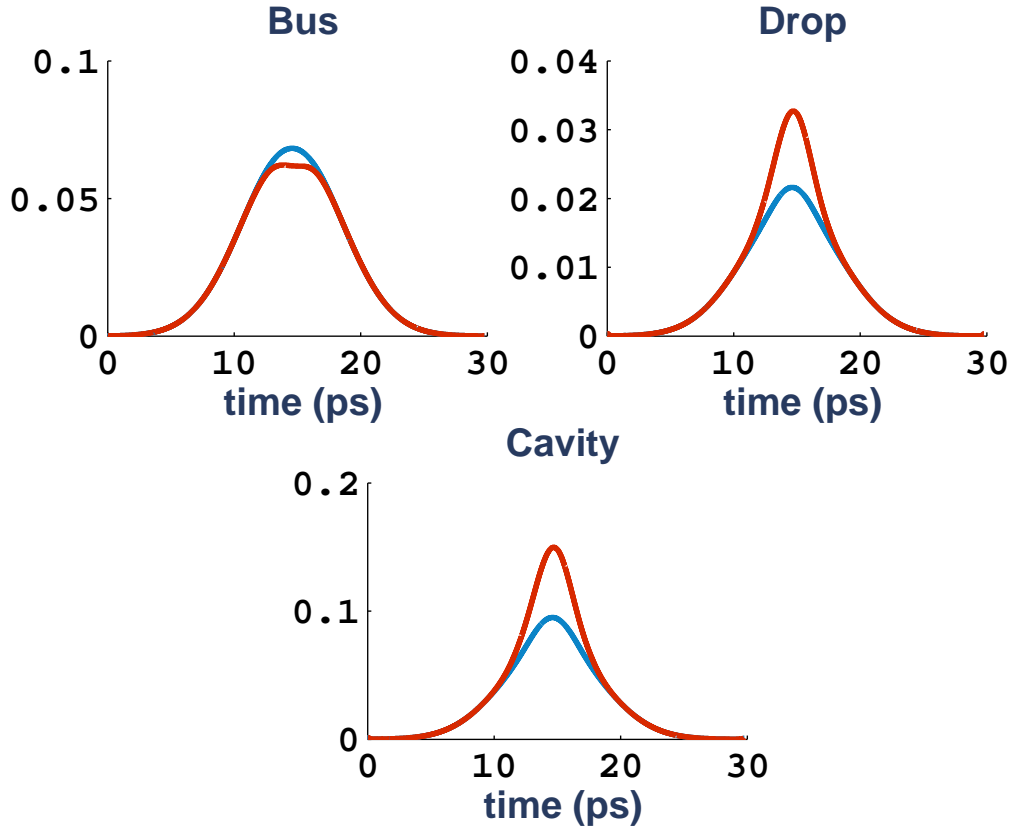
Figure 3.10: Top left: probe intensity in the bus waveguide. Top right: probe intensity in the drop waveguide. Bottom center: energy in the cavity. In each figures the state "'Off"' (blue curve) and state "'On"' (red curve) that correspond to low and high input power of the control signal respectively, are shown. The ratio between the "'On"' and the "'Off"' state in the drop defines the switching contrast.

to emphasize that in this topology the critical power that gives rise to the switching is about the 32% of the power needed in the first configuration. To understand this fact it is useful to resort to a linear CMT description of the two systems.

By defining k_{11} the coupling coefficient between the cavity and the uninterrupted waveguide [25], (note that k_{11} can be expressed in terms of the loaded quality factor as $|k_{11}|^2 = \omega_0/2Q$), for the first configuration the maximum power transferred to drop waveguide can be easily evaluated by means of the

following CMT model:

$$\frac{\partial a}{\partial t} = i\omega_0 a - 2|k_{11}|^2 a + k_{11}s \tag{3.12}$$

In fact, in the first configuration where the structure is completely symmetric, the linear losses (accounted for the terms $2|k_{11}|^2$ in Eq. (3.12)) are the same in the bus and drop waveguides (explaining the factor 2). The transmission at the drop port is given by $t_d = k_{11}^* a/s$ and results to be

$$t_d = \frac{|k_{11}|^2}{i(\omega - \omega_0) + 2|k_{11}|^2} \tag{3.13}$$

Therefore, on resonance the maximum drop efficiency is

$$T_d = |t_d(\omega_0)|^2 = \frac{1}{4} \tag{3.14}$$

irrespective of the value of k_{11}. Conversely, for the second configuration, by defining k_{12} the coupling coefficient between the cavity and the interrupted waveguide, the CMT model is written as

$$\frac{\partial a}{\partial t} = i\omega_0 a - |k_{11}|^2 a - \frac{|k_{12}|^2}{2}a + k_{11}s \tag{3.15}$$

and the transmission in the drop waveguide is

$$t_d = \frac{k_{12}^* k_{11}}{i(\omega - \omega_0) + |k_{11}|^2 + \frac{|k_{12}|^2}{2}} \tag{3.16}$$

This latter relation gives the following transmission efficiency when evaluated at resonant frequency

$$T_d = |t_d(\omega_0)|^2 = \frac{k_{12}^2 k_{11}}{|k_{11}|^2 + \frac{|k_{12}|^2}{2}} \tag{3.17}$$

that results to be maximum when $|k_{12}| = \sqrt{2}|k_{11}|$ leading to a 50% of power transferred from bus to drop. Finally, in order to evaluate the effective drop efficiency, the coupling strength between the cavity and the two different (uninterrupted and interrupted) waveguides should be determined. This can be easily obtained by comparing the values of the quality factor of the two configurations. For the first topology $Q_1 = 86$ that yields a total loss $\alpha_1 \equiv$
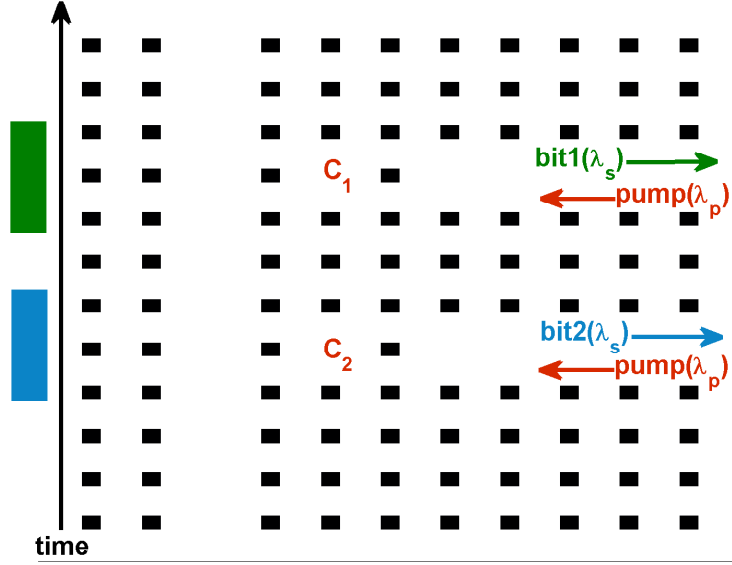
Figure 3.11: Photonic crystal structure for the serial to parallel converter.

$\omega_{01}/2Q_1$. Equivalently, in the second structure $Q_2 = 64$ that results in a total loss $\alpha_2 \equiv \omega_{02}/2Q_2$. The ratio α_2/α_1 is approximatively equal to $4/3$ that gives a value of $|k_{12}| = \sqrt{10/3}|k_{11}|$ with a drop efficiency for the second topology of about 47%, i.e. very close to the ideal optimum value. This analytical formalism explains the major switching efficiency of the second structure with respect to the first one.

3.5 The serial to parallel converter

A more complex device that can be realized by using the switching pump-probe method described in the previous sections is the all-optical serial to parallel converter that processes a data stream composed by a sequence of bits. The bits are at the same optical carrier so, the discrimination of the informations is ensured by reserving a different time slot for each bit. This is known as an optical time division multiplexer (OTDM) system. The function of the serial to parallel converter is the simultaneous switching of the N serial

44

bits from a common channel (bus) to N different channels (drop). Thereby, the parallelism of the informations is obtained by spatial division of the bits stream that travel synchronously in the output channels. To realize the serial to parallel converter, a structure in square photonic crystal of rods in air has been designed. The same features of previous models, i.e. a lattice constant of $600nm$, a width of $150nm$ for the square rods, a refractive linear index of 4.3, and a third-order susceptibility of $0.08m^2/V^2$ for the Kerr effect, have been considered. The structure is shown in Fig. (3.11) and consists of a bus waveguide that carries the serial data stream, two drop waveguides for the parallel conversion, and two single-defect cavities to extract the signal by injecting the pump control signals. The loaded Q-factor of the cavities is $Q = 64$ and the resonant wavelength is $\lambda_0 = 1538nm$. The bits are two $10ps$ Gaussian pulses at $\lambda_s = 1578nm$ that corresponds to a detuning of $\delta_s = 3.33$. The pump signals are also 10 ps Gaussian pulses but with carrier wavelength $\lambda_p = 1619nm$ giving a normalized detuning of $\delta_p = 6.74$. Thereby, the bistability effect induced by Kerr nonlinearity can be triggered for the data stream as well as for the pump signals. To obtain a correct synchronism, the two control signals are properly timed so that the first bit is switched in the high drop waveguide and the second bit in the low drop waveguide. Fig. (3.12) shows the nonlinear 2D-FDTD temporal dynamics of the data stream outgoing from the drop waveguides for two different values of the control power. When the power pumped into the system is below the bistabilty threshold no appreciable switching contrast is detected in the output channels (yellow curves in Fig. (3.12)), so that the two bits have the same intensity in each channels and cannot been discriminated. This is what happens for a pump power of about $2.7mW/\mu m$, that is not able to excite the cavities. Instead, when the drivers are brought above bistability threshold, each of them carrying a power of about $4.2mW/\mu m$, the bits are switched into the corresponding output waveguides. In fact, as shown in bottom of Fig. (3.12) the first bit is detected in the lower drop waveguide (green curve), whereas as shown in top of Fig. (3.12) the second bit is detected in the higher drop waveguide (blue curve).
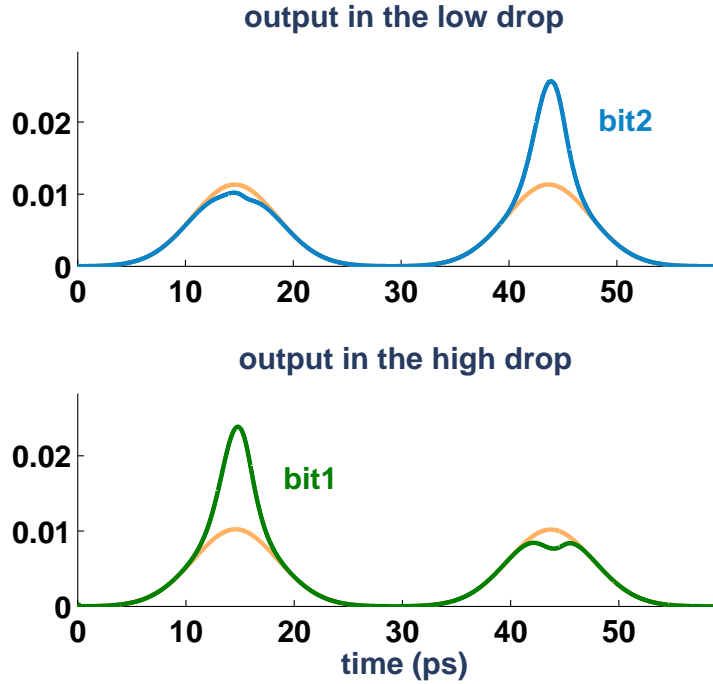
Figure 3.12: Temporal dynamics of signal data processed by the serial to parallel converter. Bottom: stream bit outgoing from the high drop waveguide for a pump power below (yellow curve) and above (green curve) threshold, that yields the detection of the first bit. Top: stream bit outgoing from the low drop waveguide for a pump power below (yellow curve) and above (blue curve) threshold, that yields the detection of the second bit.

3.6 Summary

In this chapter the Kerr effect has been studied in detail. The aim has been to investigate the properties of high-Q cavities in photonic crystal based devices realized in Kerr material and to exploit the bistable effect in order to realize all-optical devices. In particular, the design method has provided the realization of a nonlinear FDTD code that incorporates the governing equations for Kerr nonlinearity. The obtained results have been compared with those predicted by a theoretical CMT model, showing a good agreement. Finally, switches and more sophisticated devices such as optical converters have been demonstrated to work in nonlinear Kerr regime.

Chapter 4

Modeling and design of PhC based devices operating in the two photon absorption limit

4.1   Introduction

The aim of this last chapter is to set up a code able to model the main nonlinear effects in semiconductor materials to be used as a tool for the design of new optimized optical devices exploiting these effects. To this end, an analysis of the relevant nonlinear effects such as two photon absorption (TPA), free carriers dispersion (FCD), free carriers absorption (FCA), and carriers diffusion, is performed. The governing nonlinear equations are incorporated in a 2D-FDTD code that accounts for all of these nonlinear effects. The realized FDTD tool is tested by means of a theoretical CMT model and further by comparing the numerical outcomes with experimental results. The good agreement of the FDTD results with both theory and experiments allows the use of the nonlinear code to design new optical topologies for all-optical signal processing. In particular, in the last section of this chapter, two optimized configurations for a three-ports All Optical Gate (AOG) that show better performances than those known in literature are developed.

4.2 Theoretical and numerical methods

In this section, the theoretical Coupled Mode Theory (CMT) method and the numerical Finite Difference Time Domain (FDTD) scheme are developed with the purpose to investigate the nonlinear dynamics emerging in the two photon absorption regime. As demonstrated, the two methods are very efficient tools for the analysis of the nonlinear response in optical structures, each of them providing different advantages with respect their use and different insights into the nonlinear behavior.

4.2.1 The nonlinear CMT model

Dispersion induced by free carriers causes a reduction of the refractive index and, similarly to the Kerr effect, it is also capable to give rise to a bistable response for feedback mechanism. To understand this effect, it is useful to model the nonlinear dynamics that occurs inside a single mode cavity resonants at frequency ω_0 and pumped via a waveguide by a pulse at laser frequency ω_L. In such a structure, the set of coupled equations that govern the nonlinear behavior for the internal cavity energy are the following [8]:

$$\frac{\partial a}{\partial t} = i(\omega_0 + \Delta\omega_{NL} - \omega_L)a - \frac{\Gamma_{tot}}{2}a + \sqrt{\frac{\Gamma_c}{2}P_{in}} \qquad (4.1)$$

where Γ_{tot} is the inverse cavity lifetime and $\Gamma_c = \omega_0 \left(1/Q - 1/Q_0\right)$ is the cavity to waveguide coupling coefficient that depends on the intrinsic quality factor Q_0 and on the loaded quality factor Q. $\Delta\omega_{NL}$ is the nonlinear change of the frequency and it is given by

$$\Delta\omega_{NL} = -\frac{\omega_0}{n_0}\Delta n = -\frac{\omega_0}{n_0}\left(\frac{n_{2I}c}{n_0 V_{Kerr}}|a|^2 + \frac{dn}{dN}N(t)\right) \qquad (4.2)$$

with c the light speed in the vacuum, n_0 the linear refractive index of the bulk material, n_{2I} the Kerr coefficient and V_{Kerr} the Kerr nonlinear volume [35], [36]. N is the free carriers density that induces the change in the refractive index according to the following equation

$$\frac{dn}{dN} = -\frac{\omega_p^2}{2n_0\omega_0^2 N} \qquad (4.3)$$

where $\omega_p^2 = e^2 N / \epsilon_0 m^*$ is the plasma frequency, with e the electron charge and m^* the effective electron mass. In tush model the total losses are $\Gamma_{tot} = \omega_0/Q + \Gamma_{TPA} + \Gamma_{FCA}$, with ω_0/Q representing the inverse linear cavity lifetime. Γ_{TPA} is the nonlinear coefficient that accounts for the losses due to two-photon absorption and it is given by

$$\Gamma_{TPA} = \frac{\beta_2 c^2}{n_0^2 V_{TPA}} |a|^2 \tag{4.4}$$

being β_2 the TPA coefficient and $V_{TPA} = V_{Kerr}$ the nonlinear TPA volume. The nonlinear losses due to free carriers absorption are taken into account by the Γ_{FCA} coefficient proportional to the carriers density as follows

$$\Gamma_{FCA} = c(\sigma_c + \sigma_h) \frac{N(t)}{n_0} \tag{4.5}$$

where σ_c and σ_h are the cross sections for free-electron absorption and for free-hole absorption, respectively. The rate equation which governs the evolution of the carriers density is the following

$$\frac{\partial N}{\partial t} = \frac{c^2 \beta_2}{2\hbar \omega_0 n_0^2 V_{TPA} V_{car}} |a|^4 - \frac{N(t)}{\tau_r} \tag{4.6}$$

with τ_r the effective carriers lifetime and V_{car} the relevant volume in which the carriers spread and recombine [35].

4.2.2   2D-FDTD modeling

As analyzed in the chapter 1, the equations that govern the Kerr and the two photon absorption dynamics in two-dimensional structures can be easily written for TE polarized light. This allows to model the nonlinear dynamics by means of a FDTD code that fully accounts for the nonlinear response of the material. By following the method used in [12] for the 1D-FDTD implementation, the set of the equations that models the nonlinear dynamics can be extended to two dimensional domain for TE polarized light. The starting point are the Maxwell's equations:

$$\nabla \times \mathbf{E} = -\mu_0 \frac{\partial \mathbf{H}}{\partial t}$$
$$\nabla \times \mathbf{H} = \frac{\partial \mathbf{D}}{\partial t} \tag{4.7}$$

where the electric field has two in-plane polarized components, whereas the magnetic field has only one component polarized in the perpendicular direction with respect to the PhC plane. The electric displacement $\mathbf{D}$ is given by the constitutive equation

$$\mathbf{D} = \epsilon_0 \mathbf{E} + \mathbf{P} \tag{4.8}$$

with $\mathbf{P}$ that accounts for the third-order nonlinear polarizations:

$$\mathbf{P} = \mathbf{P}_{Kerr} + \mathbf{P}_{TPA} + \mathbf{P}_{FCA} + \mathbf{P}_{plasma} \tag{4.9}$$

where $\mathbf{P}_{Kerr} = \epsilon_0 \chi_{Kerr} \mathbf{E}$ is the Kerr polarization with Kerr susceptibility given by

$$\chi_{Kerr} = c n_0^2 n_{2I} |\mathbf{E}|^2 \tag{4.10}$$

with c the light speed in the vacuum, n_0 the linear refraction index, and n_{2I} the Kerr nonlinear coefficient. $\mathbf{P}_{TPA} = \epsilon_0 \chi_{TPA} \mathbf{E}$ is the polarization that accounts for the losses induced by two photon absorption. The susceptibility χ_{TPA} is modeled by the following partial differential equation

$$\frac{\partial \chi_{TPA}}{\partial t} = c^2 \epsilon_0 n_0^2 \beta |\mathbf{E}|^2 \tag{4.11}$$

in which the term β is the TPA nonlinear coefficient. The free carriers absorption polarization $\mathbf{P}_{FCA}$ that describes the losses induced by TPA generated carriers, is expressed as a partial differential equation in the form

$$\frac{\partial \mathbf{P}_{FCA}}{\partial t} = c \epsilon_0 n_0 \sigma_{FCA} N \mathbf{E} \tag{4.12}$$

where σ_{FCA} is the cross section for free-electrons and free-holes absorption, and N is the free carriers density. Free carriers, in turn, cause a refractive index change $\Delta n_{plasma}(N)$ related to the plasma polarization as follows

$$\mathbf{P}_{plasma} = 2\epsilon_0 n_0 \Delta n_{plasma} \mathbf{E} \tag{4.13}$$

in which the nonlinear index change depends on the free carriers density according to the equation

$$\Delta n_{plasma} = -\frac{e^2 N}{2\epsilon_0 m^* n_0} \tag{4.14}$$

The free carriers density dynamics can be modeled by means of the following rate equation

$$\frac{\partial N}{\partial t} = \frac{c^2 \epsilon_0^2 n_0^2 \beta}{8 \hbar \omega_0} |\mathbf{E}|^4 - \frac{N}{\tau_r} + D \nabla^2 N \qquad (4.15)$$

Nevertheless the CMT equations, here the carriers transport is governed not only by optical intensity and carriers recombination but also by the diffusion effect that, as described in the section 4.5, in nonlinear regime heavily affects the carriers lifetime inside the nanostructures, and then can not throughly ignored. Therefore, the diffusion effect has been incorporated into the FDTD code by means of the last terms of the Eq. (4.15).

All of these equations are incorporated in a 2D-FDTD code by means of time domain discretization (a detailed description of the discretized nonlinear equations is reported in appendix B). The FDTD code is tested in the following sections by means CMT models and experimental data.

4.3 Self-pulsing induced in two photon absorption regime

The bistabilty effect induced by free carriers dispersion can be analyzed by means of the set of Eqs. (4.1)-(4.6) that describe a structure where an optical cavity is coupled to a waveguide in a nonlinear medium. The effects that are considered are TPA induced pump depletion, absorption by TPA generated free carriers, and free carriers dispersion. In order to derive the relevant conditions that carry out the nonlinear frequency tuning of the cavity, the coupled mode governing equations are written as follows

$$\begin{aligned} \frac{\partial a}{\partial t} &= i(\delta + N)a - a - \alpha |a|^2 a - \gamma N a + \sqrt{P} \\ \frac{\partial N}{\partial t} &= |a|^4 - \frac{N}{\tau} \end{aligned} \qquad (4.16)$$

where a, N, and P are time-dependent variables opportunely normalized that represent the cavity energy, the carriers density induced by TPA, and the incoming optical intensity, respectively, and where t is a dimensionless temporal variable. Here, the two dimensionless coefficients δ and τ has been

defined as

$$\delta = \frac{\omega_0 - \omega}{\Gamma_0} \qquad \tau = \Gamma_0 \tau_r = \frac{\tau_r}{\tau_0} \tag{4.17}$$

where $\Gamma_0 = \omega_0/2Q = 1/\tau_0$ is the cavity lifetime, whit ω_0 the cavity resonance and Q the quality factor, whereas τ_r is the effective carrier lifetime. The system (4.16) is deduced starting from the conventional coupled equations outlined in [8] by normalizing the u (cavity energy), N_f (carriers density) and P_{in} (input intensity) variables as follows

$$a = u\sqrt[4]{\sigma\beta} \qquad N = \frac{\sigma N_f}{\Gamma_0} \qquad P = \frac{\sqrt{\sigma\beta} P_{in}}{\Gamma_0} \tag{4.18}$$

The dimensionless coefficients α and γ, and the coefficients σ in units of m^3 and β in units of J^{-2} m^{-3}, are given by

$$\begin{aligned} \sigma &= \frac{e^2}{\Gamma_0 2\epsilon_0 n_0^2 \omega_0 m^*} \qquad \beta = \frac{c^2 \beta_2}{\Gamma_0 2\hbar\omega_0 n_0^2 V_{TPA} V_{car}} \\ \alpha &= \frac{c\omega_0}{e}\sqrt{\hbar\epsilon_0\beta_2 m^*}\sqrt{\frac{V_{car}}{V_{TPA}}} \qquad \gamma = \frac{c(\sigma_e + \sigma_h)\epsilon_0 n_0 m^* \omega_0}{e^2} \end{aligned} \tag{4.19}$$

where c is the light speed in the vacuum, n_0 the linear refractive index, $\hbar$ the Planck constant, e the electron charge, m^* the electron effective mass, β_2 the TPA coefficient, σ_e and σ_h the cross sections for free-electron absorption and free-hole absorption, respectively, V_{TPA} the nonlinear TPA volume, and V_{car} the volume in which the charges spread and recombine.

4.3.1 Analytical study of bistability in low lossy regime

In order to investigate analytically the nonlinear response, as first approximation, the system (4.16) is studied by neglecting the nonlinear losses. When the lossy coefficients α and γ are set to zero the system (4.16) becomes

$$\begin{aligned} \frac{\partial a}{\partial t} &= i(\delta + N)a - a + \sqrt{P} \\ \frac{\partial N}{\partial t} &= |a|^4 - \frac{N}{\tau} \end{aligned} \tag{4.20}$$

The stationary solution of Eqs. (4.20) yields to a bistable response described by the relation

$$\bar{P} = E\left[1 + (\delta + \tau E^2)^2\right] \tag{4.21}$$
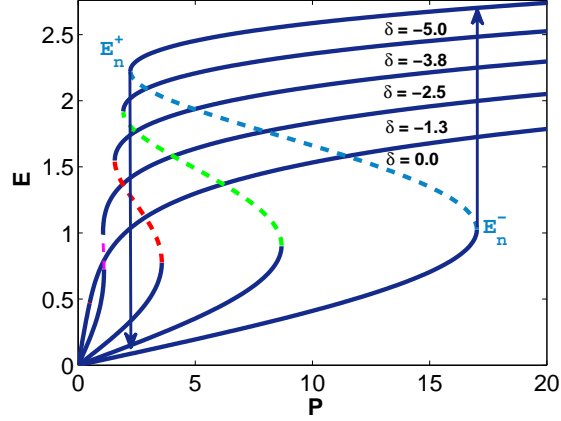
Figure 4.1: Bistable behavior ruled by the Eq. (4.20) when $\delta = -3$.

written with respect to the time-independent cavity energy $E = |A|^2$, incident optical intensity $\bar{P}$ and carriers density $\bar{N}$. From Eq. (4.21) it is possible to find that the normalized detuning needed to give rise to bistability must satisfy the condition $\delta < -\sqrt{5}/2$. Fig. 4.1 shows the relationship $E = f(P)$ according to Eq. (4.21) for different detuning δ. For $\delta < -\sqrt{5}/2$ the response is a threefold function of P exhibiting knee values at internal cavity energy

$$En^\pm = \sqrt{\frac{-3\delta \pm \sqrt{4\delta^2 - 5}}{5\tau}} \tag{4.22}$$

As pointed out in [37], it is expected that the nonlinearity ruled by the rate equation in the system (4.20), gives rise to instability owing to the presence of a characteristic recovery time (accounted for the therm τ) that is comparable to that in which the system evolves. In order to verify this, it is useful to resort to the linearized system by rewriting the cavity energy and the carriers density in (4.20) as their steady-state values with a linear perturbation in the form $a(t) = A + \epsilon(t)$ and $N(t) = \bar{N} + \delta n$. These simple ansatz yield

$$\begin{aligned}
\dot{\epsilon} &= \left[i(\delta + \tau|A|^4) - 1 \right] \epsilon + iA\delta n \\
\dot{\epsilon^*} &= \left[-i(\delta + \tau|A|^4) - 1 \right] \epsilon^* - iA^*\delta n \\
\dot{\delta n} &= 2|A|^2(\epsilon A^* + \epsilon^* A) - \frac{\delta n}{\tau}
\end{aligned} \tag{4.23}$$

The linearized system has two complex conjugate eigenvalues and a purely
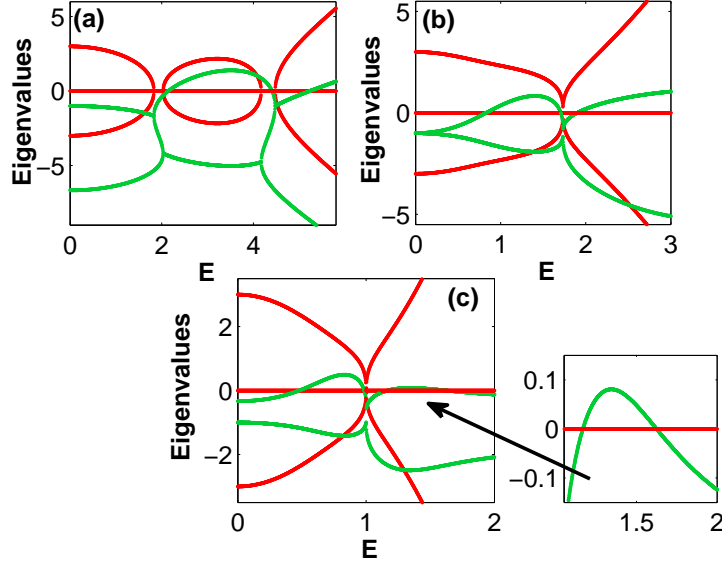
Figure 4.2: Real (green lines) and imaginary (red lines) part of the eigenvalues of the system for $\delta = -3$ and $\tau = 0.15$(a), $\tau = 1$ (b), and $\tau = 3$ (c).

real one. In Fig. 4.2 are shown the real (green lines) and imaginary (red lines) part of the eigenvalues when $\delta = -3$ for different values of τ. When the eigenvalues have negative real part the dynamics shows stable damped oscillations that occur with normalized frequency $\Omega = |Im(\lambda)|$, whereas the presence of a eigenvalue with a positive real part gives rise to instability. The latter occurs always in the negative slope branch of the bistable response and causes the jump from low (high) energy to high (low) energy states. A more detailed analysis reveals that in the upper branch the system can experience Anrdonov-Hopf bifurcation yielding an unstable solution. The bifurcation results to be supercritical emerging in a limit cycle oscillating with period $2\pi/\Omega$. The Hopf bifurcation happens for energy values that satisfy the following relation

$$E_b^{\pm} = \sqrt{\frac{\delta(\tau - 1) \pm \sqrt{\delta^2(\tau - 1)^2 + (2\tau - \tau^2)\left(\delta^2 + \left(1 + \frac{1}{\tau}\right)^2\right)}}{2\tau - \tau^2}} \qquad (4.24)$$
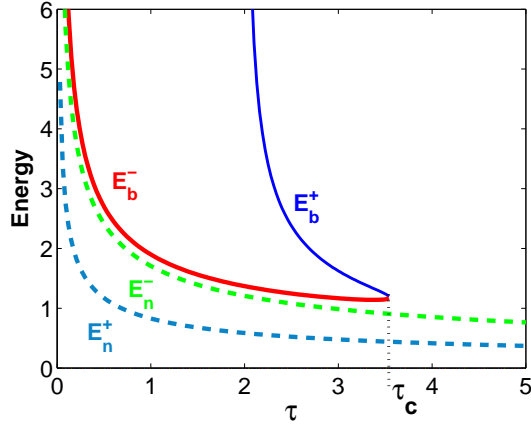
Figure 4.3: $E_b^\pm$, and $E_n^\pm$ values as a function of τ for $\delta = -3$.

From this latter, it follows that the Hopf bifurcation exists only for values of the detuning δ that satisfy

$$\delta^2 \geq \tau^2 - 2/\tau - 3. \tag{4.25}$$

Furthermore, when $\tau \geq 2$ the Eq. (4.24) admits the two solutions with different sign. This means that the system can start from a stable regime, undergoes bifurcation and finally returns to a stable regime. Fig. 4.3 shows the values $E_b^\pm$ as a function of τ. The point of bifurcation denoted by E_b^- exists for $\tau > 0$ (red curve). As expected, E_b^- moves toward increasingly higher energy values when τ approaches to zero becoming undefined for $\tau = 0$. This is consistent with the fact that the characteristic time of the nonlinearity becomes negligible with respect to the cavity lifetime, and the system experiences the dynamics typical of the systems subjected to instantaneous nonlinearities. The E_b^+ solutions (blue curve) appears for $\tau \geq 2$, and leads to an instability behavior that does not fall into chaotic regime. When the relation in Eq. (3.7) is satisfied for a given critical value τ_c, the two energy point $E_b^\pm$ disappear because of the presence of their imaginary part. Moreover, as shown in Fig. 4.3, the bifurcation point always lies above the point E_n^- (green curve) corresponding to the jump in the bistable response. This means that the unstable response always occurs.

As it can be seen, the energy pulse experiences stable periodic oscillations
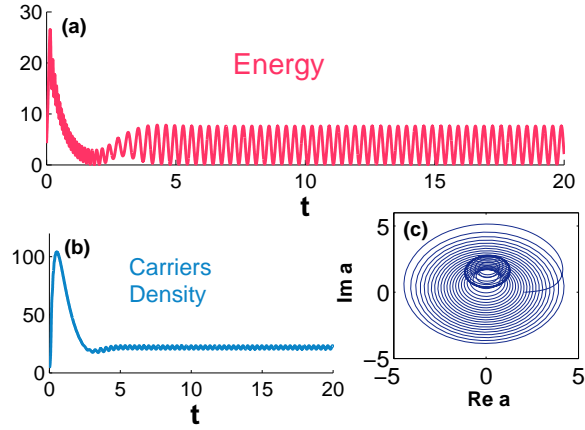
Figure 4.4: Self-pulsing dynamics of the intra-cavity energy (a) and carriers density (b) when $\delta = -3$ and $\tau = 1$. Limit cycle emerging from the bifurcation point corresponding to periodic stable regime (c).

resulting in a limit cycle (see Fig. 4.4 (c)) as it falls into a state of the upper bistable branch. Interestingly, it is found that the existence of the bifurcation does not require the bistable regime. Fig. 4.5 shows, for $\delta = 4$ and $\tau = 1$, self-pulsing behavior of the cavity energy (a), eigenvalues of the system (b), and limit cycle (c).
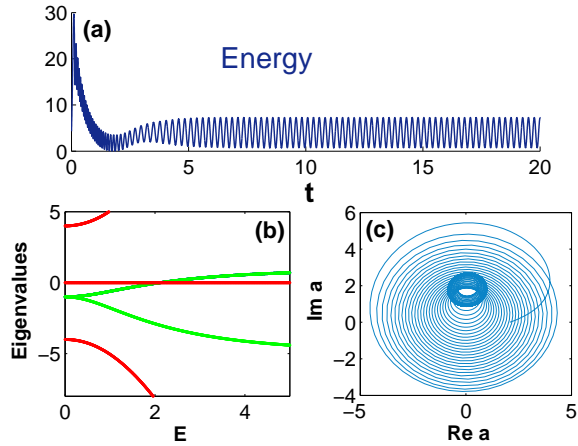
Figure 4.5: Self-pulsing behavior in the absence of bistable response: $\delta = 4$ and $\tau = 1$. Cavity energy evolution (a), system of eigenvalues (b), and limit cycle (c).

Finally, it is investigated how the critical switching power depends on the quality factor Q and modal volume V of the cavity. By simple manipulations of the Eqs. (4.21)-(4.22), the power threshold that triggers the jump from the lower to the upper bistable branch results to be $P^c \propto \sqrt{|\delta|/\tau}$. From the definition of the coefficients in Eq. (4.22), the minimum required switching power in dimensionless units (evaluated for $\delta = -\sqrt{5}/2$) results to be $P^c \propto \sqrt{\tau}$, consequently the dimensional power turns out to be $P_{in}^c \propto V/Q\sqrt{Q}$. This demonstrates that a system in delayed nonlinear regime, provides lower efficiency than systems affected by instantaneous nonlinearities.

4.3.2   Bistability in regime of TPA and FCA losses

In this section, it is investigated how TPA and FCA losses affect the results previously outlined. Before proceeding, it is useful to recall that in TPA regime, two photons are absorbed to generate a free carrier, and then it is not correct to thoroughly ignore the lossy coefficient α in Eq. (4.16). However, as defined in Eq. (4.22), α depends on ratio between the carrier volume and the TPA volume. The carrier volume in turn, is related to the carriers length diffusion and size of the cavity, therefore it can be opportunely reduced by material and geometry engineering. Analogous considerations hold for the losses induced by free carriers absorption. In particular, it is expected that in high-Q small volume cavities, the nonlinear losses can drastically be reduced. Therefore, the previous approximate analysis becomes an useful study to fully understand the dynamics in what follows.

The stationary regime of Eq. (4.16) in which are present TPA and FCA losses is given by

$$P = E \left[(1 + \alpha E + \gamma \tau E^2)^2 + (\delta + \tau E^2)^2 \right] \tag{4.26}$$

Fig. (4.6) compares the bistable response without losses (black dashed line) seen in the previous section with the bistable behavior when TPA (red line) and FCA (blue line) losses are introduced. To take into account realistic parameters, here it is used $V_{TPA} = 1.7 \, (\lambda_0/n_0)^3$, $V_{car} = 0.6 \, (\lambda_0/n_0)^3$ (where
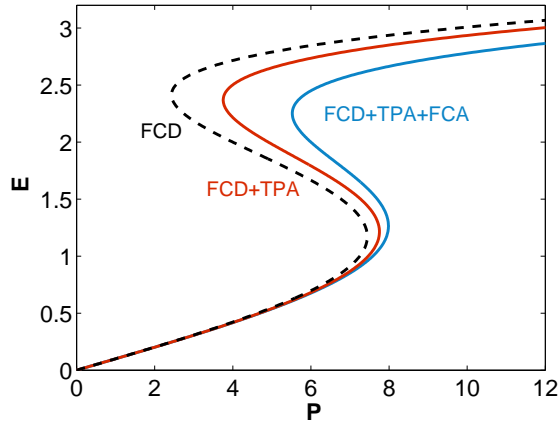
Figure 4.6: Comparison between bistable responses for the three different regimes: lossless system (dark dashed line), system affected by TPA induced losses (red line), and system affected by TPA and FCA losses (blue line). Here $\delta = -3$, $\tau = 0.5$, $\alpha = 0.1$ and $\gamma = 0.1$

$\lambda_0 = 2\pi c/\omega_0$ is the resonant wavelength of the cavity), $\sigma_e = 6 \times 10^{-22}$ m^2, and $\sigma_h = 9 \times 10^{-22}$ m^2. These values yield $\alpha = 0.1$ and $\gamma = 0.1$. Obviously, as shown in Fig. 4.6, losses affect the bistable response by lowering the efficiency in the frequency tuning of the cavity. It is worth noting that, unlike the lossless system, in this case it is not possible to obtain a condition that triggers the bistable response depending on the detuning δ value alone. This can be seen in Fig. 4.7 where the maps of P (in logarithmic units) as a function of τ and E (in logarithmic units) for fixed $\delta = -3$, are compared for the two regimes: with nonlinear losses (a) and without nonlinear losses (b). It is found that, despite the lossless case in which for $\delta < -\sqrt{5}/2$ and irrespective of τ P is a threefold function of E, in presence of losses, for small values of τ the bistability does not occur. This consideration is further highlighted in Fig. 4.8, where the P values are reported as a function of δ and E by fixing $\tau = 0.1$. As it can be seen from Fig. 4.8, when nonlinear losses are neglected, the bistable behavior takes place for $\delta < -\sqrt{5}/2$ (Fig. 4.8(b)), whereas in presence of nonlinear losses the detuning needed to trigger bistability must be decreased until $\delta = -2.27$ (Fig. 4.8(b)).
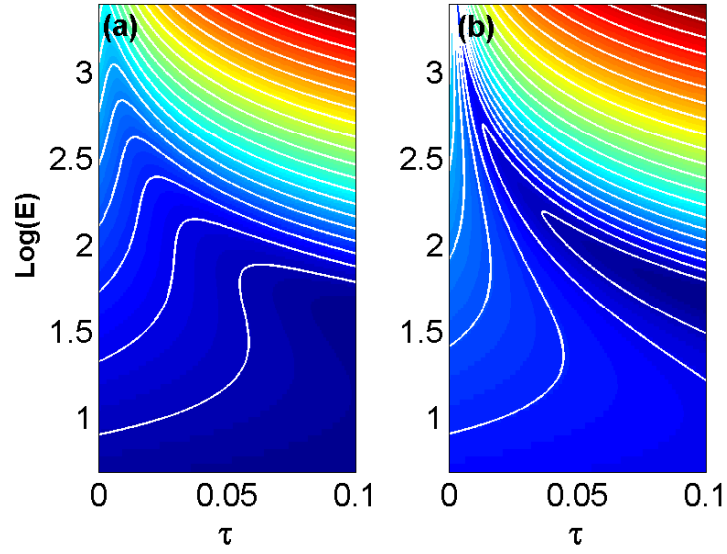
Figure 4.7: Map of input power in logarithmic units ($log(P)$) as a function of τ and $log(E)$ for $\delta = -3$ for the lossy regime (a) and lossless regime (b).
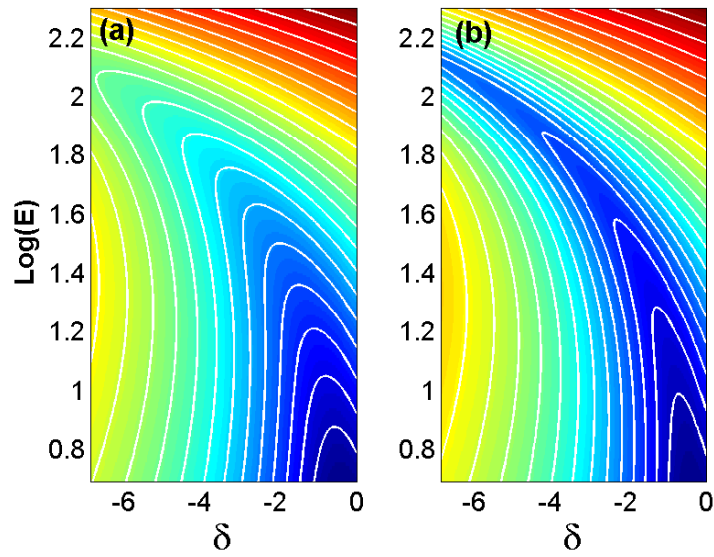
Figure 4.8: Map of input power in logarithmic units ($log(P)$) as a function of δ and $log(E)$ for $\tau = 0.1$ for the loss regime (a) and lossless regime (b).
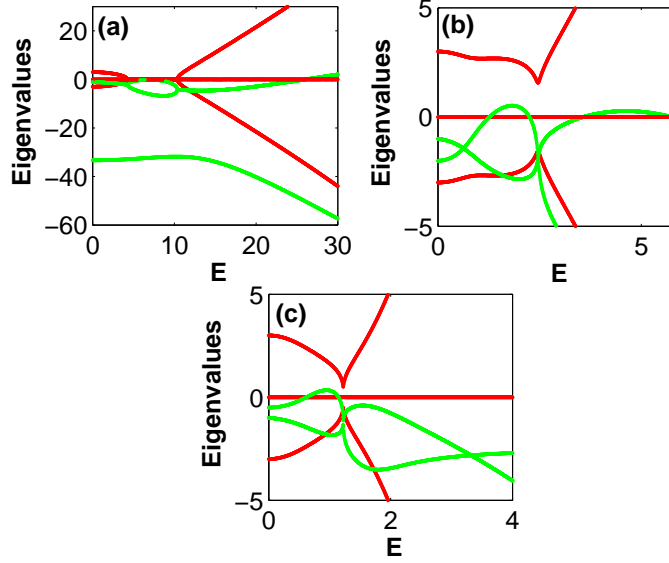
Figure 4.9: Real (green lines) and imaginary (red lines) part of the eigenvalues of the system for $\delta = -3$ and $\tau = 0.03$(a), $\tau = 0.5$ (b), and $\tau = 2$ (c).

The stability of the system (4.16) is investigate by considering the following set of linearized equations:

$$\dot{\epsilon} = \left[i(\delta + \tau E^2) - 1 - 2\alpha E - \gamma\tau E^2\right]\epsilon - \alpha A^2\epsilon^* - (\gamma - i)A\delta n$$
$$\dot{\epsilon^*} = \left[-i(\delta + \tau E^2) - 1 - 2\alpha E - \gamma\tau E^2\right]\epsilon - \alpha A^{*2}\epsilon - (\gamma + i)A^*\delta n \qquad (4.27)$$
$$\dot{\delta n} = 2|A|^2(\epsilon A^* + \epsilon^* A) - \frac{\delta n}{\tau}$$

The eigenvalues of the system (4.27) are shown in Fig. 4.9 when $\delta = -3$ for $\tau = 0.03$ (a), $\tau = 0.5$ (b), and $\tau = 2$ (c). Depending on δ, for sufficiently small values of τ, it is still found the bifurcation point (see Fig. 4.9 (a) and (b)). Moreover, by solving numerically the eigenvalue problem, it is observed that always exists a second point in which the real part of the eigenvalue that gives rise to Hopf bifurcation becomes zero. This means that the unstable dynamics never undergoes a chaotic regime. In order to understand the dependence of the bifurcation on the normalized time τ, in Fig. 4.10 are shown the two energy values E_b^- (red curve) and E_b^+ (blue curve) accounting for the bifurcation point and the further transition through zero of the eigenvalue, respectively. The points E_b^- and E_b^+ become undefined as τ approaches to

60
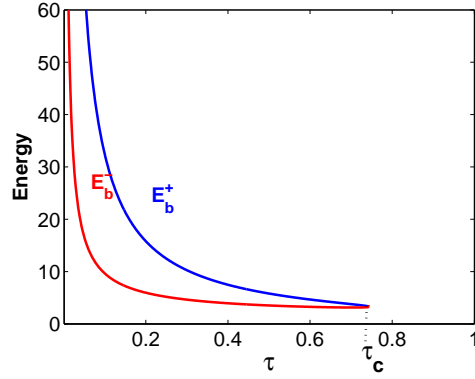
Figure 4.10: $E_b^{\pm}$ values as a function of τ for $\delta = -3$.
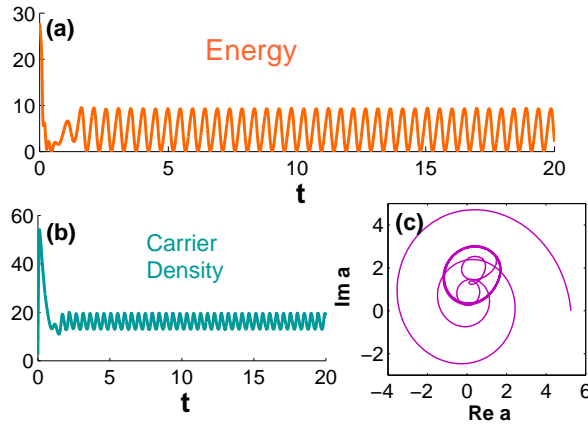
Figure 4.11: Self-pulsing dynamics of the lossy system when $\delta = -3$ and $\tau = 0.5$. Intra-cavity energy (a), Carriers density (b), and limit cycle (c).

zero. Additionally, as in the lossless regime, a critical value τ_c is found, so that when $\tau \geq \tau_c$ the two points collapse and then vanish.

Finally, the self-pulsing dynamics by perturbing the system that evolves from an unstable initial condition beyond the bifurcation point is investigated. Results are shown in Fig. 4.11, where periodic oscillations of the intra-cavity energy (a) as well as of the carriers density (b), and the occurrence of the limit cycle (c) confirm the supercritical nature of the bifurcation. Moreover, it must be noted that again, the bifurcation can appear regardless of the bistable regime.
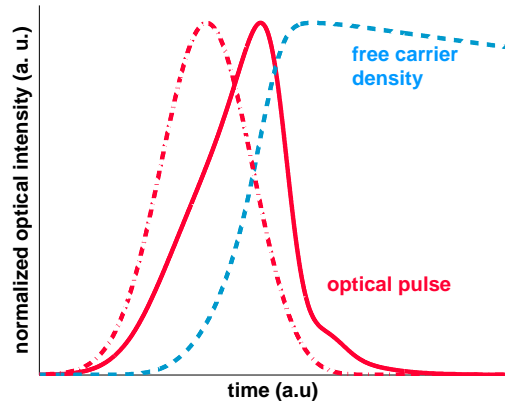
Figure 4.12: Time evolution of the carriers density with respect to the pulse time scale (blue dashed curve). Energy in the cavity for input power below the critical threshold (red dash-dotted curve) and for input power above the critical threshold (red solid curve).

4.4 Spectral broadening induced by free carriers

To understand the spectral modulation of an optical pulse involved in nonlinear dynamics where the free carriers dispersion dominate, it is useful to resort to a numerical implementation Eqs. (4.1)-(4.6) in which Kerr effect and nonlinear losses are neglected. Fig. 4.12 depicts the qualitative evolution of the free carriers density on the time scale of the optical pulse [36]. The relevant normalized time $\tau = 40$ is chosen, so that the recombination time is much larger than the cavity lifetime. With a normalized detuning $\delta = -3$, when the input power is below of the critical threshold, no appreciable self-switching happens (red dash-dotted). Conversely, for pumped power above the critical threshold, the pulse is fast switched in the cavity exhibiting weak relaxation oscillations due to the feedback mechanism (red solid curve). The shift induced in the optical phase is proportional to the number of generated carriers for unit of volume. Since the free carriers density follows the integral of the pulse shape, the trailing edge of the pulse sees a higher phase shift than the leading edge. This causes an asymmetric spectral broadening. As
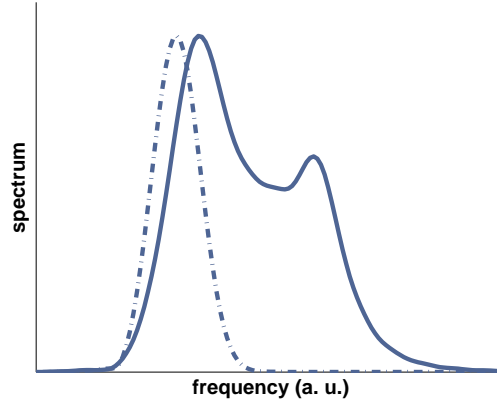
Figure 4.13: Spectral response in the case of input power below critical threshold (dashed line) and in the case above critical threshold (solid line) for the pulse in Fig. 4.12.

it is shown in Fig. 4.13 the spectrum of the pulse results blue-shifted and broadened as result of the index change.

4.5 Carriers diffusion in semiconductor photonic crystals

Another relevant effect that must be considered in the limit of two photon absorption dynamics, is the diffusion of free carriers, that can become one of the main causes that affects carriers recombination in periodic nanostructures. This section is focused on the analysis of photogeneration caused by TPA, in particular, the purpose is to investigate how the carriers lifetime is affected by the PhC geometrical features.

The rate equation that rules the dynamics of carriers generated by illumination with an optical source of intensity I^2 is given by

$$\frac{\partial N}{\partial t} = \frac{\beta I^2}{2\hbar\omega} - \frac{N}{\tau_b} + D\nabla^2 N \qquad (4.28)$$

where τ_b is the recovery time of the bulk semiconductor material, β is the nonlinear TPA coefficient, and $2\hbar\omega$ is the two photon energy, with $\hbar$ the

Planck constant and ω the frequency. The SRH term in the Eq. (4.28) describes the diffusion of the charges weighed by the diffusion coefficient D (in unit of cm^2/s). The diffusion effect is the mechanism according to which the carriers spread proportionally to the gradient of their concentration, and gives a significant contribution to the carriers lifetime and then to the switching recovery time. In fact, surface recombinations are related to diffusion effects according to the following Neumann boundary condition

$$D\nabla n|_S = \mathbf{v}_s n|_S \qquad (4.29)$$

with S the surface where charges recombine, and $\mathbf{v}_s$ the surface velocity of the recombinations. Surface recombinations in semiconductors describe the annihilation of charges at discontinuities or defects of the crystal and play a critical role as the device dimensions become small. The effective carriers lifetime is then given by

$$\frac{1}{\tau_{eff}} = \frac{1}{\tau_b} + \frac{1}{\tau_s} \qquad (4.30)$$

where τ_r arises from recombinations in the bulk semiconductor, and τ_s is determined by recombinations which occur at the surfaces of the sample. Although it is still under investigation, by following the dissertation in [38], [39], here an expression of τ_s is obtain by evaluating the steady state $(\partial N/\partial t = 0)$ of the rate equation Eq. (4.28). In two dimensions the continuity equation becomes

$$\int_S \left(G - \frac{n}{\tau_r} \right) dS = \int_S \nabla^2 n \, dS \qquad (4.31)$$

where $G = \beta I^2/2\hbar\omega$ is the generation term and S is a 2D surface. In a PhC triangular lattice with period a and holes radius $r = \delta a$ (with $0 < \delta < 0.5$), Eq. (4.31) can be evaluated by considering the integral over the hexagonal unit cell of area $S = \sqrt{3}/2a^2$. By the divergence theorem, the SRH of Eq. (4.31) can be expressed as the one dimensional integral around the curve γ_S that bounds the S surface:

$$\int_S D\nabla^2 n \, dS = \int_S \nabla \cdot (D\nabla n) dS = \int_{\gamma_S} D\nabla n \cdot \mathbf{l} \, dl \qquad (4.32)$$

where $\mathbf{l}$ is the unit vector perpendicular to the path of integration, and γ_S is composed by both the hexagonal perimeter of the unit cell and the hole

boundary. By considering the boundary condition in Eq. (4.29) with $\mathbf{v}_s = 0$ on the external cell edge and $\mathbf{v}_s \neq 0$ on the hole edge, the Eq. (4.32) becomes

$$\int_S \left(G - \frac{n}{\tau_b} \right) dS = \int_{\gamma_S} n\mathbf{v}_s \cdot \mathbf{l} \, dl \tag{4.33}$$

The integration can be easily performed in polar coordinates (ρ, θ and $\mathbf{l} = \bar{\rho}$) by considering the optical intensity I^2 spatially uniform in the domain and a surface velocity direct along the radial coordinate. The result is

$$\left(G - \frac{n}{\tau_b} \right) \left(\frac{\sqrt{3}}{2} a^2 - \pi r^2 \right) = 2\pi r n v_s \tag{4.34}$$

The effective recombination time $\tau_{eff} = G/n$ is then given by

$$\frac{1}{\tau_{eff}} = \frac{1}{\tau_b} + \frac{2\pi \delta v_s}{\frac{\sqrt{3}}{2}a - \pi \delta^2 a} \tag{4.35}$$

from which follows the expression for the time of surface recombinations τ_s:

$$\tau_s = a \frac{\left(\frac{\sqrt{3}}{2} - \pi \delta^2 \right)}{2\pi \delta v_s} \tag{4.36}$$

The latter expression highlights as the recovery time induced by surface recombinations can be tailored by means of the geometrical features of the crystal. The ratio δ between the holes radius and the lattice constant a seems to be a critical parameter. As an example, when the recombination velocity is $v_s = 10^4 m/s$ in a PhC with period $a = 430nm$ and $\delta = 0.20$, τ_s is about $25ps$. An increasing of δ up to 0.30 leads τ_s to be almost $13ps$, and with a further increasing until $\delta = 0.40$, τ_s decreases to approximately $6ps$ becoming comparable to the temporal duration of the signals processed in the devices.

4.6 Testing the 2D-FDTD FCD modeling by comparison with the CMT theory
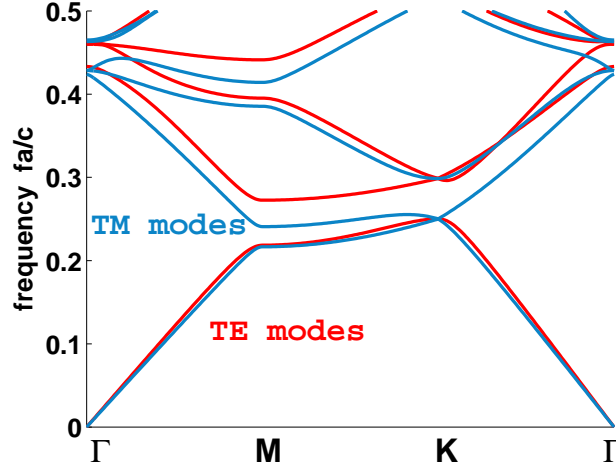
Figure 4.14: Photonic band structure for a triangular lattice of air holes in bulk material with $n = 2.73$. The crystal shows a complete band gap for TE modes (red curves), whereas the gap is close for TM modes (blue curves). The frequency is expressed as dimensionless ratio fa/c where a is the lattice constant and c the speed of light. In the horizontal axis are reported the in-plane wavevector values at the edges of the irreducible Brillouin zone from Γ to M to K.

Free carriers dispersion has been deeply analyzed in section 4.3. In this section the 2D-FDTD results obtained by numerical implementation of the nonlinear equations previously described, are compared with the CMT model. The structure studied is a 2D PhC of air holes in a triangular lattice with period $a = 430nm$, holes radius $0.22a$ and linear refractive index of the bulk material $n = 2.73$. As shown in Fig. 4.14, the structure exhibits a complete band gap for TE polarized light. A high-Q H0 cavity is realized by shifting of $0.16a$ two nearest holes [40]. The cavity is side-coupled to a waveguide obtained by removing a row of holes in the ΓK direction (see Fig. 4.15). In the side-coupled configuration, the transmission at the end of the waveguide is "'Off"' when the cavity is on resonance. This can be obtained
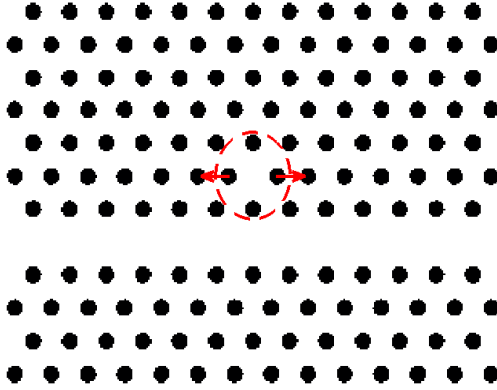
Figure 4.15: 2D PhC domain. The structure consists of a H0 cavity obtained by shifting two nearest holes and a linear defect realized by removing a line of holes. The cavity is side-coupled to the waveguide resulting in a deep of the transmission when the cavity is on resonance.

by the following linear CMT model:

$$\frac{\partial a}{\partial t} = i\omega_0 a - |k_1|^2 a + k_1 s_{in}$$
$$s_{out} = 1 - k_1^* a \tag{4.37}$$

where ω_0 is the cavity resonance, k_1 the coupling coefficient between the cavity and the waveguide, and s_{in} and s_{out} are the intensities in the input and output waveguides, respectively. The output transmission, shown in Fig. 4.16, is then given by

$$T_{out} = 1 - \frac{|k_1|^2}{i(\omega - \omega_0) + |k_1|^2} \tag{4.38}$$

 To investigate the nonlinear frequency blue-shift induced by free carriers dispersion, FDTD simulations are performed by means of the set of equations described in the section 4.2.2 without the implementation of the Kerr effect and nonlinear polarization responsible of losses, namely $\mathbf{P}_{TPA}$ and $\mathbf{P}_{FCA}$. The TPA coefficient used is $\beta = 10.2 cm/GW$, while the carrier lifetime has been fixed at $\tau_r = 8$ ps. For the diffusion effect, a value of the diffusion
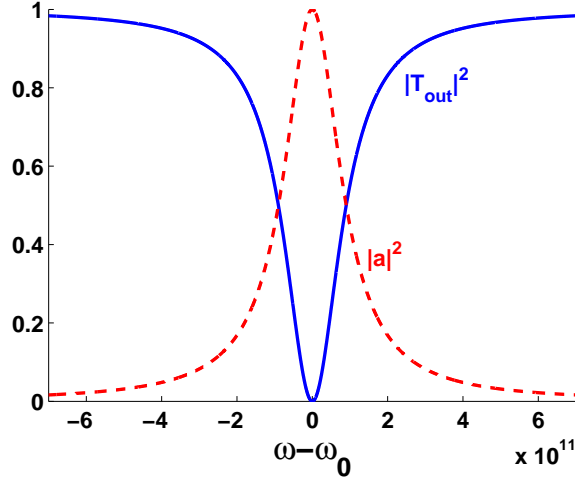
Figure 4.16: Linear transmission of a cavity side-coupled to waveguide. The transmission is "'Off"' (blue curve) when the cavity is on resonance (red curve).

coefficient comparable to that is measured in Silicon, i.e. $D = 35cm^3/s$, has been used. The structure is pumped via a $10ps$ Gaussian pulse lunched into the waveguide with a detunign of $4nm$ with respect the cavity resonant wavelength. The cavity resonates at $\lambda_0 = 1718nm$ and exhibits a loaded quality factor Q of about 250 corresponding to a loaded cavity lifetime of about $0.46ps$. Therefore the driving pulse detuned by $4nm$ results in a normalized detuning $\delta = 1.16$, just sufficient to trigger self-switching. The energy stored in the cavity is extracted by numerical calculation of the following surface integral

$$E_n = \frac{1}{2} \int_S \epsilon_0 \epsilon_r |\mathbf{E}|^2 dS \tag{4.39}$$

where S is restricted to an area around the cavity. The result is shown in Fig. 4.17. Subsequently, the envelope is evaluated by low-pass filtering of the energy waveform. Fig 4.18 shows the energy envelopes for two different values of the pumped power. In the first case, the optical intensity injected in the waveguide is not sufficient high to trigger the switching, and the energy level in the cavity remains low. In the second case, when the input intensity is large enough, the signal is fast switched in the cavity by the bistable effect. In Fig.
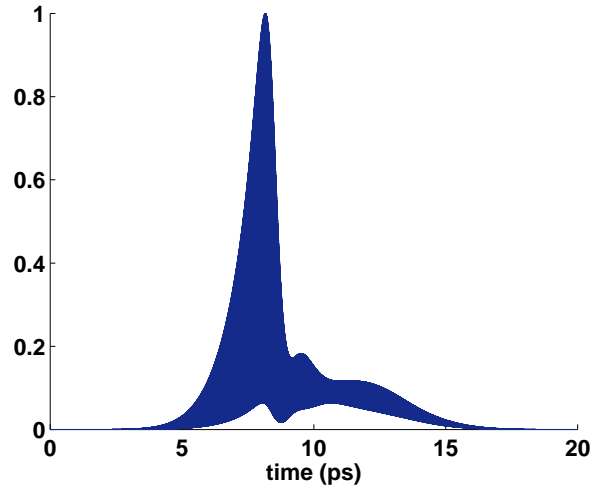
Figure 4.17: Nonlinear 2D-FDTD time evolution of the energy stored in the cavity when bistable switching is achieved.

4.18 the red dashed curve is referred to the below critical threshold case and the red solid curve to the above critical threshold case. The time evolution displayed by the blue thin curve, is the result obtained by a CMT simulation, where the relevant coefficients are extrapolated by linear FDTD calculations. The qualitatively bistable behavior evaluated by the CMT model is in good agreement with respect to that obtained by the nonlinear FDTD simulations. However, the CMT curves can not perfectly overlap with the FDTD ones, due to the FDTD implementation that takes into account the additional contribution of diffusion effects in the carriers temporal evolution. Fig. 4.19 shows the spectral shapes in the case in which the signal is not switched (dashed blue curve) and in the case in which the signal is switched in the cavity (solid blue curve). Moreover, when the bistable effect is achieved, the spectrum is broadened and shifted towards lower wavelength.

69
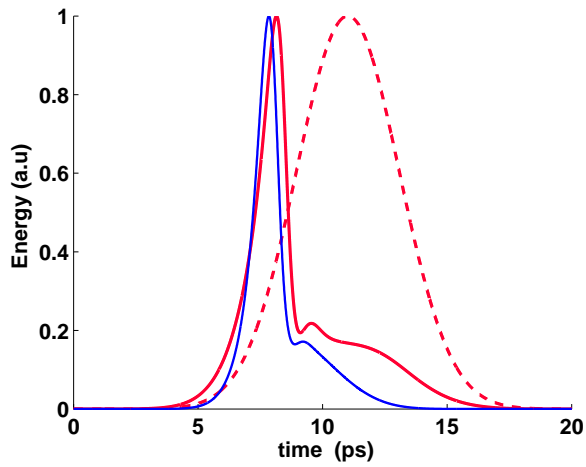
Figure 4.18: Nonlinear 2D-FDTD time evolution of the cavity energy envelope when switching is not achieved (red dashed curve) and when the bistable switching is triggered above threshold (red solid curve). The FDTD dynamics is qualitatively compared with a CMT simulation (thin blue curve).
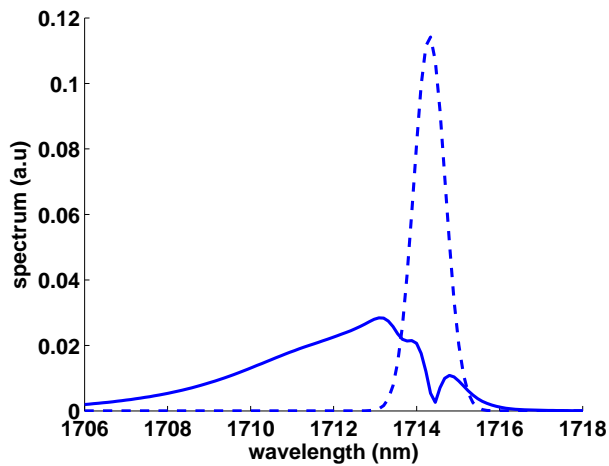
Figure 4.19: Spectral shape of the energy waveform in the two cases of Fig. 4.18: when the switching is not triggered the spectrum is undistorted (dashed blue curve) whereas, when the input power is high enough to give rise to a bistable effect, the spectrum is broadened and blue shifted (solid blue curve).
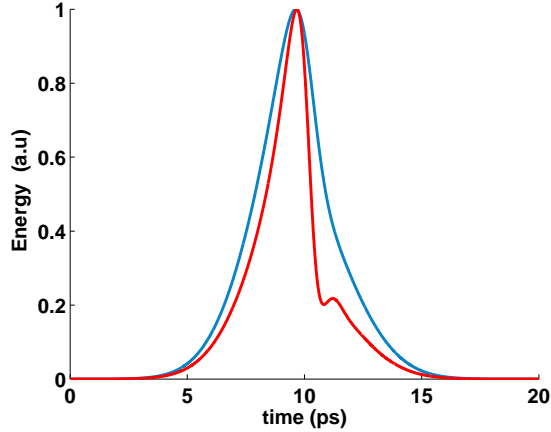
Figure 4.20: CMT modeling of bistable switching triggered by free carriers dispersion in the case in which nonlinear losses are neglected (red curve) and in the case in which nonlinear losses are taken into account (blue curve).

4.7 The effect of nonlinear losses

An issue of great interest is to investigate how the nonlinear losses due to two photon absorption and absorption for free carriers generated by TPA can degrade the switching performances.

The structure modeled is still the PhC cavity side-coupled to the waveguide analyzed in the previous section. Fig. 4.20 compares the CMT dynamics for the two cases: bistable switching induced by free carriers dispersion without nonlinear losses (red curve) and bistable switching when TPA nonlinear losses are accounted for (blue curve). By analyzing the temporal evolution displayed in figure, it is clear that the effect of losses induced by two photon and free carriers absorption, produces a smoothing effect of the energy waveform during the bistable dynamics. The same qualitative evolution can be observed by comparing the temporal dynamics obtained by nonlinear FDTD simulations. To this end, all nonlinear third order polarizations have been included into the 2D-FTDT code. For the cross-section that accounts for the losses induced by free carriers absorption, a coefficient $\sigma_{FCA} = 9.3(\lambda_0/\mu m)^{2.3}$ has been used. This coefficient is comparable to that known by measures in semiconductor materials such as Silicon or GaAs. Fig 4.21 shows the results
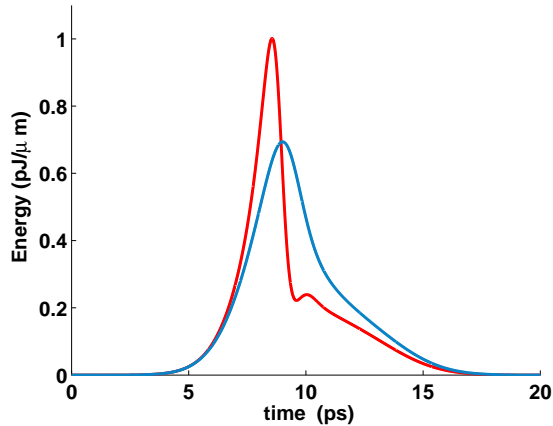
Figure 4.21: 2D-FDTD modeling of bistable switching induced by free carriers dispersion when TPA losses are not incorporated into the code (red curve), and when nonlinear losses are included (blue curve). The energy is plotted in $(pJ/\mu m)$ units. Comparison between the intensity peaks shows that owing to the nonlinear losses, a degradation of $1.59dB$ is observed in the switched energy.

for the two different modeling: bistable dynamics induced by free carriers dispersion when losses are not included (red curve), and bistable dynamics when losses are incorporated into the code (blue curve). As predicted by the CMT simulations, the temporal evolution of the cavity energy results to be smoothed by the nonlinear losses. Furthermore, by comparing the peak values in the two cases shown in Fig. 4.21, a degradation of about $1.59dB$ in the switched energy caused by the nonlinear losses is observed.

4.8   Switching by pump-probe operations

The required operating energy for a cavity based switch scales as V/Q^2 or $V/Q\sqrt{Q}$ by exploiting Kerr or TPA nonlinearity, respectively, where Q is the cavity quality factor and V the modal volume. Small volume and high-Q photonic crystal cavities can therefore realize optical switching with a large reduction in operating power due to their strong light confinement.
As discussed for the switching in Kerr photonic crystal, the pump-probe op-

erations, where the excitation of the cavity for the signal processing is driven by a pump signal, can be very interesting due to their potential with respect to the control of speed and switching efficiency.

In this section pump-probe operations are studied in a PhC H0 cavity coupled to two waveguides in an in-line configuration. The PhC has the same properties as those analyzed above. In detail, it is a triangular lattice of air holes in high contrast bulk material with refractive index $n = 2.73$. The period of the crystal is $a = 430nm$ and the holes radius is $r = 0.22a$. To enhance the coupling between the cavity and the two waveguides, the holes radius of the first two rows in the waveguides has been increased of $r_{wg} = 0.34a$. Thereby, the cavity exhibits a resonance at $\lambda_0 = 1583nm$ with a loaded quality factor $Q = 980$. The structure is depicted in Fig. 4.22. In the in-line configuration the cavity is coupled to two separated waveguides, so that the transmission in the output port is in the "'On"' state when the cavity is on resonance. This can be suitably predicted by the following linear CMT model:

$$
\begin{aligned}
\frac{\partial a}{\partial t} &= i\omega_0 a - |k_1|^2 a + k_1 s_{in} \\
s_{out} &= -k_1^* a
\end{aligned}
\tag{4.40}
$$

with ω_0 the cavity resonance, k_1 the cavity to waveguide coupling coefficient, s_{in} the input and s_{out} the output signal, respectively. The system gives the following output transmission

$$
T_{out} = \frac{|k_1|^2}{i(\omega - \omega_0) + |k_1|^2}
\tag{4.41}
$$

that exhibits "'On"' output transmission at the cavity resonance.

Pump-probe operations have been analyzed with the nonlinear 2D-FDTD code. In order to investigate the bistable switching induced by free carriers dispersion, Kerr effect and nonlinear losses have been neglected. The nonlinear parameters of the material are the same as those used in previous section, i.e. $\beta = 10.2cm/GW$ for the TPA coefficient, $\tau_r = 8ps$ for the carriers recovery time, and $D = 35cm^3/s$ for the diffusion coefficient. For this configuration it is of particular interest the analysis of the tuning and detuning performances by switching "'On"' and "'Off"' the probe signal by means of the control signal. In the first case, both, pump and probe are $6ps$
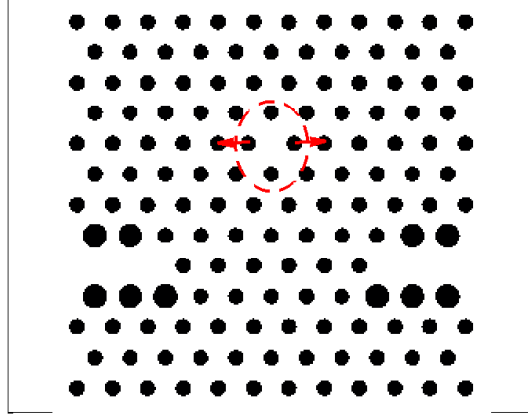
Figure 4.22: 2D PhC domain. The structure is composed by a H0 cavity coupled to an input and an output waveguide in an in-line configuration.

Gaussian pulses detuned of $\Delta\lambda = \lambda - \lambda_0 = -10nm$ with respect to the cavity resonance. This means that the driving signal switches "'On"' itself and, at the same time, switches "'On"' the probe signal, resulting in an enhancement of the probe output transmission that follows the cavity dynamics. Fig. 4.23 shows the cavity energy for different values of the control signal. The energy has been normalized with respect to its value when $P_{pump} = Off$ so that the switching contrast is emphasized. As it can be seen, the contrast is increased according to the level of the driving intensity.

In the second case, pump and probe are two $6ps$ Gaussian pulses. The pump has a negative detuning $\Delta\lambda = \lambda - \lambda_0 = -10nm$, whereas the probe has been setup to have a positive detuning $\Delta\lambda = \lambda - \lambda_0 = 5nm$. Thereby, when the pump self-switches by increasing the optical energy inside the cavity, owing to the blue-shift of the frequency induced by free carriers dispersion, the probe is switched "'Off"', resulting in a decrease of the output transmission. Fig. 4.24 shows the results of the simulations for different values of the peak power of the control signal. As expected, by increasing the driving intensity, the cavity energy is switched "'Off"' with deeper contrast.
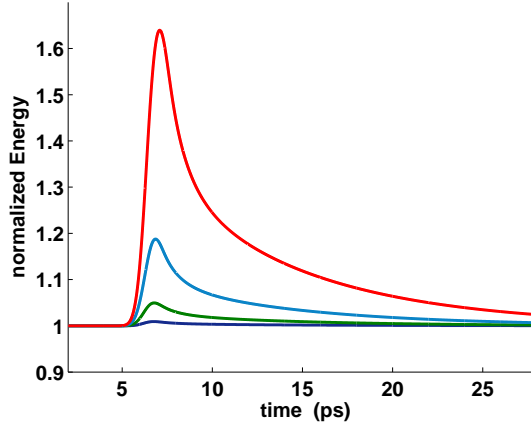
Figure 4.23: Tuning of the cavity by pump-probe operation. The energy curve are shown for different values of the input driving power: $P_{in} = 109mW/\mu m$ (dark curve), $P_{in} = 246mW/\mu m$ (green curve), $P_{in} = 438mW/\mu m$ (blue curve) and $P_{in} = 685mW/\mu m$ (red curve). The energy curves show an enhancement in the switching contrast as a result of the increased optical control intensity.
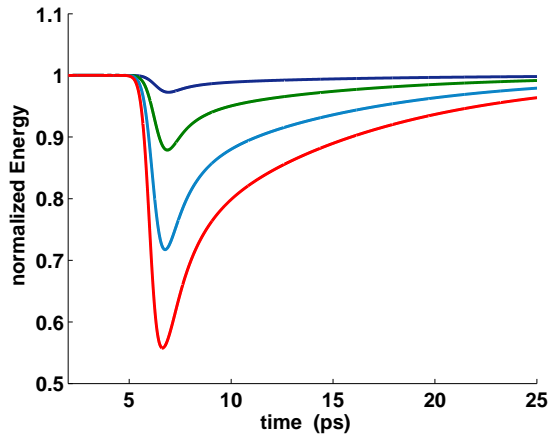
Figure 4.24: Detuning of the cavity by pump-probe operation. The energy curve are shown for different values of the input driving power: $P_{in} = 109mW/\mu m$ (dark curve), $P_{in} = 246mW/\mu m$ (green curve), $P_{in} = 438mW/\mu m$ (blue curve) and $P_{in} = 685mW/\mu m$ (red curve). The energy inside the cavity is decreased when the input control intensity is increased.

4.9 Comparison between 2D-FDTD nonlinear results and experimental data

Up to now the 2D-FDTD nonlinear code has been checked by comparison with CMT models and by testing qualitatively the correctness of the results concerning to the tuning and detuning operations in PhC cavities. The goal was to demonstrate the potential switching features of such structures in nonlinear regime induced by two photon absorption, as well as to check the right code operations. Nevertheless, to keep down the computational cost, simulations have been performed by modeling a PhC domain of about 15×15 periods, that does not corresponds to the realistic dimensions of structures employed in experimental frameworks. In particular, the small size of the simulated domain was responsible for the low quality factor of the cavities seen so far. Hence, while the small PhC domain allowed us to perform important tests with very low computational cost, it did not give any knowledge about the realistic performances of the devices. Moreover, the nonlinear parameters employed so far do not correspond to the realistic parameters of the semiconductor materials used to build the signal processing devices. In this section, in order to set up a simulation tool aimed at investigating the dynamics of PhC switching, the correct operations of the code are validated by comparing the numerical results with experimental data.

Measurements are performed over a GaAs PhC slab sample, involving a single H0 nano-cavity coupled to two (input and output) sections of a line-defect waveguide, in an arrangement equivalent (topologically) to the one reported in [9]. The cavity, whose spectral response is shown in Fig. 4.25 (top) resonates at $\lambda_0 = 1551.84nm$ with a loaded quality factor $Q = 1800$, which corresponds to a spectral FWHM $\Delta\lambda = 0.56nm$. In order to investigate the nonlinear behavior of the sample, non-degenerate pump-probe experiments have been performed, the nonlinearity being driven by the strong pump pulse. Figure 4.25 (bottom) shows the typical outcome in terms of the dynamics of the transmitted probe pulse, when the pump wavelength is held on resonance while the probe is blue-shifted to the $-3dB$ point of the cavity spectral response. By increasing the pump power up to few tens of μW, a dramatic increase of the probe transmission is observed when the
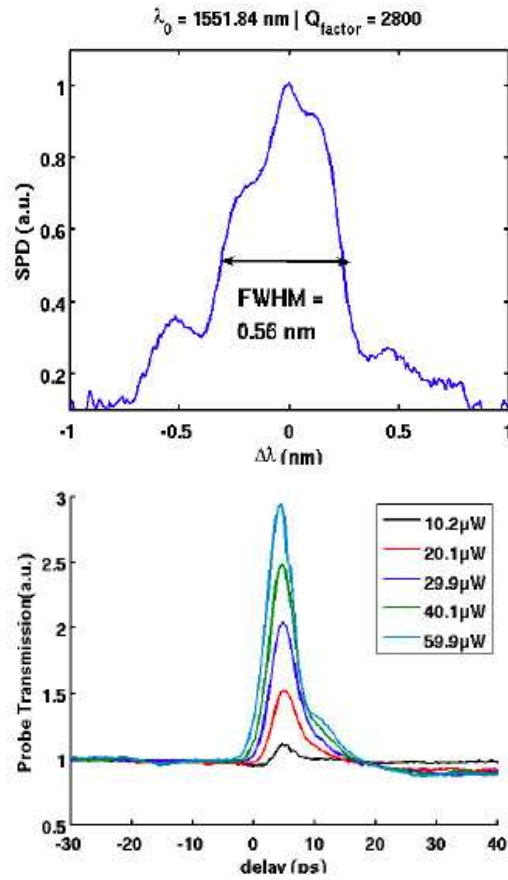
Figure 4.25: Spectral response of the GaAs H0 nanocavity (top) and time-resolved dynamics of the probe transmission (bottom) in a waveguide side-coupled to the nano-cavity. High probe transmission (switching) is obtained in pump-probe configuration with the pump on resonance and the probe blue-shifted at -3 dB point of the spectal response.

probe overlaps temporally with the pump. This is a signature that the response of the cavity is dominated by the plasma effect (carriers generated via TPA) which is responsible for a pump-induced blue-shift of the resonance, while the effect of nonlinear losses remains marginal. The data shows that the dynamics of the carriers is extremely fast with a relaxation time of few psec, while a good switching contrast of $1 : 3$ is achieved at a pump power of $60mW$. The use of membranes allows to give a reasonable description in 2D employing effective index method in the vertical direction, with a value

77
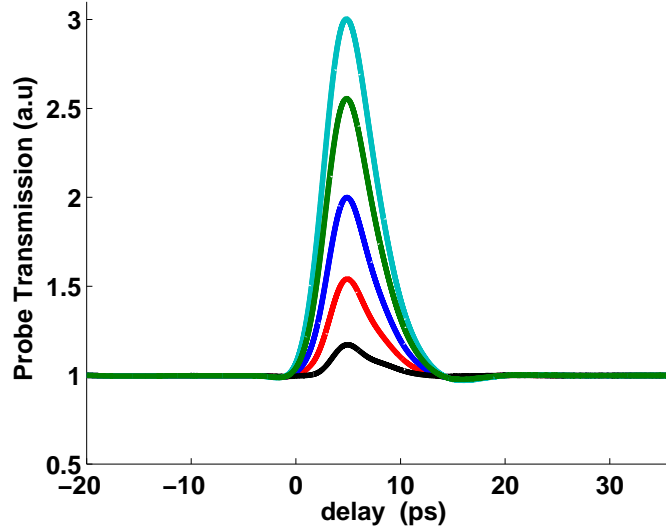
Figure 4.26: Dynamics simulated by means of the nonlinear 2D-FDTD code of the structure characterized in experiments.

$n = 2.67$ and perfect matched layer (PML) absorbing boundary conditions in the plane of the PhC. To account the nonlinear effects in GaAs, a Kerr coefficient $n_{2I} = 1.5 \times 10^{-14} cm^2/W$ and a TPA coefficient $\beta = 10.2 cm/GW$ have been used. For the carriers dynamics the recovery time has been taken $\tau_r = 6ps$ with a diffusion coefficient $D = 237,86 cm^2/s$. To obtain the exact linear response, a sufficiently large domain of simulation (23×41 cells) has been chosen, that sets the realistic cavity quality factor to be affected only by the coupling with the waveguide. Moreover, to obtain operative informations about the transmission efficiency, in the FDTD code the calculus of the Poynting flux at the bus output port has been implemented, and the outcome has been processed with a low-pass filter to extract the envelope. The results are shown in Fig. 4.26. By comparing with Fig. 4.25 it turns out that the outcomes of the simulations are in good agreement with experimental data, and this confirm the correct set up of the code.
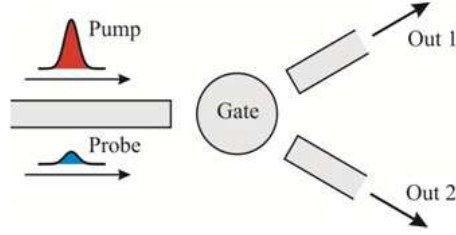
Figure 4.27: Schematic of a three-ports AOG operating in a degenerate fashion with a pump and a probe at different wavelengths.
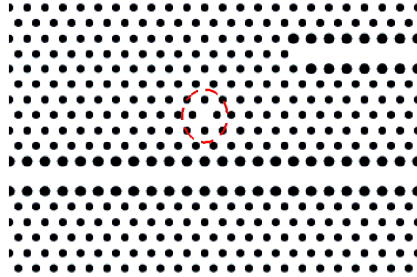
Figure 4.28: Domain of simulation.

4.10   Design of a three-ports switching device

In this section a first three-ports configuration for ultra-fast optical switching (see scheme in Fig. 4.27) is studied. The device is composed by a triangular lattice PhC of air holes in GaAs membrane. The lattice constant is $a = 430nm$ and the holes radius is $0.22a$. As depicted in Fig. 4.28, the structure consists of a H0 cavity side-coupled to a bus (low) waveguide and a drop (high) waveguide. The radius of the two first rows in both, bus and drop waveguides, has been increased to enhance the coupling with the cavity.

FDTD simulations aimed to investigate pump-probe operations have been performed with the same nonlinear parameters for GaAs material as described in the last section. As shows Fig. 4.29, the cavity presents a resonance at $\lambda_0 = 1456nm$. In order to obtain the best performances in terms of switching contrast, some tests have been made by changing the probe
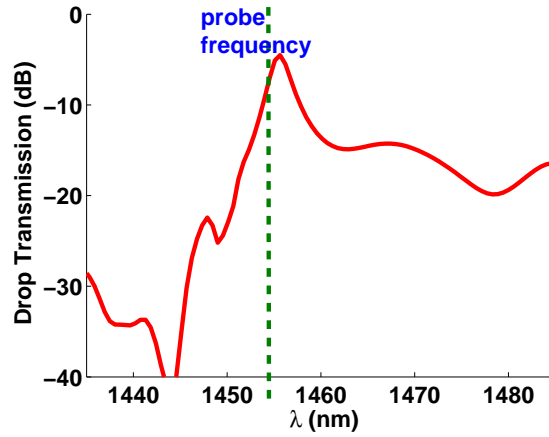
Figure 4.29: Linear drop transmission in dB

detuning with respect to the cavity resonance and maintaining fixed the frequency pump blue shifted by $0.5nm$. In Figs. 4.30-4.35 the normalized $(P_{out}(pump = On)/P_{out}(pump = Off))$ power ratio in the bus and drop waveguides for probe detuning from $1nm$ to $3nm$ are shown. As expected by the knowledge concerning to the performances of switching via PhC cavities [9], and in good agreement with them, the maximum switching contrast not exceed 3.5. This occurs with the probe blue shifted by $3nm$, as displayed in Fig. 4.35, where the required pump power and the corresponding probe switching contrast obtained have been also indicated. Further increasing the probe detuning does not lead to any improvement in the switching performances.
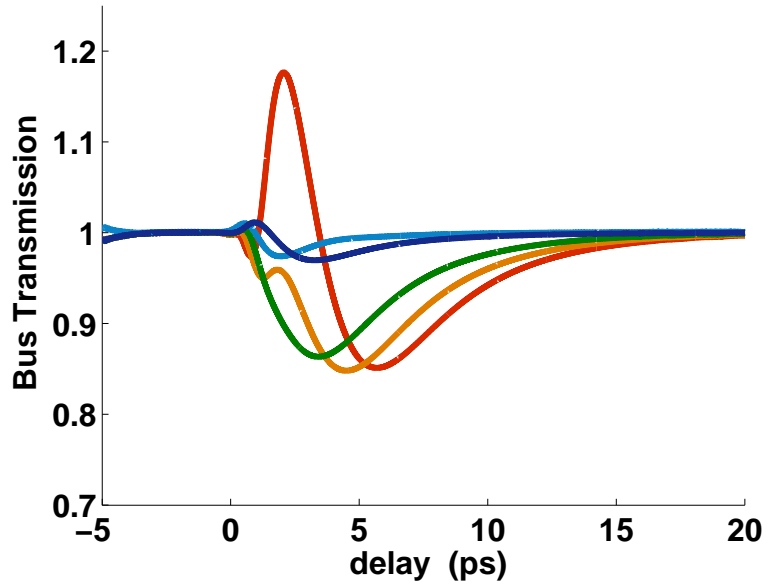
Figure 4.30: Bus switching efficiency with probe detuned by $1nm$.
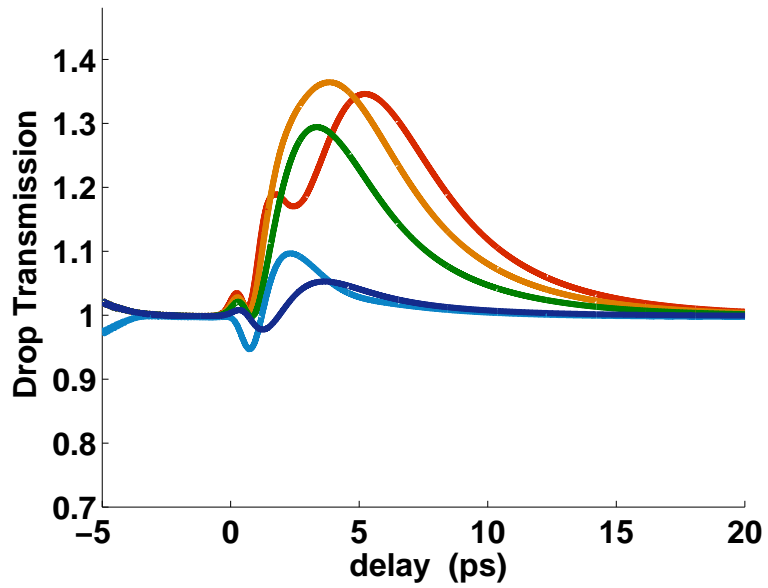
Figure 4.31: Drop switching efficiency with probe detuned by $1nm$ that shows a maximum SC achievable of about 1.3 (red curve).
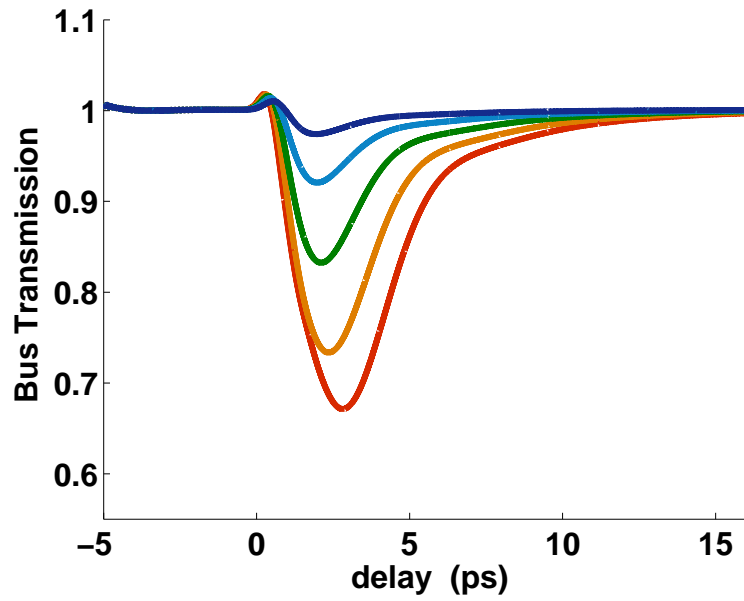
Figure 4.32: Bus switching efficiency with probe detuned by $2nm$.
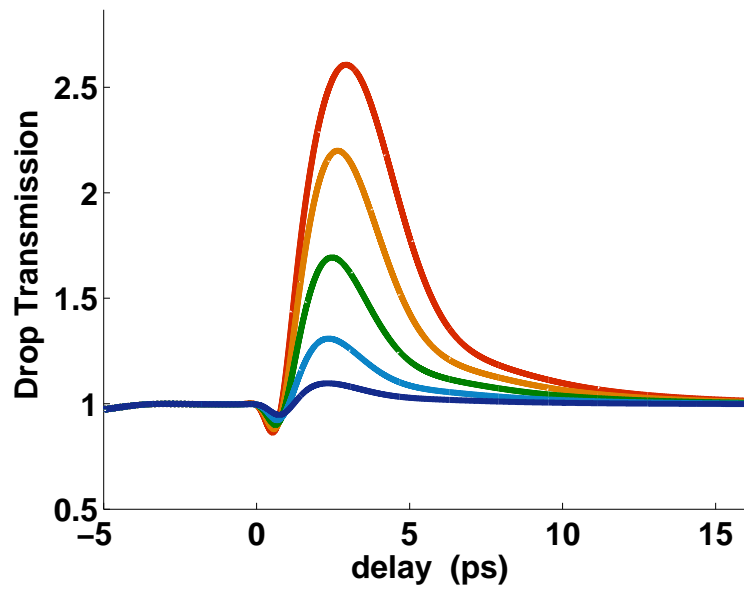
Figure 4.33: Drop switching efficiency with probe detuned by $2nm$ that shows a maximum SC achievable of about 2.6 (red curve).
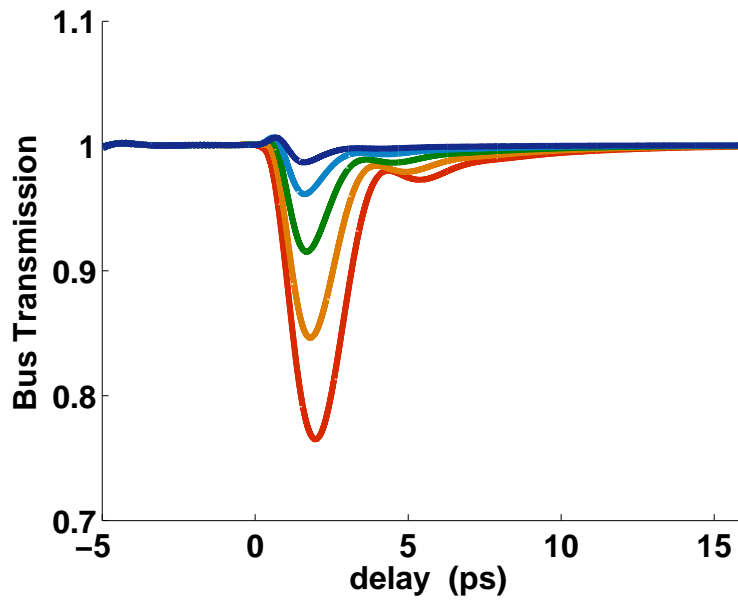
Figure 4.34: Bus switching efficiency with probe detuned by $3nm$.
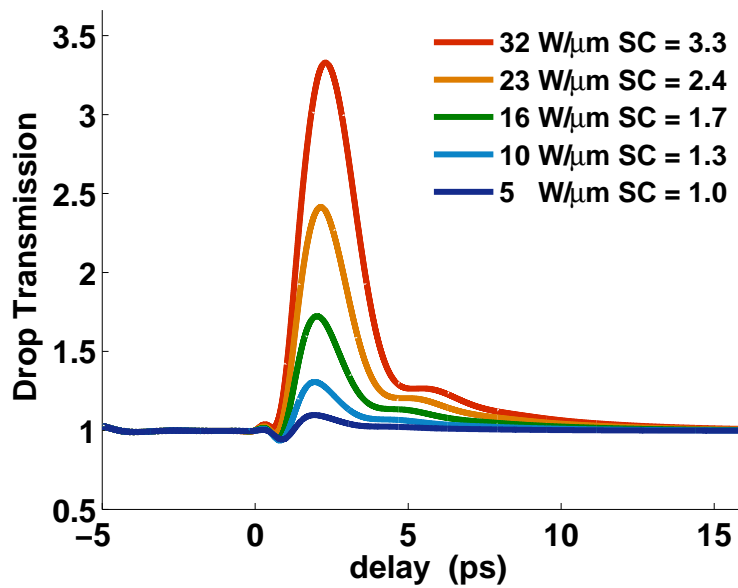
Figure 4.35: Drop switching efficiency with probe detuned by $3nm$ corresponding to the best performances: maximum achievable SC of about 3.3 (red curve).

4.11 Three-ports All Optical Gate (AOG): optimized design

Finally, in this section some optimized topologies of a three-ports All Optical Gate (AOG) are developed. The aim is to enhance the performances of the three-ports switching device previously described. The bottom line idea is that a better switching contrast can be obtained by exploiting the interference between multi-resonators that can exhibit very sharp transmission. In this perspective, the optimization is pursued by numerically investigating different PhC topologies.

The basic structure is the same PhC discussed in the previous section that has been modeled by means of the 2D-FDTD nonlinear code by using the nonlinear coefficients for GaAs membrane material. As before, the device is made of a photonic crystal triangular lattice of air holes in a thin semiconductor membrane. All the configurations share the same lattice constant $a = 430nm$, while holes radius is $r = 0.22a$. The waveguides are W1 ones, with an inner row of holes with radius $0.29a$. A set of two or three H0 coupled cavities with different parameters is used.

In the first topology shown in Fig. 4.36 (a), two coupled H0 cavities with shifts of $0.18a$ and $0.19a$ act as multi-frequency resonator to switch the signal from bus (bottom waveguide) to drop (top waveguide). As shown in Fig. 4.36 (d) the interference between the cavities makes a very steep peak of transmission that can lead to high switching performance in pump-probe operations with very low driving power when the probe is slightly blue-detuned with respect to the maximum of the drop transmission. The linear transmission along the through channel exhibits an insertion loss of $0.22dB$ at the operating (probe) frequency (see Fig. 4.36 (c)). Furthermore, the linear transmission evaluated in the drop channel exhibits a sharp change ($30dB$) in the transmission as the frequency changes by $1nm$. Switching in pump-probe regime has been investigated by employing a $6ps$ Gaussian pump pulses to drive a continuous-wave probe. The dynamical response (pump-probe degenerate operation) modeled by means of the 2D-FDTD nonlinear code exhibits a switching contrast $SC = 55$ in the drop channel and a switching contrast $SC = 0.45$ in the through one (see Fig 4.37). This has been obtained with
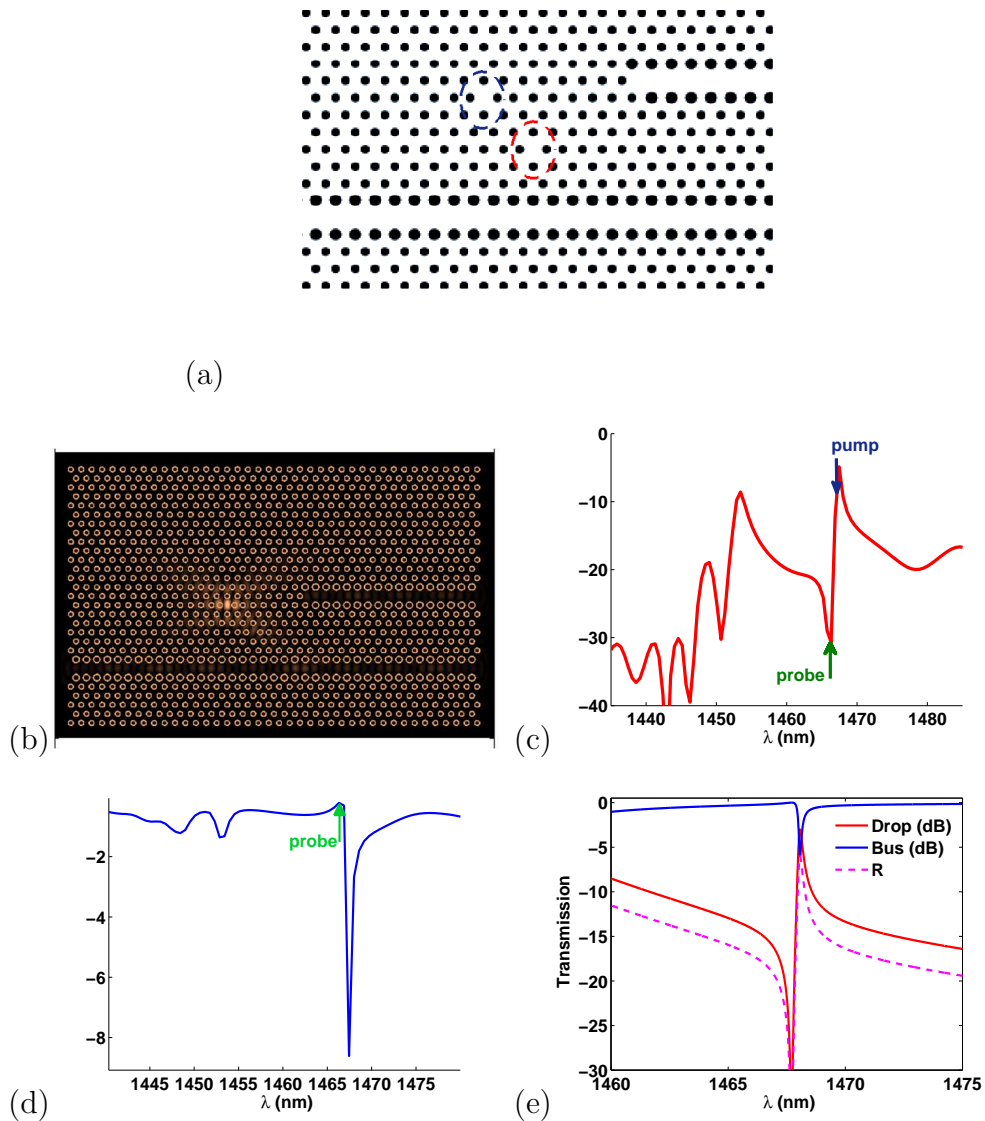
Figure 4.36: Optimized topology of three-ports switching device with two cavities. (a) PhC structure. (b) Pattern of the magnetic field on resonance corresponding to high drop transmission. (c) Linear bus transmission in dB. (d) Linear drop transmission in dB: in figure pump and probe wavelengths used for nonlinear operations are indicated. (e) Linear transmission evaluated by an equivalent CMT model.

(a)

(b)
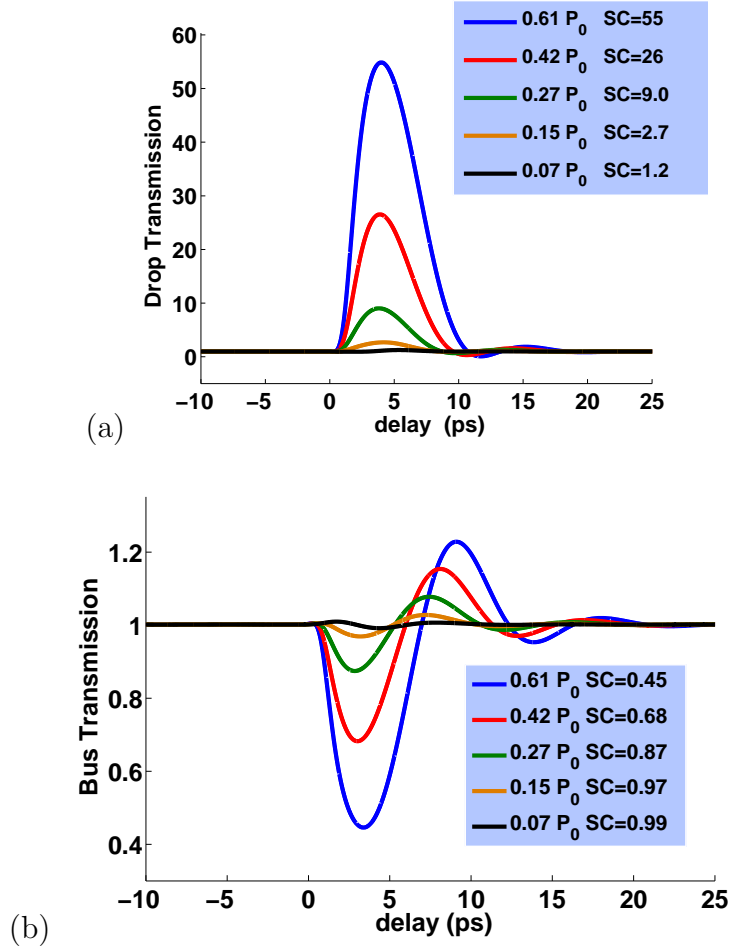
Figure 4.37: Two-cavities design. Nonlinear transmission at the drop (a) and through (b) port evaluated for different levels of input power.

(estimated) input peak power $P_0 \approx 350mW$, which is comparable to that required to have a $SC = 3$ in the simple device realized with only one cavity. In the second topology, a system of three cavities with shifts of the holes set to $0.22a$, $0.19a$ and $0.16a$ is used (see Fig 4.38 (a)). Figs. 4.38 (b) and (c) show the linear transmission in the through and drop port, respectively. The linear transmission in the drop presents a sharp change of $30dB$ as the frequency is shifted by $1nm$. The insertion loss in the through channel evaluated at the probe frequency is $0.5dB$. In this case, in pump-probe degenerate operation, the expected SC is 205, still with the same power level as above (see Fig. 4.39 (a) and (b)).

(a)

(b)

(c)
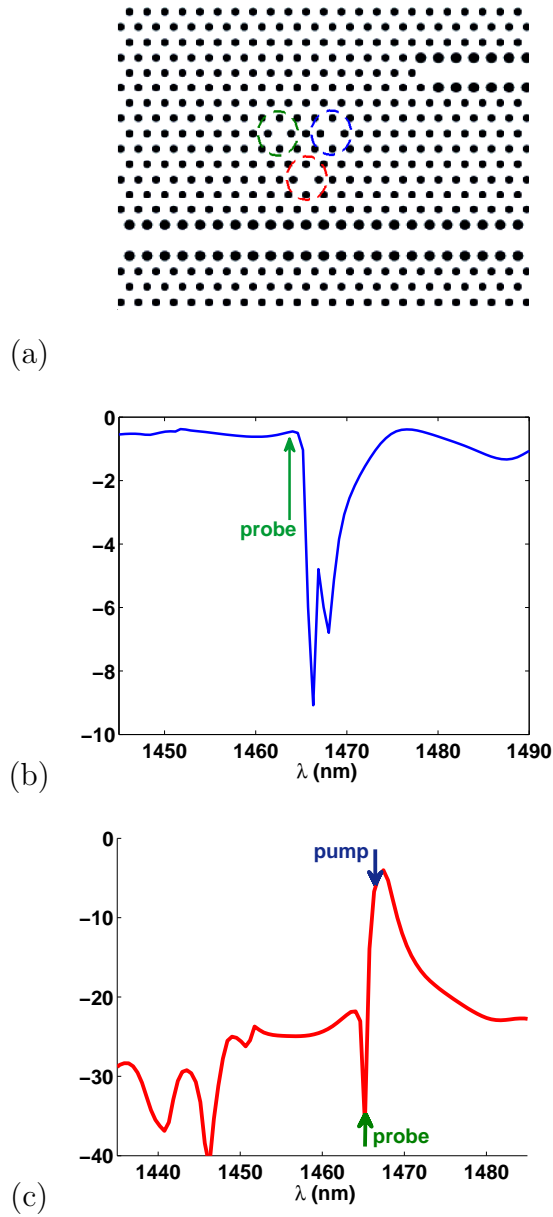
Figure 4.38: Optimized topology of three-ports switching device with three cavities. (a) PhC structure. (b) Linear bus transmission in dB. (c) Linear drop transmission in dB: in figure pump and probe wavelengths used for nonlinear operations are indicated.
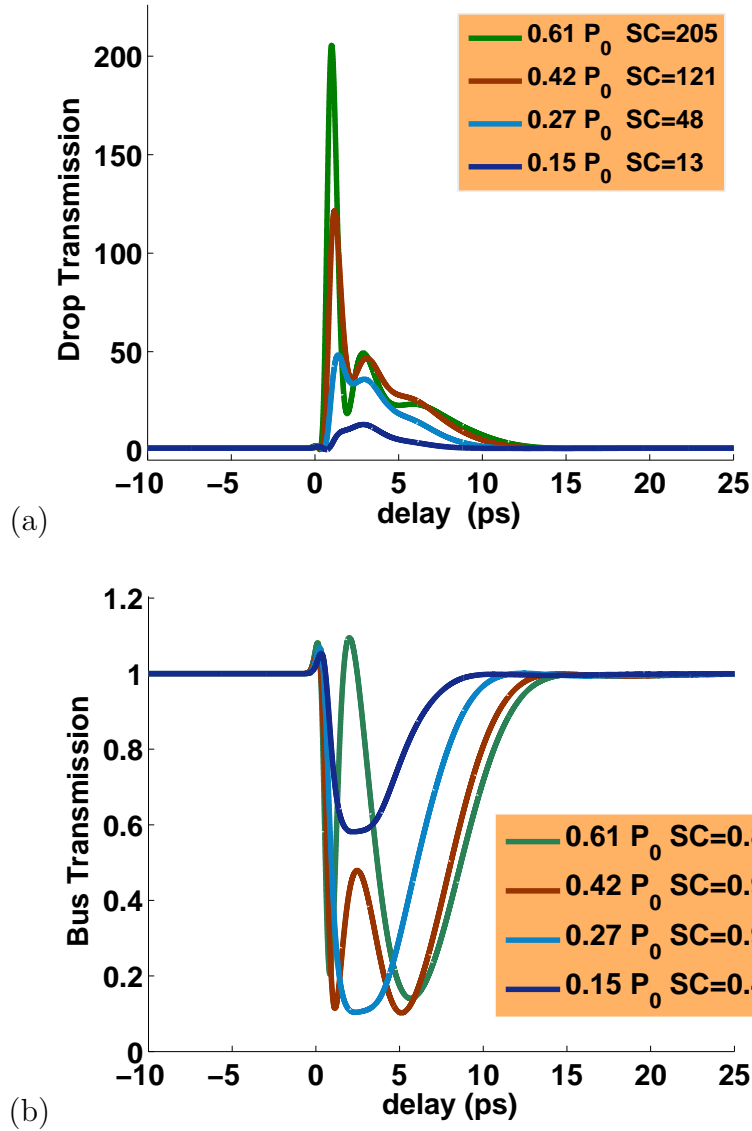
Figure 4.39: Three-cavities design. Nonlinear transmission at the drop (a) and through (b) port evaluated for different levels of input power.

Both configurations with two and three cavities exhibit a highly improved switching contrast by means of interference between the resonant cavities introduced in the gate section. The efficiency in terms of the SC is shown at different values of input power in Figs. 4.37 and 4.39. The drop efficiency (power transferred from input bus to output drop) is about 30% for the first

configuration and about 40% for the second configuration. The reflected power is of about 50% in both cases.

4.12 Summary

In this chapter the most relevant nonlinear effects present in semiconductor materials such as two photon absorption and free carriers dispersion as well as absorption induced by TPA have been analytically studied. All of these nonlinear effects have been incorporated in a 2D-FDTD code in order to model high-performances PhC switching devices. Finally, some optimized designs of a three-ports All Optical Gate have been analyzed. In particular, two different configurations have been reported, that in a pump-probe degenerate operation show a switching contrast of $SC \approx 50$ and $SC \approx 200$ respectively, resulting far superior to the performance of a single-mode cavity device operating at the same input power levels.

Conclusions

This thesis has been focused on the study of nonlinear effects in optical devices realized in semiconductor materials. The Kerr and two photon absorption nonlinearities have been deeply analyzed as dominant effects in standard semiconductors. In particular, the study has been developed by investigating device topologies based on photonic crystals but it should be emphasized that the results obtained here can be easily extended to any other settings involving different types of optical structures such as ring resonators and pohtonic wires.

A first interesting target of this thesis, was the analytical study of the bistable response in systems affected by TPA nonlinearities by means of the CMT model. In fact, this theoretical investigation highlighted some important features about the switching performances of an optical cavity coupled to a waveguide. In particular, the conditions in terms of the detuning between the cavity resonance and driving frequency able to trigger the switch have been obtained, and the performances in terms of switching efficiency have been related to the quality factor and the modal volume of the cavity.

Another important result is the implementation of a 2D-FDTD nonlinear code in which all the nonlinear effects have been incorporated. The realization of this numerical tool has firstly required to extend the governing equations that ruled the nonlinear effects to frameworks in which the electromagnetic field acquires a specific polarization. Furthermore, in order to validate the correctness of the simulations, different tests such as comparisons between the numerical outcomes and CMT models as well as comparisons between the FDTD results and experimental data have been performed.

Finally in the last part of this work, the knowledge acquired about the physic of the nonlinear effects, the analysis of theoretical models, the implemen-

tation of numerical tools, has been exploited for the design of new high-performances switching devices aimed to realize ultra-fast all-optical signal-processing. This latter results are currently the basis for the fabrication and characterization of a new generation of optical devices.

Appendix A

The Finite Difference Time Domain (FDTD) method

In this study numerical methods based on time domain techniques that use spatial and temporal discretization of the electromagnetic differential equations are applied. One of the best known and widely diffused is the finite difference time domain (FDTD) approach [26] whose general guidelines and advantages are briefly described in this appendix. The purpose is to introduce a scheme that is next extended to study the nonlinear dynamics in semiconductor materials.

The FDTD scheme applies the Yee's algorithm that solves Maxwell's curl equations for both electric and magnetic fields in time and space. In the Yee's algorithm the spatial domain is divided in cubic cells, so that the edge of each cube forms the three dimensional space grid. The $\mathbf{E}$ and $\mathbf{H}$ spatial components are positioned in this grid structure so that every $\mathbf{E}$ component is enclosed in a square of four circulating $\mathbf{H}$ components and vice versa (see Fig. A.1). Thereby, the method implicitly applies the Faraday and Ampere laws. In the time, the Yee's algorithm calculates the $\mathbf{E}$ and $\mathbf{H}$ components at temporal instants that differ of half time step $\Delta t/2$ (see Fig. A.2).

Insight into FDTD method can be obtained by considering for simplicity the homogeneous Maxwell's equations in a Cartesian coordinate system in
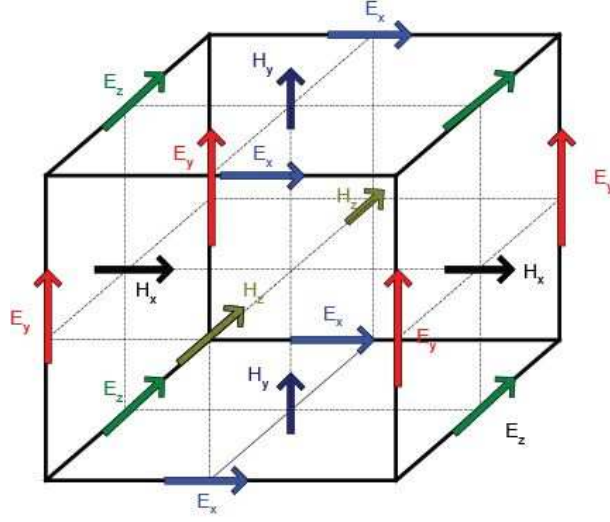
Figure A.1: Yee's scheme.

linear, isotropic, nondispersive three dimensional media:

$$
\frac{\partial E_x}{\partial t} = \frac{1}{\epsilon} \left[\frac{\partial H_z}{\partial y} - \frac{\partial H_y}{\partial z} - \sigma E_x \right]
$$
$$
\frac{\partial E_y}{\partial t} = \frac{1}{\epsilon} \left[\frac{\partial H_x}{\partial z} - \frac{\partial H_z}{\partial x} - \sigma E_y \right]
$$
$$
\frac{\partial E_z}{\partial t} = \frac{1}{\epsilon} \left[\frac{\partial H_y}{\partial x} - \frac{\partial H_x}{\partial y} - \sigma E_z \right]
$$
$$
\frac{\partial H_x}{\partial t} = \frac{1}{\epsilon} \left[\frac{\partial E_y}{\partial z} - \frac{\partial E_z}{\partial y} \right]
$$
$$
\frac{\partial H_y}{\partial t} = \frac{1}{\epsilon} \left[\frac{\partial E_z}{\partial x} - \frac{\partial E_x}{\partial z} \right]
$$
$$
\frac{\partial H_x}{\partial t} = \frac{1}{\epsilon} \left[\frac{\partial E_x}{\partial y} - \frac{\partial E_y}{\partial x} \right]
$$

(A.1)

With the notation

$$
E_x|_{i,j,k} = E_x(i\Delta x, j\Delta y, k\Delta z) \tag{A.2}
$$

where the grid spatial points are denoted by $(i, j, k) = (i\Delta x, j\Delta y, k\Delta z)$ with Δx, Δy and Δz the spatial step along the three directions x, y and z, and i, j and k integer number, by space and time discretization, the first equation of (A.1) for the E_x component becomes
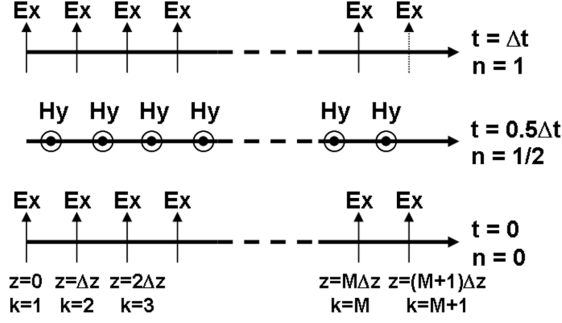
Figure A.2: The 1D space-time Yee algorithm showing central differences for the space derivatives and leapfrog over the time derivatives. k represent electric field node numbers and n is the time step.

$$
E_x|_{i,j+1/2,k+1/2}^{n+1/2} = \left(\frac{1 - \frac{\sigma \Delta t}{2\epsilon}}{1 + \frac{\sigma \Delta t}{2\epsilon}} \right) E_x|_{i,j+1/2,k+1/2}^{n-1/2} +
$$
$$
+ \left(\frac{\frac{\Delta t}{\epsilon}}{1 + \frac{\sigma \Delta t}{2\epsilon}} \right) \left[\frac{H_z|_{i,j+1,k+1/2}^{n} - H_z|_{i,j,k+1/2}^{n}}{\Delta y} - \frac{H_y|_{i,j+1/2,k+1}^{n} - H_y|_{i,j+1/2,k}^{n}}{\Delta z} \right]
$$
$$
\tag{A.3}
$$

For the other field components analogous discretized expressions hold. It is clear that a first advantage of this technique is that the new value of a electromagnetic component at any grid point depends only on its previous value and previous values of the other fields at adjacent points. Then, in very simple way, the Maxwell's equations are fully solved. Moreover, the discretized equations result explicit, thus numerical implementations do not require solving for matrix inversion. Another advantage is that the continuity of the tangential components of **E** and **H** fields is naturally ensured by the gird structure. Finally, it must be noted that due to their definition, the central finite difference expression for the derivatives have second-order accuracy.

A.1 Reduction to two dimension: TM and TE modes

If the structure extends to infinity along the z coordinate without any change in both the geometry and the electromagnetic properties, the electromagnetic wave is also uniform in z direction and all partial derivatives with respect to z are zero. In this case the Maxwell's equations become

$$
\begin{aligned}
\frac{\partial H_x}{\partial t} &= -\frac{1}{\mu}\frac{\partial E_z}{\partial y} \\
\frac{\partial H_y}{\partial t} &= \frac{1}{\mu}\frac{\partial E_z}{\partial x} \\
\frac{\partial H_z}{\partial t} &= -\frac{1}{\mu}\left[\frac{\partial E_x}{\partial y} - \frac{\partial E_y}{\partial x}\right] \\
\frac{\partial E_x}{\partial t} &= \frac{1}{\epsilon}\left[\frac{\partial H_z}{\partial y} - \sigma E_x\right] \\
\frac{\partial E_y}{\partial t} &= -\frac{1}{\epsilon}\left[\frac{\partial H_z}{\partial x} + \sigma E_y\right] \\
\frac{\partial E_z}{\partial t} &= \frac{1}{\epsilon}\left[\frac{\partial H_y}{\partial x} - \frac{\partial H_x}{\partial y} - \sigma E_z\right]
\end{aligned}
\tag{A.4}
$$

The equations that involve only H_x, H_y, and E_z are designed as transverse magnetic modes (TM):

$$
\begin{aligned}
\frac{\partial H_x}{\partial t} &= -\frac{1}{\mu}\frac{\partial E_z}{\partial y} \\
\frac{\partial H_y}{\partial t} &= \frac{1}{\mu}\frac{\partial E_z}{\partial x} \\
\frac{\partial E_z}{\partial t} &= \frac{1}{\epsilon}\left[\frac{\partial H_y}{\partial x} - \frac{\partial H_x}{\partial y} - \sigma E_z\right]
\end{aligned}
\tag{A.5}
$$

whereas the equations that involve only E_x, E_y, and H_z are designed as transverse electric modes (TE):

$$
\begin{aligned}
\frac{\partial E_x}{\partial t} &= -\frac{1}{\epsilon}\left[\frac{\partial H_z}{\partial y} - \sigma E_x\right] \\
\frac{\partial E_y}{\partial t} &= -\frac{1}{\epsilon}\left[\frac{\partial H_z}{\partial x} + \sigma E_t\right] \\
\frac{\partial H_z}{\partial t} &= \frac{1}{\mu}\left[\frac{\partial E_x}{\partial y} - \frac{\partial E_y}{\partial x}\right]
\end{aligned}
\tag{A.6}
$$

Discretization for the TM modes yields

$$E_z|_{i-1/2,j+1/2}^{n+1/2} = \left(\frac{1 - \frac{\sigma\Delta t}{2\epsilon}}{1 + \frac{\sigma\Delta t}{2\epsilon}}\right) E_z|_{i-1/2,j+1/2}^{n-1/2} +$$

$$+ \left(\frac{\frac{\Delta t}{\epsilon\Delta x}}{1 + \frac{\sigma\Delta t}{2\epsilon}}\right) \left[H_y|_{i,j+1/2}^{n} - H_y|_{i-1,j+1/2}^{n}\right] + \left(\frac{\frac{\Delta t}{\epsilon\Delta y}}{1 + \frac{\sigma\Delta t}{2\epsilon}}\right) \left[H_x|_{i-1/2,j}^{n} + H_x|_{i-1/2,j+1}^{n}\right]$$

$$H_x|_{i-1/2,j+1}^{n+1} = H_x|_{i-1/2,j+1}^{n} + \left(\frac{\Delta t}{\mu\Delta y}\right) \left[E_z|_{i-1/2,j+1/2}^{n+1/2} - E_z|_{i-1/2,j+3/2}^{n+1/2}\right]$$

$$H_y|_{i,j+1/2}^{n+1} = H_y|_{i,j+1/2}^{n} + \left(\frac{\Delta t}{\mu\Delta x}\right) \left[E_z|_{i+1/2,j+1/2}^{n+1/2} - E_z|_{i-1/2,j+1/2}^{n+1/2}\right]$$

$$(A.7)$$

and discretization for TE modes yields

$$E_x|_{i,j+1/2}^{n+1/2} = \left(\frac{1 - \frac{\sigma\Delta t}{2\epsilon}}{1 + \frac{\sigma\Delta t}{2\epsilon}}\right) E_x|_{i,j+1/2}^{n-1/2} + \left(\frac{\frac{\Delta t}{\epsilon\Delta y}}{1 + \frac{\sigma\Delta t}{2\epsilon}}\right) \left[H_z|_{i,j+1}^{n} - H_z|_{i,j}^{n}\right]$$

$$E_y|_{i-1/2,j+1}^{n+1/2} = \left(\frac{1 - \frac{\sigma\Delta t}{2\epsilon}}{1 + \frac{\sigma\Delta t}{2\epsilon}}\right) E_y|_{i-1/2,j+1}^{n-1/2} + \left(\frac{\frac{\Delta t}{\epsilon\Delta x}}{1 + \frac{\sigma\Delta t}{2\epsilon}}\right) \left[H_z|_{i-1,j+1}^{n} - H_z|_{i,j+1}^{n}\right]$$

$$H_z|_{i,j+1}^{n+1} = H_x|_{i,j+1}^{n} + \left(\frac{\Delta t}{\mu\Delta y}\right) \left[E_x|_{i,j+3/2}^{n+1/2} - E_x|_{i,j+1/2}^{n+1/2}\right]$$

$$+ \left(\frac{\Delta t}{\mu\Delta y}\right) \left[E_y|_{i-1/2,j+1}^{n+1/2} - Ey|_{i+1/2,j+1}^{n+1/2}\right]$$

$$(A.8)$$

These very simple expressions are suitable for numerical implementation of electromagnetic propagation in structures that support polarized light. In particular, since this is the situation of interest for the devices analyzed in this thesis, they are often applied to the analysis of nonlinear dynamics in photonic crystal devices.

A.2   Boundary conditions: Perfectly Matched Layer

At boundaries the set of Eqs. (A.4) must be modified by alternative equations (boundary conditions) to treat the edge of the computational domain. To
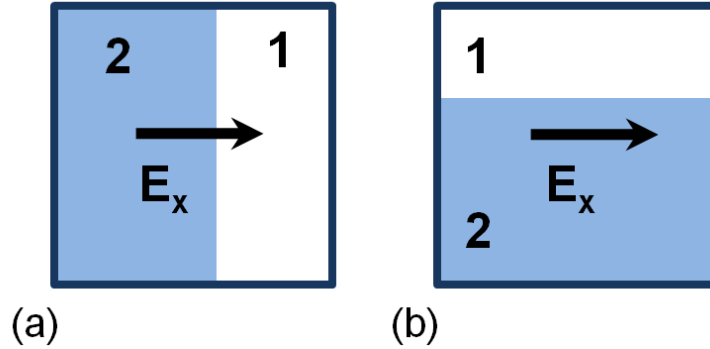
Figure A.3: Partially filled cells: (a) interface orthogonal to the electric field component. (b) interface parallel to the electric field component [29].

this end, different constrains (perfectly electric or magnetic material, or periodical conditions) can be imposed depending on the different situations. If the structure is thought as an indefinitely extended domain, then the boundary conditions should guarantee the propagation toward infinite without any spurious reflection. In this case the boundary conditions are named Absorbing Boundary Condition (ABC) [26]. When ABC satisfy the two constrains:
- are extended over a thin layer so that the number of cells involved is very low and the computational effort is not affected by their presence
- absorb outgoing waves from the interior of the domain without reflecting them back
then they are said Perfectly Matched Layer (PML) conditions [27].

A.3 Effective permittivity

Effective permittivity method accounts for the boundary condition of the electromagnetic field at dielectric interfaces. Different shaped dielectric surfaces, such as periodic array of holes in a PhC, can generate partially filled FDTD cells [28], [29]. An approach to minimize the computational errors emerging to this not fine tuned of dielectric boundary is to assign an effective permittivity for partially filled cells. The calculation of the effective permittivity requires both the tangential and the normal components of the electric field. If the electric field is parallel to the interface, the effective

permittivity can be derived from the integral form of Ampere's law, whereas if the electric field is perpendicular to the interface (see Fig. A.3), it follows from the integral form of the Faraday's law. Both parallel and perpendicular contributions to the effective permittivity can be treated with the following expression for the dielectric constant [30]:

$$\epsilon_{||} = f\epsilon_2 + (1 - f)\epsilon_1 \tag{A.9}$$

$$\epsilon_{\perp} = \left(\frac{f}{\epsilon_2} + \frac{(1 - f)}{\epsilon_1}\right)^{-1} \tag{A.10}$$

where f is the ratio of the filled area of the cell to the whole cell area and ϵ_1, ϵ_2 are the dielectric permittivity of media 1 and 2 respectively. For curved surfaces, the effective permittivity is the superposition of the normal and the parallel effective permittivity with respect to the angle between the electric field and the boundary, therefore the following phenomenological relation can be used

$$\epsilon_{eff} = \epsilon_{||}cos^2\theta + \epsilon_{\perp}(1 - cos^2\theta) \tag{A.11}$$

where θ is the angle between the electric field vector and the normal vector to the boundary.

Appendix B

Nonlinear FDTD scheme

In this appendix the discretized 2D-FDTD equations that fully account for the TE polarized light in nonlinear regime are described. The spatial grid is discretized in cells of size $\Delta x \times \Delta z$ in a two-dimensional domain (x, z) where the i, k indexes denote the coordinates of the single cell. The equations are updated at the time $(n + 1/2)\Delta t$ for the electrical field, and at the time $(n + 1)\Delta t$ for the magnetic field, being Δt the temporal step.

B.1 Main equations

The coefficients accounting for the nonlinear evolution of the electric field are set up as follows

$$
\begin{aligned}
G1_x{}^{n+1/2}(i,k) &= \frac{\epsilon_0}{\Delta t}\epsilon_{r,x}(i,k) + \chi_{Kerr}{}^{n+1/2}(i,k) + \frac{2\epsilon_0\sqrt{\epsilon_r}}{\Delta t}\Delta n_{plasma}^{n+1/2}(i,k)+ \\
&+ \frac{\epsilon_0}{4}\left[\chi_{TPA}{}^{n+1/2}(i,k) + \chi_{TPA,stored}^{n+1/2}(i,k)\right] + \frac{c_0\epsilon_0\sqrt{\epsilon_r}\sigma_{FCA}}{2}N^{n+1/2}(i,k) \\
G2_x(i,k)^{n+1/2} &= \frac{\epsilon_0}{\Delta t}\epsilon_{r,x}(i,k) + \chi_{Kerr,stored}^{n+1/2}(i,k) + \frac{2\epsilon_0\sqrt{\epsilon_r}}{\Delta t}\Delta n_{plasma,stored}^{n+1/2}(i,k)+ \\
&+ \frac{\epsilon_0}{4}\left[\chi_{TPA}{}^{n+1/2}(i,k) + \chi_{TPA,stored}^{n+1/2}(i,k)\right] + \frac{c_0\epsilon_0\sqrt{\epsilon_r}\sigma_{FCA}}{2}N^{n+1/2}(i,k) \\
G1_z(i,k)^{n+1/2} &= \frac{\epsilon_0}{\Delta t}\epsilon_{r,z}(i,k) + \chi_{Kerr}{}^{n+1/2}(i,k) + \frac{2\epsilon_0\sqrt{\epsilon_r}}{\Delta t}\Delta n_{plasma}^{n+1/2}(i,k)+ \\
&+ \frac{\epsilon_0}{4}\left[\chi_{TPA}{}^{n+1/2}(i,k) + \chi_{TPA,stored}^{n+1/2}(i,k)\right] + \frac{c_0\epsilon_0\sqrt{\epsilon_r}\sigma_{FCA}}{2}N^{n+1/2}(i,k) \\
G2_z(i,k)^{n+1/2} &= \frac{\epsilon_0}{\Delta t}\epsilon_{r,z}(i,k) + \chi_{Kerr,stored}^{n+1/2}(i,k) + \frac{2\epsilon_0\sqrt{\epsilon_r}}{\Delta t}\Delta n_{plasma,stored}^{n+1/2}(i,k)+ \\
&+ \frac{\epsilon_0}{4}\left[\chi_{TPA}{}^{n+1/2}(i,k) + \chi_{TPA}{}^{n-1/2}(i,k)\right] + \frac{c_0\epsilon_0\sqrt{\epsilon_r}\sigma_{FCA}}{2}N^{n+1/2}(i,k)
\end{aligned}
\tag{B.1}
$$

where σ_{FCA} is the cross section for free-electrons and free-holes absorption. Following the order in RHS of Eqs. (B.1), each coefficients stores the linear polarization, the Kerr effect, the plasma effect, the losses induced by TPA, and the losses due to FCA, respectively. It is worth to note that the relative dielectric permittivity is separated in two components x and z in order to take into account the effective permittivity seen by the two electric components E_x and E_z as described in last section of appendix A.

By means of these definitions, the time-step equations for the electric field are written in compact form as follows

$$
\begin{aligned}
E_x{}^{n+1/2}(i+1,k) &= \frac{G2_x(i+1,z)}{G1_x(i+1,k)}E_x{}^{n-1/2}(i+1,k) - \frac{H_y{}^n(i+1,k+1) - H_y{}^n(i+1,k)}{\Delta z G1_x(i+1,k)} \\
E_z{}^{n+1/2}(i+1,k) &= \frac{G2_z(i+1,z)}{G1_z(i+1,k)}E_x{}^{n-1/2}(i+1,k) + \frac{H_y{}^n(i+1,k+1) + H_y{}^n(i+1,k)}{\Delta z G1_z(i+1,k)}
\end{aligned}
\tag{B.2}
$$

For the Kerr susceptibilty, at the step $(n + 1/2)\Delta t$, the old $\chi_{Kerr}^{n-1/2}$ must be firstly stored and then the corresponding equation can be updated:

$$\chi_{Kerr,stored}^{n+1/2}(i,k) = \chi_{Kerr}^{n-1/2}(i,k)$$
$$\chi_{Kerr}^{n+1/2}(i,k) = c_0\epsilon_0\epsilon_r n_{2I}(i,k) \left[|E_x^{n+1/2}(i,k)|^2 + |E_z^{n+1/2}(i,k)|^2\right] \quad \text{(B.3)}$$

where n_{2I} is the nonlinear Kerr coefficient.

Equivalently, the update equations for the TPA losses are given by

$$\chi_{TPA,stored}^{n+1/2}(i,k) = \chi_{TPA}^{n-1/2}(i,k)$$
$$\chi_{TPA}^{n+1/2}(i,k) = \frac{2c_0\epsilon_0\epsilon_r\beta_{TPA}(i,k)}{2} \left[|E_x^{n+1/2}(i,k)|^2 + |E_z^{n+1/2}(i,k)|^2\right] \quad \text{(B.4)}$$

with β_{TPA} being the TPA coefficient.

The rate equation discretized for the carriers density N writes as

$$N^{n+1}(i,k) = \frac{1}{c_{o1}} \frac{c_0^2\epsilon_0^2\epsilon_r\beta_{TPA}(i,k)}{8\hbar\omega_0} \left[|E_x^{n+1/2}(i,k)|^2 + |E_z^{n+1/2}(i,k)|^2\right]^2 +$$
$$+ \frac{c_{o2}}{c_o1}N(i,k) + \frac{c_{o3}}{c_{o1}}[N^n(i+1,k) + N^n(i-1,k)] + \frac{c_{o4}}{c_{o1}}[N^n(i,k+1) + N^n(i,k-1)] \quad \text{(B.5)}$$

where the coefficients c_{op} with $p = 1, 2, 3, 4$ are defined as follows

$$c_{o1} = \frac{2\tau_r + \Delta t}{2\tau_r\Delta t} \qquad c_{o1} = \frac{2\tau_r - \Delta t}{2\tau_r\Delta t}$$
$$c_{o3} = \frac{D}{2\Delta x^2} \qquad c_{o4} = \frac{D}{2\Delta z^2} \quad \text{(B.6)}$$

with τ_r the carriers recovery time and D the diffusion coefficient. The same constraint applied for the Kerr and TPA coefficients must be followed for the plasma effect, that is firstly stored and then updated:

$$\Delta n_{plasma,stored}^{n+1/2}(i,k) = \Delta n_{plasma}^{n-1/2}(i,k)$$
$$\Delta n_{plasma}^{n+1/2}(i,k) = -\frac{e^2}{2\epsilon_0\omega_0^2 m^*\sqrt{\epsilon_r}}N(i,k) \quad \text{(B.7)}$$

where e is the electron charge and m^* the effective mass of the charges.

Finally, the time-step equation for the H_y field is given by

$$H_y^n(i+1,k+1) = H_y^{n-1}(i+1,k+1) + \frac{\Delta t}{\mu_0\Delta x}\left[E_z^{n+1/2}(i+1,k+1) - E_z^{n+1/2}(i,k+1)\right] -$$
$$- \frac{\Delta t}{\mu_0\Delta z}\left[E_x^{n+1/2}(i+1,k+1) - E_x^{n+1/2}(i+1,k)\right] \quad \text{(B.8)}$$
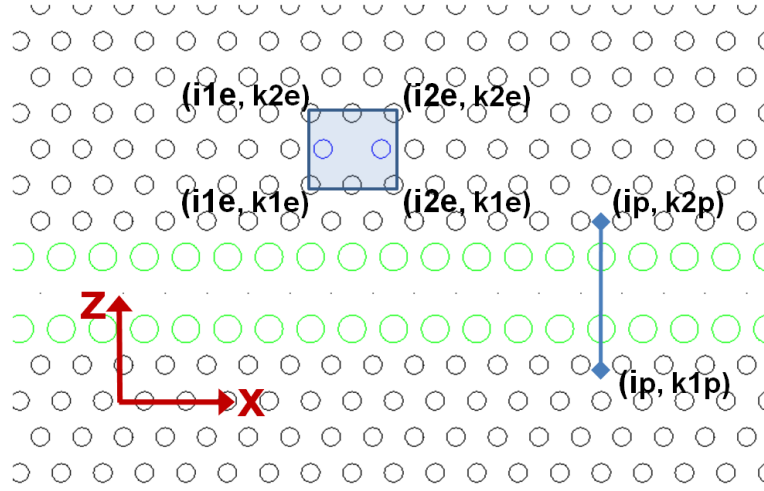
Figure B.1: Computational domain.

B.2 Computation of energies and powers

Other useful discretized equations are those set up for the time-domain calculation of the energy in a cavity and the power in a waveguide. As sketched in Fig. B.1, by identifying with the indexes $i1_e$, $i2_e$, $i1_e$ and $i2_e$ a Cartesian region including the cavity, at each time-step the energy stored inside the cavity can be evaluated by means of two nested loops that realize the discrete spatial integration:

$$
\begin{aligned}
&\mathbf{do}\ ni = i1_e, i2_e \\
&\quad \mathbf{do}\ nk = k1_e, k2_e \\
&\qquad Energy^{n+1/2} = Energy^{n+1/2} + \\
&\qquad + \frac{\epsilon_0 \epsilon_r(ni, nk)}{2} \left[|E_x^{n+1/2}(ni, nk)|^2 + |E_x^{n+1/2}(ni, nk)|^2 \right] \Delta x \Delta z \\
&\quad \mathbf{end\ do} \\
&\mathbf{end\ do}
\end{aligned}
\tag{B.9}
$$

Equivalently, the temporal evolution of the power flux that crosses a section of a waveguide (see definition of the indexes in Fig. B.1) can be numerically

integrated as follows

$$\textbf{do } nk = k1_p, k2_p$$
$$Power^n = Power^n - E_z^{n+1/2}(i_p, nk)H_y^n(i_p, nk)\Delta z \qquad \text{(B.10)}$$
$$\textbf{end do}$$

Finally, it is worth to emphasize that in simulations involving pump and probe signals, it could be useful to maintain the pump and the probe equations stored in two different lines.

List of publications

Stefania Malaguti, Gaetano Bellanca, Stefano Trillo, "Two-dimensional envelope localized waves in the anomalous dispersion regime", Optics Letter, 15 Maggio 2008, Vol. **33**, No. 10, pp. 1117-1119.

Stefania Malaguti, Stefano Trillo, "Envelope localized waves of the conilcal type in linear normally dispersive media", Physical Review A, 1 Giugno 2009, Vol. **79**, pp. 063803-1 063803-10.

A. Armaroli, S. Malaguti, S. Trillo, C. Conti, A. Fratalocchi, "Dispersive shock waves from optical dark beams", XVIII RiNEm (Riunione Nazionale di Elettromagnetismo), Benevento, Italy, Sept 6-10, 2010.

A. Armaroli, S. Malaguti, A. Fratalocchi, S. Trillo, " Control of dispersive shock dynamics developing from dark waveforms" in Nonlinear Photonics, OSA Technical Digest (CD) (Optical Society of America, 2010), paper NWB7; within Advanced Photonics and Renewable Energy OSA Optics and Photonics Congresses, Karlsruhe, Germany, June 21-24 , 2010.

S. Malaguti, A. Armaroli, G. Bellanca, S. Trillo, S. Combrié, P. Colman, A. De Rossi, " Temporal Dynamics of Nonlinear Switching in GaAs Photonic-Crystal-based Devices", CLEO/Europe-EQEC Focus Meeting 2010 "New Frontiers in Photonics", Turin, Sept. 19-23, 2010.

S. Malaguti, A. Corli, S. Trillo, "Control of gradient catastrophies developing from dark beams", Optics Letters, Vol. **35**, pp. 4217-4219 (2010).

Stefania Malaguti, Gaetano Bellanca, Sylvain Combrié, Alfredo de Rossi, Stefano Trillo, "'Self-pulsing driven by two-photon absorption in semiconductor nanocavities"', submitted to Phys. Rev. A

Acknowledgements

I would like to thank:

Stefano Trillo, Gaetano Bellanca, Alfredo De Rossi, Sylvain Combrié.

My family.

Bibliography

[1] T. Ibrahim, W. Cao, Y. Kim, J. Li, J. Goldhar, P. -T. Ho, and C. Lee, "'Lightwave Switching in Semiconductor Microring Devices by Free Carrier Injection "', J. Lightwave Tech., **21**, 2997 (2003).

[2] V. Almeida, C. Barrios, R. Panepucci, and M. Lipson, "'All-optical control of light on a silicon chip"', Nature (London) **431**, 1081 (2004).

[3] T. J. Johnson, M. Borselli, and O. Painter, "'Self-induced optical modulation of the transmission through a high-Q silicon microdisk resonator"', Optics Express **14**, 817 (2006)

[4] S. G. Johnson, P. R. Villeneuve, S. Fan, and J. D. Joannopoulos, "'Linear waveguides in photonic-crystal slabs"', Phys. Rev. B **62**, 8212 (2000).

[5] T. Tanabe, M. Notomi, S. Mitsugi, A. Shinya, and E. Kuramochi, "'Fast bistable all-optical switch and memory on a silicon photonic crystal onchip"', Opt. Lett. **30**, 2575 (2005).

[6] T. Asano, B. S. Song, Y. Akahane, and S. Noda, IEEE J, Select. Top. Quantum Electron. **12**, 1123 (2006).

[7] A. Shinya et al., Optic Express **16**, 19382 (2008).

[8] A. De Rossi, M. Lauritano, S. Combrié, Q. V. Tran, and C. Husko, "'Interplay of plasma-induced and fast thermal nonlinearities in a GaAs-based photonic crystal nanocavity"', Phys. Rev. A **79**, 043818, (2009).

[9] C. Husko, A. De Rossi, S. Combrié, Q. V. Tran, F. Raineri, and C. W. Wong, "'Ultrafast all-optical modulation in GaAs photonic crystal cavities, Apl. Phys. Lett. **94**, 021111 (2009).

[10] S. Combrié, Q. V. Tran, C. Husko, P. Colman, and A. De Rossi, "'High quality GaInP nonlinear photonic crystals with minimized nonlinear absorption"', Appl. Phys. Lett. **95**, 221108 (2009).

[11] S. Malaguti, A. Armaroli, G. Bellanca, S. Trillo, S. Combrié, P. Colman, A. De Rossi, "' Temporal Dynamics of Nonlinear Switching in GaAs Photonic-Crystal-based Devices"', CLEO/Europe-EQEC Focus Meeting 2010 "'New Frontiers in Photonics"', Turin, Sept. 19-23, 2010.

[12] N. Suzuki, "'FDTD Analysis of Two-Photon Absorption and Free-Carrier Absorption in Si High-Index-Contrast Waveguides"', J. Lightwave Tech. **25**, 2495 (2007).

[13] T. Tanabe, H. Taniyama, and M. Notomi, "'Carrier Diffusion and Recombination in Photonic Crystal Nanocavity Optical Switches"', J. Lightwave Tech. **26**, 1396 (2008).

[14] Boyd, R W. *Nonlinear Optics*, Academic Press: Boston, 1992.

[15] E. Yablonovitch, Phys. Rev. Lett. **58** (1987) 2059.

[16] S. John, Phys. Rev. Lett. **58** (1987) 2486.

[17] J. D. Joannopoulos, R. D. Meade, and J. N. Winn, *Photonic Crystals: Molding the Flow of Light*, Princeton University Press, Princeton, 1995.

[18] Sakoda, K. *Optical Properties of Photonic Crystals*, (Springer, Berlin, 2001).

[19] G. Priem, "'Nonlinear behavior in nanophotonic waveguides and resonators for ultrafast signal processing"', PhD dissertation, University Gent, 2005-2006.

[20] C. Kittel, *Introduction to solid state physics*, 7th edition New York, Wiley, 1996.

[21] J. I. Pankove, *Optical proceses in semiconductors*, New York, Dover, 1971.

[22] P. Butcher and D. Cotter, *The elements of nonlinear optics*. Cambridge: University Press, 1th ed., 1990.

[23] L. C. Andreani, and D. Gerace, ”'Photonic-crystal slabs with a triangular lattice of triangular holes investigated using a guided-mode expansion method”', Phys. Rev. B **73**, 235114 (2006).

[24] H. A. Haus, *Waves and Fields in Optoelectronics*, (Prentice-Hall, Englewood Cliffs, NJ, 1984).

[25] C. Manolatou, M. J. Khan, Shanhui Fan, Pierre R. Villeneuve, H. A. Haus, ”"' Coupling of Modes Analysis of Resonant Channel Add-Drop Filters”', IEEE J. Quantum Electron. **35**, 1322 (1999).

[26] Taflove, A. *Computational Electrodynamics: The Finite-difference Time-domain Method* (Artech House, Boston, 1995).

[27] J. Berenger, ”'A perfectly matched layer for the absorption of electromagnetic waves”', J. Comput. Phys. **114**, 185 (1994).

[28] A. Mohammadi, and M. Agio, ”'Contour-path effective permittivities for the two-dimensional finite-difference time-domain method”', Opt. Express **13**, 10367 (2005).

[29] T. Jalali1, K. Rauscher, A. Mohammadi, D. Erni, Ch. Hafner, W. Baechtold, and M. Z. Shoushtari, ”'Efficient Effective Permittivity Treatment for the 2D-FDTD Simulation of Photonic Crystals”', J. Comput. Theor. Nanosci. **4**, 644 (2007).

[30] K.Rauscher, D.Erni, J.Smajic, and C.Hafner , Prog. Elec. Research Sym. PIERS 2004 43, 25 (2004).

[31] R. Stoffer, and Yu. S. Kivshar, ”'Optical bistability in a nonlinear photonic crystal waveguide notch filter”', Proceedings Symposium IEEE/LEOS Benelux, Chapter, 2000, Delft, The Netherlands.

[32] Y. Akahane, T. Asano, and S. Noda, ”'High-Q photonic nanocavity in a two-dimensional photonic crystal”', Nature **425**, 944 (2003).

[33] E. Kuramochi, M. Notomi, S. Mitsugi, A. Shinya, T. Tanabe, and T. Watanabe, "'Ultrahigh-Q photonic crystal nanocavities realized by the local width modulation of a line defect"', Appl. Phys. Lett. **88**, 041112 (2006).

[34] A. Shinya, S. Mitsugi, E. Kuramochi, and M. Notomi, "'Ultrasmall multi-channel resonant-tunneling filter using mode gap of width-tuned photoniccrystal waveguide"', Opt. Express **13**, 4201 (2005).

[35] T. Uesugi, B.-S. Song, T. Asano, and S. Noda, "'Investigation of optical nonlinearities in an ultra-high-Q Si nanocavity in a two-dimensional photonic crystal slab"', Opt. Express **14**, 377 (2006).

[36] O. Boyraz, P. Koonath, V. Raghunathan, and B. Jalali, "'All optical switching and continuum generation in silicon waveguides"', Opt. Express, **12**, 4094 (2004).

[37] K. Ikeda, Opt. Commun. **30**, 257 (1980); K. Ikeda, and O. Akimoto, Phys. Rev. Lett. **48**, 617 (1982).

[38] A. B. Sproul, "'Dimensionless solution of the equation describing the effect of surface recombination on carrier decay in semiconductors"', J. Appl. Phys. **76**, 2851 (1994).

[39] D. Dimitropoulos, R. Jhaveri, R. Claps, J. C. S.Woo, and B. Jalali, "'Lifetime of photogenerated carriers in silicon-on-insulator rib waveguides"', Appl. Phys. Lett. **86**, 071115(1) (2005).

[40] K. Nozaki, H. Watanabe, and T. Baba, "'Photonic crystal nanolaser monolithically integrated with passive waveguide for effective light extraction"', Appl. Phys. Lett. **92**, 021108 (2008).